Universidad Autónoma de Madrid
Facultad de Ciencias
Departamento de Física Aplicada

Stress and nanostructure control for the development of magneto-electro-mechanical micro-devices.

Memoria de tesis para optar al grado de doctor en Física
presentada por:

Iván Fernández Martínez

y dirigida por:

el Prof. Fernando Briones y el Dr. Jose L. Costa-Krämer

Instituto de Microelectrónica de Madrid
Centro Nacional de Microelectrónica
Consejo Superior de Investigaciones Científicas

Tres Cantos, Noviembre 2008

Fernando Briones Fernández-Pola, Profesor de Investigación del Instituto de Microelectrónica de Madrid, y Jose Luis Costa-Krämer, Científico Titular del Instituto de Microelectrónica de Madrid, AUTORIZAN la presentación a trámite de la Tesis Doctoral de Iván Fernández Martínez, titulada “Stress ad nanostructure control for the development of magneto-electro-mechanical micro-devices”.

Tres Cantos, 11 de Octubre de 2008

Fdo.: Fernando Briones Fernandez-Pola

Fdo.: Jose Luis Costa-Krämer

La presente Tesis Doctoral ha sido llevaba a cabo gracias a la financiación por parte del Ministerio de Ciencia y Tecnología a través de una beca predoctoral perteneciente al programa de Formación de Personal Investigador.

La presente Tesis Doctoral ha sido realizada en :

Instituto de Microelectrónica de Madrid
(IMM-CNM-CSIC)

C/ Isaac Newton 8, PTM
28760 Tres Cantos (Madrid)

To my Family.
To Rachel.

Objetivos y motivación

La miniaturización de sistemas Micro-Electro-Mecánicos o MEMS ya es una realidad de nuestros días. Estos micro-dispositivos, que combinan la tecnología basada en sistemas micro-mecánicos, como por ejemplo micro-palancas, membranas, micro-actuadores, etc... y dispositivos microelectrónicos para su control, ya se emplean, por ejemplo para la realización de acelerómetros, presentes en los airbags de los automóviles. Este mismo tipo de MEMS también se emplean como elementos de navegación, particularmente en la industria aeroespacial, se utilizan como sensores de presión, temperatura, humedad, etc... o como actuadores, como pueden ser micro-espejos, micro-válvulas, etc....[1]. Por otra parte, el uso de MEMS magnéticos tiene varias ventajas [2] con respecto a las demás tecnologías. Quizás su mayor atractivo sea la interacción a distancia. Este tipo de sistemas funciona en la mayoría de los casos en forma remota, es decir, sin necesidad de contacto con lo que se pretende medir. Además, también presenta unos bajos costes de producción y bajo consumo combinado con una enorme eficiencia.

En esta tesis, es investiga la utilización de películas delgadas amorfas de Fe-B para su uso en actuadores micro-mecánicos magnetostrictivos, como por ejemplo micro-palancas del Microscopio de Fuerza Atómicas (AFM). La magnetostricción es la propiedad de los materiales magnéticos que hace que cambien sus dimensiones al encontrarse en presencia de un campo magnético. Para la integración de este tipo de películas delgadas como actuadores magnetostrictivos, se necesitan controlar :

- las tensiones residuales de las películas delgadas magnetostrictivas, ya que provocan curvaturas indeseadas en las micro-palancas.

- la anisotropía magnética, ya que no todas las direcciones son equivalentes dentro de un material magnético, lo que provoca que no todos los procesos de inversión de la imanación dan lugar a un esfuerzo magnetostrictivo.

- el carácter magnéticamente blando, de modo que pequeños campos aplicados dan lugar a una deformación del magnetostrictivo.

- la resistencia a la corrosión del material magnetostrictivo en medios corrosivos.

De este modo, la tesis se divide en seis capítulos.

En el primer capítulo (Chapter I), se describen varios conceptos básicos sobre depósito de películas delgadas, caracterización magnética y estructural, y medida de las tensiones

residuales de películas delgadas. A continuación, se presentan las técnicas experimentales usadas durante el desarrollo de esta tesis, poniendo especial énfasis en los sistemas experimentales diseñados y construidos por el autor. En particular, se describe el diseño y fabricación de un sistema de 'pulverización catódica' para el depósito de películas delgadas amorfas de $Fe_{80}B_{20}$.

El segundo capítulo (Chapter II) se centra en la medida de las tensiones acumuladas *in-situ* durante el depósito de películas delgadas amorfas de $Fe_{80}B_{20}$. A partir de estas medidas se distingue el tipo de crecimiento que desarrolla la película delgada. A continuación, se estudia el valor de al tensión total acumulada de la película delgada en función de los parámetros de depósito. El objetivo de este estudio es la obtención de películas delgadas con tensión acumulada nula.

En el tercer capítulo (Chapter III), se estudia la anisotropía magnética de las películas delgadas de $Fe_{80}B_{20}$ en función de los parámetros de depósito y geometría del sustrato. El objetivo de este estudio es controlar la dirección final de anisotropía de la película delgada, algo que es esencial para el uso de las mismas en MEMS, ya que el esfuerzo magnetostrictivo es máximo cuando el proceso de inversión de la imanación es mediante rotación coherente de dominios.

En el cuarto capítulo (Chapter IV) se estudian las propiedades magnéticas, estructurales y de resistencia a la corrosión de películas delgadas de $Fe_{80}B_{20}$ depositadas en presencia de nitrógeno.

Una vez obtenidas películas delgadas de Fe-B-N con buenas propiedades magnéticas, magnetoelásticas y de alta estabilidad química o resistencia a la corrosión, nos proponemos a usarlas como actuadores magnetostrictivas (Chapter V). Se desarrolla un nuevo Microscopio de Fuerzas Atómicas (AFM) magnetostrictivo para medidas de topografía en medios líquidos.

Finalmente, en el sexto capítulo (Chapter VI), se explican los procesos de fabricación de Sistemas Nano-Electro-Mecánicos (NEMS).

[1] K. L. Ekinci ad M. L. Roukes, '*Nano-electro-mechanical systems'*, Review of Scientific Instruments, **76**, 061101 (2005).

[2] M. R. J. Gibbs, *'Apliccations of magMEMS'*, J. Mag. Magn. Mat., **290**, 1298 (2005).

Index of contents

Chapter I

I.1. Introduction 3

I.2. Thin film deposition 3

I.2.1. Sputtering deposition 3

I.2.2. Brief discussion of the thin film deposition process 4

I.2.3. Amorphous and polycrystalline thin films: Volmer-Weber. 6

I.2.4. Experimental system at the IMM : Multi-target triode sputtering. 8

I.3. Accumulated stress in deposited thin films. 11

I.3.1. *In-situ* stress measurement of thin films. 11

I.3.2. Relation between film accumulated stress (compressive or tensile) and the sign of the curvature change. 13

I.3.3. Sources of stress in deposited thin films. 14

I.3.4. Stress in sputtered films: 'atomic peening' effect. 15

I.3.5. Experimental set-up at the IMM for in-situ stress measurement. 17

I.4. Magnetic characterization techniques 20

I.4.1. Principles of Magneto-Optical Kerr Effect (MOKE) 20

I.4.2. Experimental set-up at the IMM : Transversal Kerr and magneto-optical torque. 21

I.4.3. Magneto-elastic effects: Magnetostriction. 24

I.4.4. Experimental set-up at the IMM : Magnetostriction measurement 28

I.5. Molecular Beam Epitaxy (MBE) 32

I.6. Patterning techniques 33

References 35

Chapter II

II.1. Introduction. 41

II.2. Experimental details. 41
II.3. *In-situ* stress measurements during $Fe_{80}B_{20}$ thin film deposition. 41
II.3.1 Regime I : initial instantaneous compression 42
II.3.2. Regime II : interaction between amorphous islands and substrate 44
II.3.3. Regime III : 'Atomic peening effect' due to ion/atom bombardment 45
II.4. Total accumulated stress as a function of the deposition parameters 46
II.5. Monte-Carlo simulation: kinetic energy of arriving atoms. 47
II.6. X-ray diffraction measurements of the $Fe_{80}B_{20}$ thin films 50
II.7. Atomic Force Microscopy (AFM) measurements of the $Fe_{80}B_{20}$ thin films 51
II.7. Conclusions 52
References. 52

Chapter III

III.1. Introduction……..57
III.2. Magnetic anisotropy of deposited films…… 57
III.2.1. Growth induced: angle deposition 58
III.2.2. Stress induced 60
III.2.3. Field induced 61
III.3. Magnetic anisotropy of sputtered amorphous $Fe_{80}B_{20}$ thin films ……62
III.3.1. Balance of two contributions: stress induced and field induced anisotropy. 63
III.3.2. Balance of three contributions: stress , field and oblique incidence anisotropies. . 68
III.3.2.a) Thick glass substrate. 70
III.3.2.b) Thin glass substrate (B) which long edge is parallel to the applied magnetic field.... 74
III.3.2.c) Thin glass substrate (C) which long edge is perpendicular to the applied magnetic field 77
III.3.3. Magnetic anisotropy as a function of the target potential. 80
III.4. Conclusions……..82
References……82

Chapter IV

IV.1. Introduction. 87
IV.2. Experimental details. 88
IV.3. Structural properties of Fe-B-N films. 88
IV.3.1. Nitrogen concentration determination. 88
IV.3.2. Crystallinity. 91
IV.3.3. Chemical environment of Fe, N y B atoms. 91
IV.4. Magnetic properties of Fe-B-N thin films. 94
IV.4.1. Saturation magnetization (M_S) 94
IV.4.2. Anisotropy Constant (K_u) 95
IV.4.3. Saturation Magnetostriction coefficient (λ_S) 96
IV.5. Evaluation of the corrosion resistance in liquid environment. 98
IV.6. Conclusions. 99
References. 99

Chapter V

V.1. Introduction. 105
V.2. Introduction to Atomic Force Microscopy (AFM). 105
V.3. Fe-B-N thin films for Magnetostrictive Cantilevers. 110
V.3.1. Residual Stress measurement in commercial cantilevers. 110
V.4. Magnetostrictive drive of AFM cantilevers. 111
V.5. Conclusions 114
References. 114

Chapter VI

VI.1. Introduction. 119
VI.2. Nano-Electro-Mechanical-Systems (NEMS) 119

VI.3. NEMS fabrication process. 120

VI.4. NEMS fabrication using epitaxial GaAs/AlGaAs heterostructures. 123

VI.5. Strained NEMS for the fabrication of a tunnelling displacement detector. 124

VI.6. Conclusions. 131

Referencias. 131

I

Thin film deposition, accumulated stress, and magnetic measurements : experimental techniques used in this thesis.

I.1. Introduction. 3

I.2. Thin film deposition. 3

I.2.1. Sputtering deposition. 3

I.2.2. Brief discussion of the thin film deposition process. 4

I.2.3. Amorphous and polycrystalline thin films: Volmer-Weber. 6

I.2.4. Experimental system at the IMM : Multi-target triode sputtering. 8

I.3. Accumulated stress in deposited thin films. 11

I.3.1. *In-situ* stress measurement of thin films. 11

I.3.2. Relation between film accumulated stress (compressive or tensile) and the sign of the curvature change. 13

I.3.3. Sources of stress in deposited thin films. 14

I.3.4. Stress in sputtered films: ‘atomic peening’ effect. 15

I.3.5. Experimental set-up at the IMM for *in-situ* stress measurement. 17

I.4. Magnetic characterization techniques. 20

I.4.1. Principles of Magneto-Optical Kerr Effect (MOKE). 20

I.4.2. Experimental set-up at the IMM : Transversal Kerr and magneto-optical torque. 21

I.4.3. Magneto-elastic effects: Magnetostriction. 24

I.4.4. Experimental set-up at the IMM : Magnetostriction measurement. 28

I.5. Molecular Beam Epitaxy (MBE). 32

I.6. Patterning techniques. 33

References. 35

I.1. Introduction.

This chapter describes the process of thin film deposition and the experimental arrangement used to obtain the magnetostrictive films and semiconductor epitaxial heterostructures studied in this work. It also describes the physics fundamentals and the methods used to study the structural, magnetic and magneto-elastic properties of the thin films.

I.2. Thin film deposition.

I.2.1. Sputtering deposition.

The process of sputter deposition is one of the most commonly used methods for the deposition of thin films [1]. Its popularity stems from the simplicity of the physical process involved, the accurate control of deposition rate, excellent film adhesion and high degree of reproducibility of the deposited films. It also allows deposition of high melting point metals, insulators, and different compounds through co-deposition or reactive sputtering with nitrogen, oxygen, etc.. Sputtering is a physical process by which highly energetic gas ions strike the surface of a solid target, causing the emission of neutral atoms by momentum transfer. These sputtered atoms ejected from the target travel through the vacuum chamber and are deposited onto a substrate, reaching energies in the 10 - 100 eV regime. Since the sputtering process is carried out in a gas atmosphere, with a typical sputtering gas pressure of 10^{-3} mbar, the energy of the arriving atoms can be varied not only by changing the target accelerating potential, but the sputtering pressure as well. The process is schematically shown in Figure 1, where a number of atoms are ejected when the Ar^{+} ions collide with the target material. Some of the bombarding atoms are also reflected back and neutralised, but may still be energetic enough to reach the substrate where the film is being deposited. This is a source of substrate bombardment (back-scattering) that affects the resulting film properties. The energy of the atoms arriving to the substrate is varied by changing the sputtering pressure or the target potential.

A triode sputtering [2] has been used in this thesis for the deposition of amorphous magnetostrictive films. In this sputtering configuration, the ionization of the plasma is achieved by injecting electrons into the plasma from a hot filament, which are accelerated by an anode at a positive potential, as shown in Figure 1. The main advantage of this sputtering configuration is that independent control of the ion energy is achieved either changing the target potential or working gas pressure. In other sputtering configuration, as for example a magnetron sputtering, the secondary electron emission from the target is the only source of electron injection, being dependent the value of the target potential with the sputtering working pressure. Moreover, deposition at very low pressures ~ 10^{-4} - 10^{-3} mbar can be achieved. This allows a high kinetic energy of the impinging atoms, as the number of collisions between the depositing atoms while they travel from the target to substrate and gas atoms is reduced. A magnetic field provided by

a Helmholtz coil can be used to confine the plasma and increase the plasma density. Typical growth conditions are as follows: anode potential +30 V, anode current 2 Amps, filament current 13 Amps and a plasma-confining magnetic field of about 10 Oe.

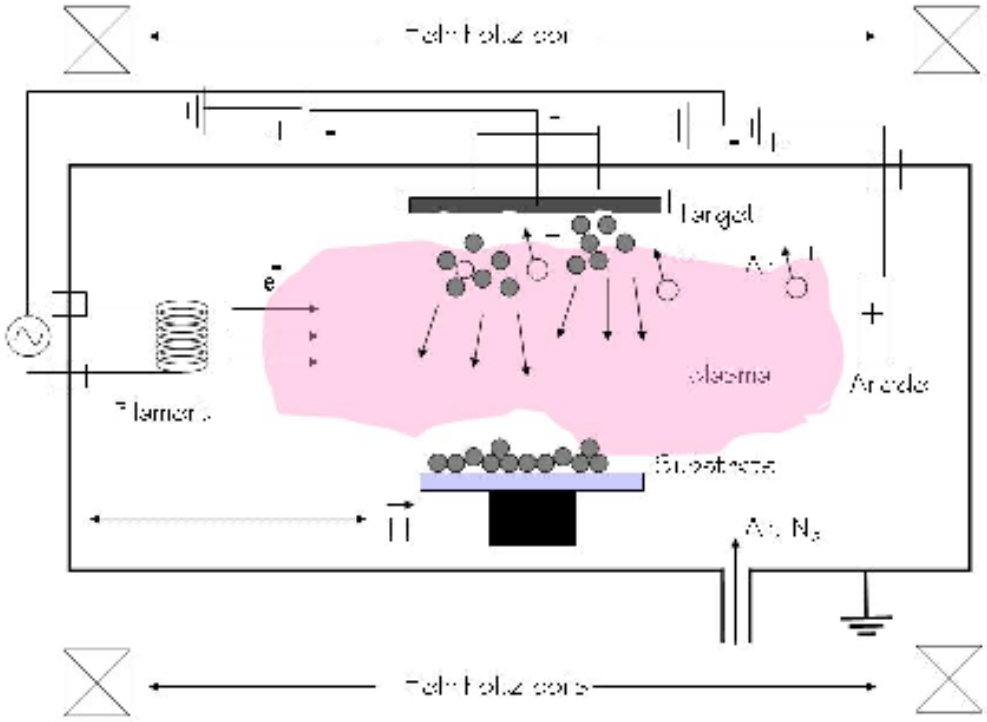

Figure 1 : Schematic view of the triode sputtering mechanism.

In summary, sputter deposition is a complex process where there are combinations of sputtering parameters which influence structural, and consequently the magnetic, mechanical, electrical, etc… properties of the depositing film. It is experimentally found that one set of sputtering parameters on a given sputtering system cannot be transferred to another system to deposit films with the same magnetic and structural properties. This illustrates how sensitive the films are to the sputtering parameters.

I.2.2. Brief discussion of the thin film deposition process.

The basic processes occurring at the surface of the substrate during film deposition are shown in Figure 2. The arriving atoms reach the substrate, transfer its kinetic energy and become a loosely bonded type of particles known as adatoms. In the case of thermal evaporation, the kinetic energy of the arriving atoms oscillate between 0.1 to 1.0 eV, while for sputtered atoms, the value of the kinetic energy can reach hundreds of eV. These adatoms diffuse over the substrate surface until they are either adsorbed at low energy sites or desorbed by evaporation or re-sputtering. The adatom diffusivity depends mainly on the interaction between the same adatoms and the substrate atoms and on the substrate temperature. The low energy sites or nucleation sites can be defects on the substrate, steps, etc… From this

nucleation site, thin film growth develops. This growth can generally be classified into three major modes:

- Volmer-Weber growth mode [3] or three dimensional (3D) island growth : the first few atomic layers grow as adatom clusters or islands of the depositing material centred on nucleation sites. These islands increase their size until they touch each other, reaching the coalescence thickness. Typically, the value of this thickness varies between 2 nm, for example for a Ni film deposited at 15 K, or 15 nm, for a Au film deposited at 600 K. The thin film properties at the thickness around or below the percolation threshold will be very different from the bulk properties. For this growth mechanism, film and substrate are usually either different materials or the crystalline structure is different. Moreover, the interaction is stronger between depositing atoms than between the depositing atoms and substrate. The film growth develops either by adsorption of bigger islands by the smaller ones, or by coalescence between islands. Once the islands coalesce, the arriving atoms incorporate to the microstructure through surface diffusion or adsorption processes, as occurs at the initial stages. Some new process, as for example diffusion through the grain boundaries or voids can also occur. This growth mode is typical from polycrystalline or amorphous films.

- Frank-van de Merwe growth mode [4] or two dimensional (2D) growth : film grows layer-by-layer perfectly coupled to the substrate. Adatoms attach preferentially to surface sites resulting in atomically smooth, fully formed layers. This layer-by-layer growth is two dimensional, indicating that complete layers form prior to growth of subsequent layers.

- Stranski - Krastanov growth mode [5] or layer-plus-island growth: first few layers grow layer-by-layer coupled to the substrate, but beyond a critical thickness of the deposited film that depends for example on the lattice mismatch, growth continues through the nucleation and coalescence of islands.

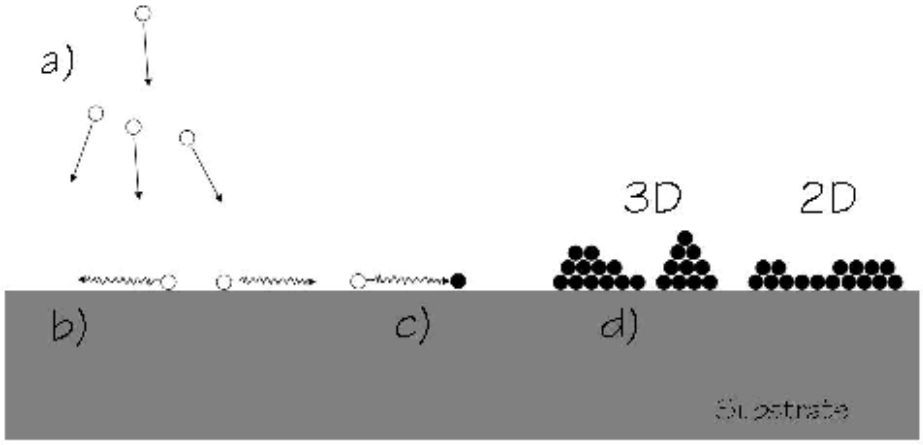

Figure 2 : Schematic view of the thin film growth mechanism by means of a physical vapour deposition (PVD) process. This process includes: a) arriving of the depositing atoms, b) adsorption and diffusion of the atoms onto the substrate surface, c) nucleation and d) growth modes.

The adatom diffusion at the substrate surface is highly dependent upon the deposition parameters, as for example the temperature of the substrate and the surface of the substrate itself [6]. In the case of sputter deposition, the adatom diffusion depends also on the target potential, sputtering pressure and distance between target and substrate. Moreover, other species of particles as neutral reflected atoms can also arrive at the substrate with enough energy to sputter the film or become incorporated into the film itself. The bombardment of this particles can be controlled either by working at pressures where the mean free path of the particles is small compared to the target to substrate separation, or by working at lower target potentials. All particles impinging on the substrate, including electrons, transfer energy in the form of heat, increasing the temperature of the substrate surface, which affects the mobility of the depositing atoms and consequently the film microstructure.

I.2.3. Amorphous and polycrystalline thin films: Volmer-Weber.

In the Volmer – Weber growth mode, it has been demonstrated that the activation energies of processes such as adatom diffusion or diffusion through voids has a exponential dependence with the melting temperature $T_{melting}$ of the depositing material. The morphology and microstructure of deposited thin films, and consequently its properties, was found to be dependent on the relation $T/T_{melting}$ during the deposition process, where T is the temperature at which the deposition is carried out. A model for the thin film microstructure was developed by B. A. Movchan y A. V. Demchishim [7]. This model, named MD model, is valid for thin films evaporated at different values of $T/T_{melting}$. Later, J. A. Thornton [8] has extended to sputtered thin films by adding a third coordinate to account the influence of working gas pressure. This model was named TMD model, and shows four different zones:

- Zone I ($0 < T/T_{melting} < 0.1$): in this regime, adatom diffusion is insufficient to overcome the effects of shadowing. There is a high density of nucleation sites and columnar grain growth in the flux direction. The microstructure is dominated by open boundaries. Recrystallization processes are inhibited. This phenomena is enhanced with increasing the sputtering gas pressure, as the number of collisions between the arriving atoms and the gas atoms increases, reducing the energy of the deposited atoms. This microstructure is typical of amorphous thin films or materials with high melting point, as for example Mo, W, Cr…. In the amorphous case, the surface diffusion is limited as a consequence of the substrate temperature or the presence of several elements, as for example the amorphous Fe-B alloy.

- Zone T or “transition” zone ($0.1 < T/T_{melting} < 0.3$): in this regime, if the deposited atoms arrive at normal incidence and no effect of the substrate roughness exists, the deposited atoms have enough surface diffusion to overcome the roughness introduced by the initial nucleated islands. As in the first regime, there is a high density of nucleation sites, while the adatom migration between neighbouring islands is allowed at coalescence. Islands that grow with lower surface energy incorporate a higher number of atoms. There is a competitive crystal growth,

that reflects in a V-shape of the islands as the thickness increases. Films deposited under these conditions show improved mechanical and electrical properties.

- Zone II ($0.3 < T/T_{melting} < 0.5$): in this regime, film growth is dominated by migration between grain boundaries. This gives rise to a crystalline growth from the initial islands formed at the surface. Grain size increases due to coalescence between grains. The microstructure is still columnar, denser and formed by microcrystalline grains with a diameter that increases with the relation $T/T_{melting}$. Crystal size can reach the film thickness. Films deposited under these conditions show good mechanical and electrical properties.

- Zona III ($0.5 < T/T_{melting} < 1.0$): in this regime, adatom diffusion is sufficient to largely overcome shadowing, while the microstructure appears to be determined by surface recrystallization and preferential growth of oriented crystal faces. Impurities are also segregated to the surface.

A schematic view of the film microstructure according to the MD and TMD models is shown in Figure 3. In the second model, proposed by Thornton, an increase in the working pressure, that reduces the energy of the arriving atoms and randomize its direction, displaces the film microstructure to higher values of $T/T_{melting}$.

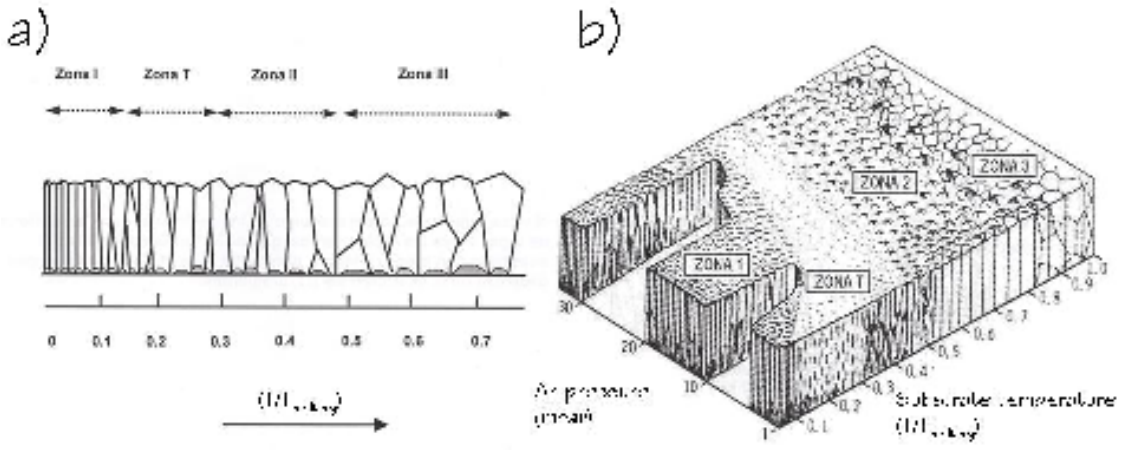

Figure 3 : a) Evolution of the microstructure for films evaporated at different substrates temperatures (T) relative to the melting point ($T_{melting}$) of the deposited material. This model, named MD, was developed by B. A. Movchan and A. V. Demchishin. b) Evolution of the microstructure for films sputtered at different substrates temperatures (T) relative to the melting point ($T_{melting}$) of the deposited material and argon gas pressures. This model, named TMD, was developed by Thornton.

I.2.4. Experimental system at the IMM : Multi-target triode sputtering.

In this thesis, all magnetic films were deposited using a triode sputtering system. A picture of the system is shown in Figure 4. It consist in a cylindrical chamber made of stainless-steel 304 grade, that is evacuated by a turbo-pump accompanied by a mechanical rotary pump, reaching a base pressure in the 10^{-9} mbar regime. The chamber pressure was monitored by a Pirani gauge, in the range 10^{3} – 10^{-2} mbar, and a Penning gauge in the range 10^{-2} – 10^{-10} mbar. The sputtering chamber is connected to a load lock chamber through a gate valve. Pumping in the load-lock chamber consist in a turbo-pump accompanied by a mechanical rotary pump, reaching a base pressure of $5 \cdot 10^{-7}$ mbar in approximately 10 minutes. The substrate holder is transferred from the load-lock to the sputtering chamber by a linear magnetic manipulator that also allows to rotate the substrate holder. A halogen lamp type of heater is introduced in the load-lock chamber to degas the substrates at 200 ºC. There are two gas inlet ports in the sputtering chamber to admit argon and nitrogen into the vacuum chamber. The gas flow was controlled by a needle valve. High purity sputtering gases were used (99.995%).The sputtering chamber is connected to a mass spectrometer that allows leakage and base pressure chemical composition detections. A quartz crystal microbalance is used for the deposition rate control. A Helmholtz coil is placed around the outside of the chamber to apply an axial magnetic field parallel to the substrate surface.

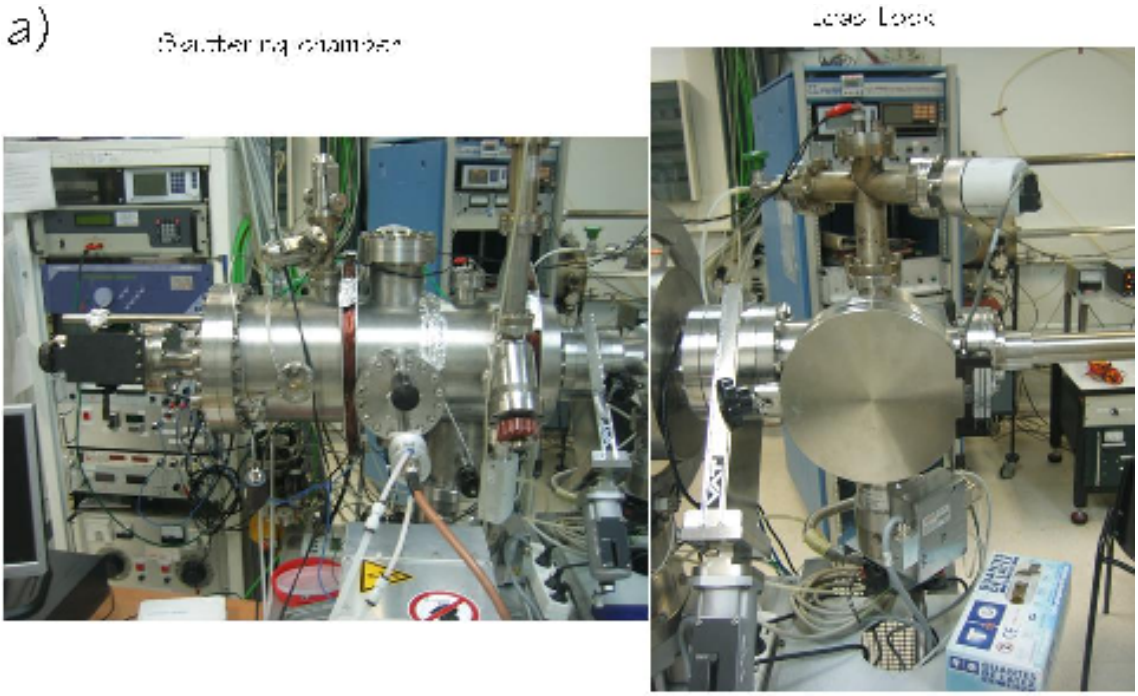

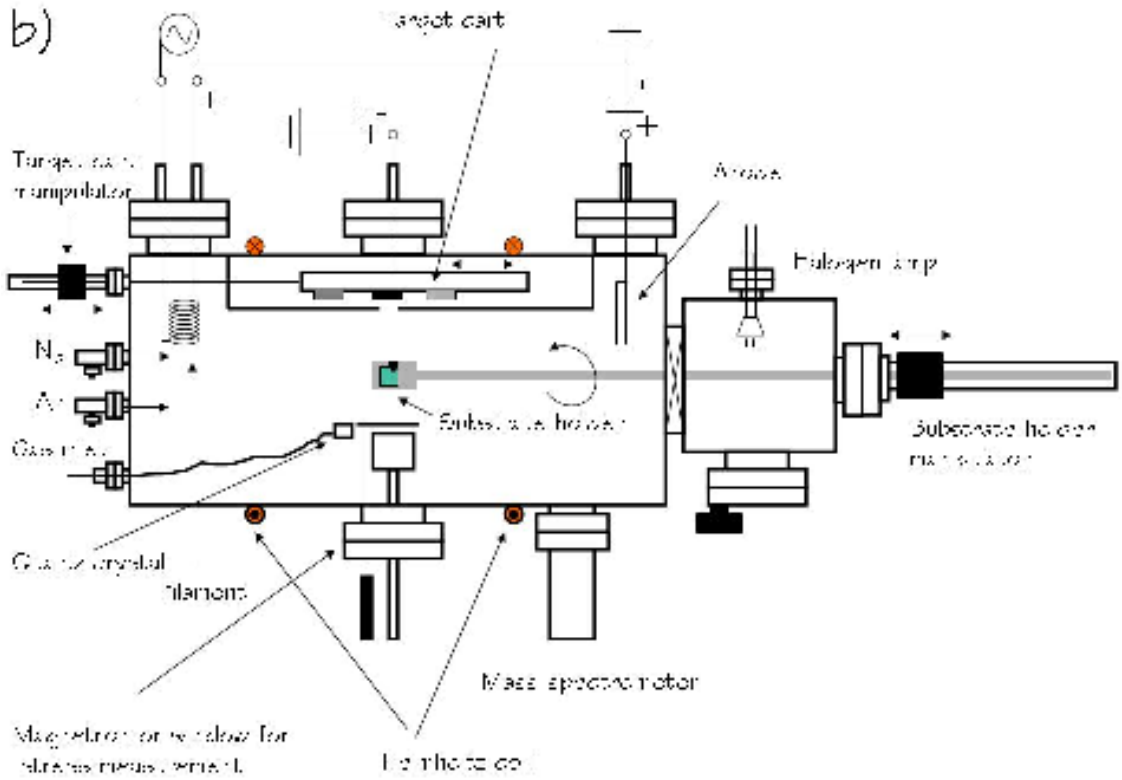

Figure 4 : a) IMM sputtering chamber and load-lock chamber. b) Schematic picture (top view) of the IMM sputtering system. c) Picture of the inside of the sputtering chamber.

As shown in Figure 4, the system includes a thermo-emissive cathode, an anode placed opposite to the filament and a target holder. A positive potential is applied to the anode to accelerate the electrons emitted by the cathode. These accelerated electrons strike and ionize the gas atoms, thus producing the plasma. The thermo-emissive cathode consist in a heating filament coil made of 0.2 mm diameter tungsten wire in a spiral shape of 2 mm diameter and 20 mm long. The anode is made of square tantalum foil, 0.2 mm thick and 4 × 8 cm^2 area. The targets (50 mm diameter) are positioned perpendicular to the anode–cathode axis. An homogeneous magnetic field provided by an external Helmholtz coil is applied co-axially to the electrical field in the anode – filament direction. This field confines the emitted electrons from the hot filament and increases the plasma density.

Three different parameters are necessary to control the plasma conditions : (a) the gas pressure ($5 \cdot 10^{-4}$ to $25 \cdot 10^{-2}$ mbar range), (b) heating filament current (typically 13 Amps), and (c) plasma current (typically 2 Amps). The potential applied to the sputtering target, which is independent on the plasma conditions, can be varied between -0.5 kV and -2.0 kV. The deposition rate depends on the target potential, gas pressure, applied magnetic field and the chemical nature of the target material. In the case of $Fe_{80}B_{20}$ films, the deposition rate was 1.2 Å/s with a target potential of -2.0 kV, working gas pressure of $8 \cdot 10^{-3}$ mbar and an applied magnetic field produced by 6 Amps through the coil windings.

A novel target holder system was designed, fabricated and used in this thesis. As shown in Figure 5, the system consists of three sputtering targets (50 mm diameter) mounted on a transport cart. This system provides the facility to sputter from three target materials separately, and therefore allowed the deposition of multi-layered films. The system comprises a copper sheet (2 mm thick) where the targets are bonded by indium, that acts as a common electrode for the high negative potential. This copper sheet is electrically isolated by four ceramic pieces from the outer stainless steel part of the cart. The cart uses four ball bearings to be transported along two stainless-steel linear guides, which are welded to the sputtering chamber. A magnetic manipulator is used to move the target cart. A grounded shield made of stainless steel was designed and machined. The shield restricts the ion bombardment to the target alone and avoids cross contamination.

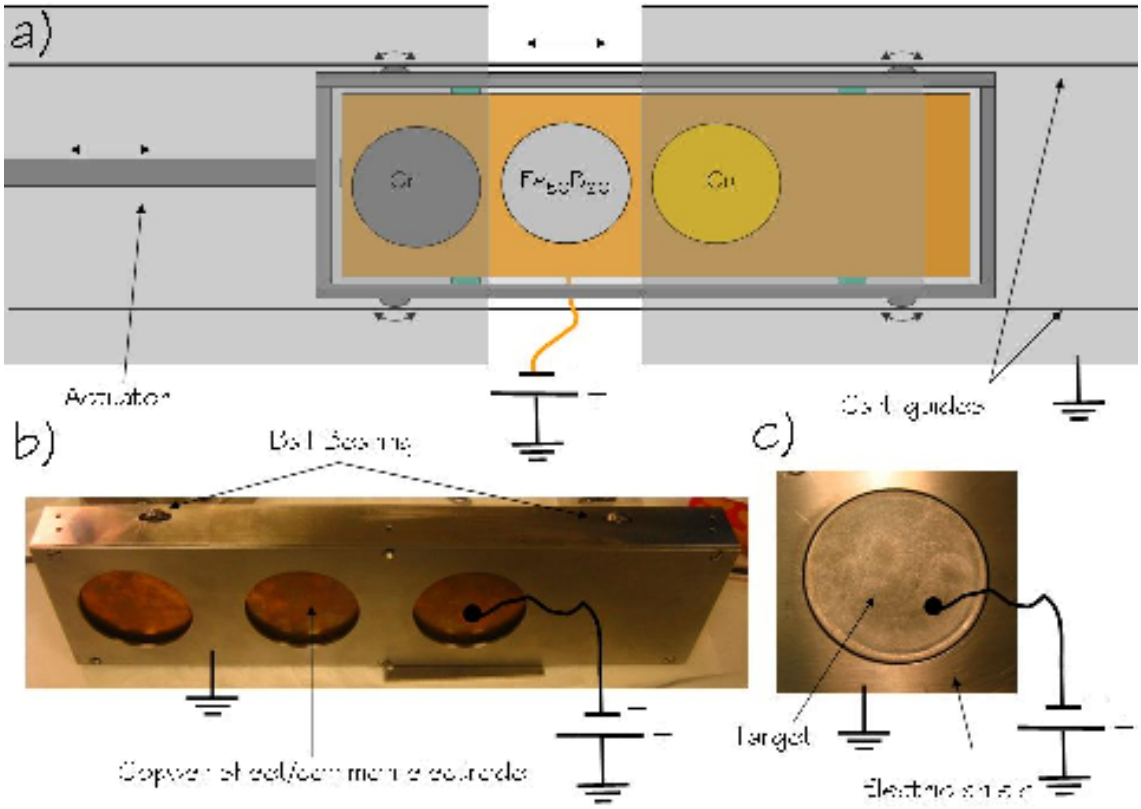

Figure 5 : a) Schematic view of the multi-target sputtering system. b) Picture of target cart. c) Picture of the sputtering target and the stainless-steel shield.

I.3. Accumulated stress in deposited thin films.

It is well known that thin films obtained by Physical Vapour Deposition (PVD) process accumulate large stresses during their preparation [9]. This accumulated stress either originates from strained regions within the films (grain boundaries, dislocations, voids, impurities, etc..) or at the film/substrate (lattice mismatch, different thermal expansion, etc..) and film/vacuum interfaces (surface stress, adsorption, etc..) or is due to dynamic processes (recrystallization, interdifusion, etc...). Since the magnitude of most of these stress contributions is directly related to film morphology, important structural information can be extracted from measurements of the accumulated stress. An *in-situ* characterization of the film accumulated stress can be used to obtain additional information about the growth mechanism of the film, offering also the possibility of real-time control and actuation.

I.3.1. *In-situ* stress measurement of thin films.

The method most commonly used to study accumulated stress of thin films is based on determining the film stress from the curvature that the film induces onto the substrate (in general beams, plates or discs) during deposition. In particular, the cantilever beam technique, that uses a cantilever beam substrate clamped at one end along its width and with the opposite

end remaining free to move [10]. This bending is detected as a change of a capacitance, as a deflection of a laser beam or by using a scanning probe. The easiest method to implement in a UHV chamber is the optical method. In this case, the curvature induced on the cantilever/substrate is measured by using a reflected laser beam from the top side of the substrate to a segmented photodetector, as shown in Figure 6. The cantilever/substrate is clamped from one side. The measured deflections in the photodetector are denoted as Δx.

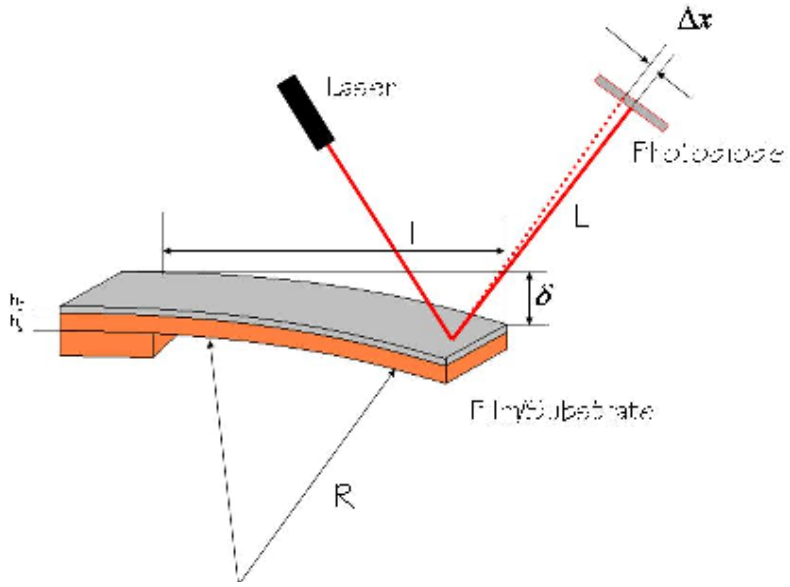

Figure 6. Schematic view of the laser beam curvature measurement.

Changes in the substrate curvature can be directly related to the film accumulated (σ) stress by the well-known Stoney's equation revised for biaxial stress [11],

$$\sigma = -\frac{1}{6}\frac{E_s h_s^2}{(1-\upsilon_s)h_f}\Delta\left(\frac{1}{R}\right) = -\frac{1}{3}\frac{E_s h_s^2}{(1-\upsilon_s)h_f}\frac{\Delta x}{lL} \qquad (1)$$

where $E_s/(1-\nu_s)$ is the biaxial elastic modulus of the substrate, h_s and h_f are the thickness of the substrate and film respectively, and r_0 and r denote the curvature radii before and after the film deposition respectively. The substrate curvature was determined measuring the free end bending using the next geometrical relation

$$\left[\frac{1}{r}-\frac{1}{r_0}\right] = \frac{1}{2}\frac{\Delta x}{lL} \qquad (2)$$

Equation (1) is valid if the following conditions are accomplished [12,13]:

a) Film thickness (h_f) and substrate thickness (h_S) are uniform and much lower that the substrate length (l) and width (w). ($h_S << w, l$);

b) Film thickness is much lower than substrate thickness ($h_f << h_S$);
c) Film accumulated stress has not out of plane components;
d) Substrate material is homogeneous, isotropic and linearly elastic, whilst the film material is isotropic;
e) The effects of the boundaries are negligible and the physical properties are homogeneous at the plane parallel to the interface;
f) Deflections are infinitesimally small, remaining in the elastic regime for the film and substrate;
g) Substrate is not constrained to curve along any direction.

All these conditions are fulfilled in our experiments with relatively small errors.

I.3.2. Relation between film accumulated stress (compressive or tensile) and the sign of the curvature change.

The criteria used in this thesis to connect the sign of the film accumulated stress with the substrate deformation is schematically shown in Figure 7. The film accumulates a compressive stress ($\sigma < 0$) if the substrate curvature is convex, i.e. $\Delta(1/R) > 0$ (Figure 7.a)). For example, this curvature is observed when the lattice parameter of a epitaxially grown layer is higher than that of the substrate. In this case, the layer reduces its lattice parameter to accommodate the lattice mismatch, accumulating a compressive stress negative in sign. On the other hand, the film accumulates a tensile stress ($\sigma > 0$), producing a concave curvature on the substrate $\Delta(1/R)<0$ (Figure 7.b)). For example, this curvature is observed if the lattice parameter of the epitaxially grown ayer is smaller than that of the substrate, the layer expands its lattice parameter to accommodate the lattice mismatch, accumulating a tensile stress positive in sign.

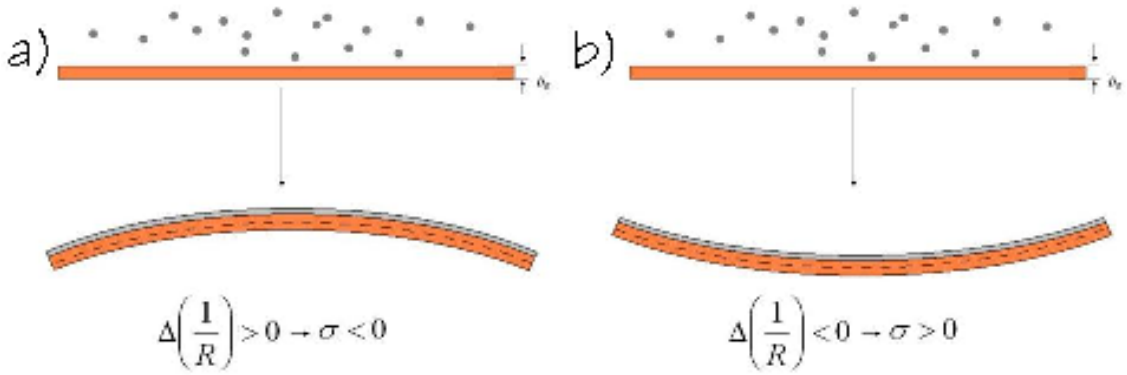

Figure 7 : Relation between the accumulated stress sign and the substrate curvature direction.

I.3.3. Sources of stress in deposited thin films.

In general, thin films contain many defects of different types, which may act as sources of stress [9]. In this section, the most common film stress contributions are discussed and classified according to their range of action, either within the films or at the film/substrate and film/vacuum interfaces.

a) Accumulated stress within the films.

Contribution	Sign	Growth mechanism	Characteristic	Example	
Grain boundaries	$\sigma > 0$	Policrystalline/Amorphous	Low $T/T_{melting}$	Mo at $T \leq RT$	[14]
Re-crystallization	$\sigma > 0$	Policrystalline	High $T/T_{melting}$	Au at $T \geq RT$	[15]
Domain walls	$\sigma < 0$	Epitaxial V-W	Nucleation of domains	Ag on mica	[16]
Lattice expansion	$\sigma < 0$	Policrystalline	Expansion during island size growth	Au islands on C	[17]
Capillarity	$\sigma < 0$	Policrystalline/Amorphous	Expansion at islands coalescence	Continuous Au	[18]
Impurities	$\sigma < 0$	Policrystalline/Amorphous	↑ nucleation / compounds	O_2 on Al	[19]
Ion Peening	**$\sigma < 0$**	**All**	**Atomic displacement**	**Mo at $T \leq RT$**	[20]

b) Accumulated stress in the film/substrate interface.

Contribution	Sign	Growth mechanism	Characteristic	Example	
Lattice mismatch	$\sigma > 0$, $\sigma < 0$	Epitaxial	Pseudomorphic growth	GaP/GaAs	[21]
Interface reactions	$\sigma < 0$	All	Interface compounds	$PtSi_2$ / $PdSi_2$	[22]
Inter diffusion	$\sigma > 0$	All	Diffusion between film and substrate.	Al on AlOx	[23]
$\neq$ thermal expansion coefficient	$\sigma > 0$, $\sigma < 0$	All	Temperature fluctuations.	Au on SiOx	[24]

c) Accumulated stress in the film/vacuum interface.

Contribution	Sign	Growth mechanism	Characteristic	Example	
Surface stress	$\sigma > 0$, $\sigma < 0$	Epitaxial	Surface reconstructions	Al (111)	[25]

In general, several contributions to the film accumulated stress are present, but depending on the deposition method, deposition temperature, base pressure, etc… some contributions are dominant over the rest. As an example, the evolution of the accumulated stress of Cr films for different substrate temperatures is shown in Figure 8. At 300K, the film accumulated stress is clearly tensile, due to the interaction between grain boundaries which

constitute the main defects in columnar grain films. But raising the substrate temperature to 573K, the evolution of the accumulated stress changes, promoting also recrystallization processes after film deposition. Now, the dominant effect to the film accumulated stress is the capillarity and lattice expansion within the deposited islands. This change in the accumulated stress tendency is directly related to a change in the film microstructure, as there is a variation in the $T/T_{melting}$ relation. From the MD model, it is known that thin films deposited at low temperature have a columnar growth, with a very small grain size, but raising the substrate temperature during deposition, the thin film becomes denser, allowing atom diffusion and recrystallization processes.

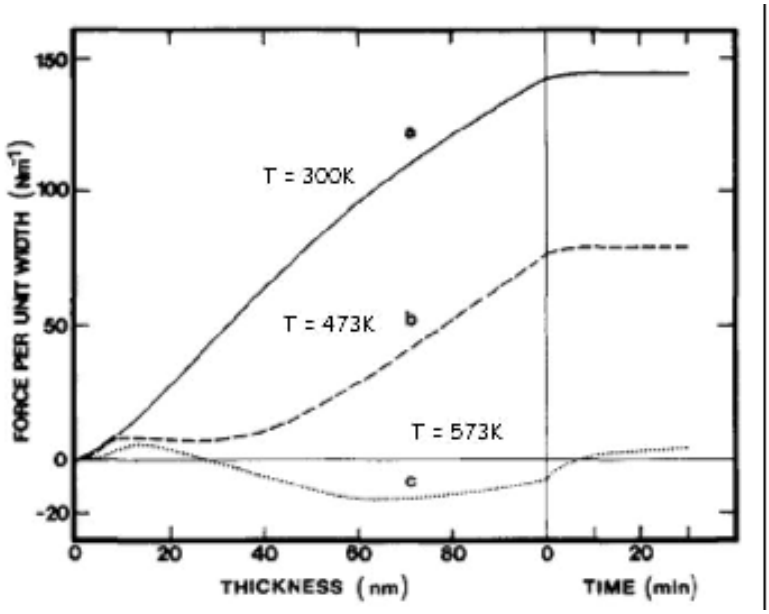

Figure 8 : Evolution of the film accumulated stress, denoted as 'Film forces per unit width' as a function of the deposited thickness (during deposition) and time (alter deposition) of Cr films evaporated at different substrate temperatures.

I.3.4. Stress in sputtered films: 'atomic peening' effect.

As shown before, the film microstructure, and consequently the film accumulated stress, depends strongly on the deposition parameters. In particular, for thin films deposited by sputtering techniques, it is necessary to take into account the following deposition parameters that influence the film microstructure:

a) Substrate temperature : alters the adatom surface mobility.
b) Working gas pressure : higher pressures promotes an increase in the number of collisions between atoms and gas, reducing its energy and randomize their direction.
c) Mass of the working gas species (typically Ar, Xe, Kr) : the quantity of energy lost by the sputtering atoms in collisions with atoms in the sputtering gas is different.

d) Deposition rate: faster rates restrict surfaces mobility.

e) Angle of deposition of the incoming flux.

f) Target to substrate distance : increasing the separation has the effect of increasing the number of collisions between atoms and gas, lowering the energy of the arriving atoms.

g) Target potential : imposes the initial energy of the sputtered atoms.

The accumulated stress in sputtered thin films is generally compressive, due to the energetic particle bombardment of the film surface during film deposition, or the called “atomic peening effect” [26]. The particles may be sputtered atoms which arrive to the substrate with much of their initial kinetic energy, or working gas atoms back-reflected in the target. The momentum of impact is sufficient to disturb the previously condensed material, packing it together. In the case of materials with high melting points, i.e. low adatom mobility during film deposition, the distortion introduced by the energetic atoms can not be relaxed and accumulates almost linearly with film thickness. This bombardment gives rise to a evolution of the accumulated stress linear and in the compressive direction ($\sigma < 0$). In the case of amorphous thin films (very low adatom mobility) deposited by sputtering, this is the main factor that gives rise to an accumulated stress in the film. However, for low melting point materials, i.e. high adatom surface mobility during film deposition, this distortion can be relaxed.

The “atomic peening” effect depends strongly on the energy of the arriving particles, either sputtered atoms or gas neutrals. In a sputtering system with a fixed target to substrate distance, the value of this energy is controlled by the target potential (initial energy of the sputtered/back-reflected atoms) and the working pressure (number of collisions with the working gas atoms). An important parameter is the thermalization distance , or the distance at which the kinetic energy of the arriving atoms is lost (k_BT = 25meV) [27-28]. This value can be calculated as :

$$d = n \cdot \lambda \qquad (3)$$

where *n* is the number of collisions at which the energy of the sputtered/back-reflected atoms is reduced to the average energy of the gas atoms, and λ is the mean free path of an atom travelling through a gas. This thermalization distance depends strongly on the mass and initial energy of the atoms.

It has been shown that films deposited with enhanced energy of the arriving atoms, i.e., in a state of high compressive stress ($\sigma < 0$), show a denser microstructure [29]. The energetic particles striking the surface limit the columnar growth morphology and displaces atoms into denser sites than the equilibrium structure contains. However, lowering the energy of the arriving atoms (increasing pressure or lowering target potential), the columnar structure

resulting from the self-shadowing of the incident atoms by those already incorporated into the growing film develops, changing the sign of the film accumulated stress ($\sigma > 0$). In this case, the interaction between columns (high surface tension of the inner surface of the voids) is the source of the film accumulated stress. This is illustrated in Figure 9 for sputtered Mo films, where a correlation between the film accumulated stress and the Mo microstructure imaged by Transmission Electron Microscopy (TEM) is shown for various sputtering pressures.

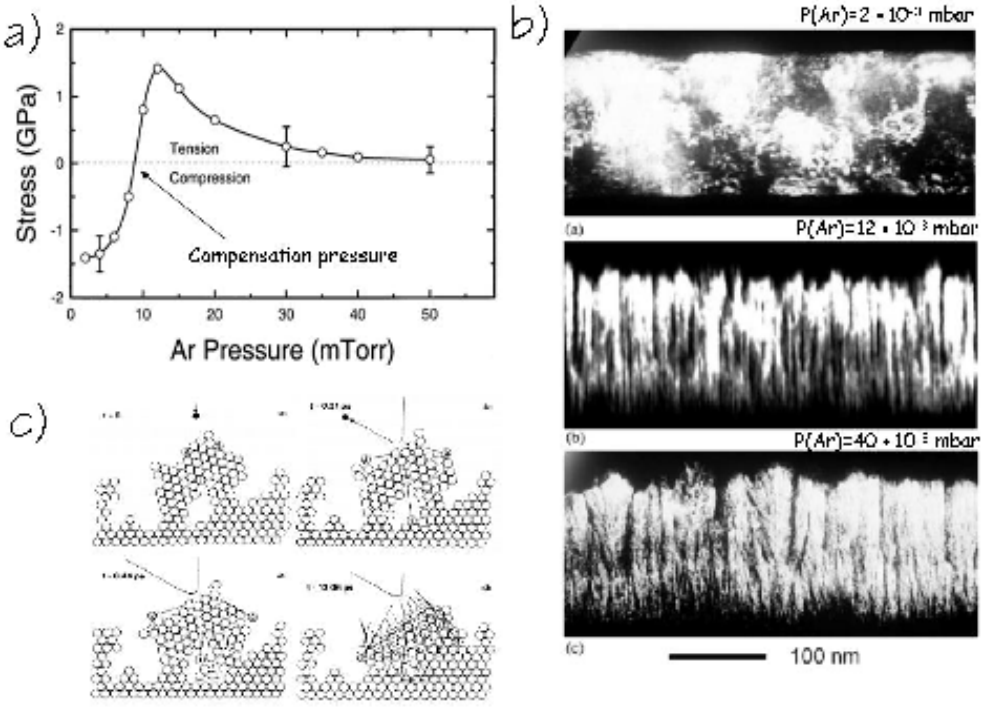

Figure 9 : a) Accumulated stress of a sputtered Mo film as a function of the Ar sputtering pressures [30]. *b) TEM images showing the microstructure of three Mo films deposited under different Ar sputtering pressures. c) Schematic picture of the distortion induced in a porous deposited film by the bombardment of a energetic particle. The microstructure becomes denser.*

For amorphous deposited films, there is a set of deposition parameters at which the accumulated stress of the deposited film is compensated, due to the competition between the "atomic peening effect" compressive (low pressures combined with high target potentials) and the interaction between columns tensile (high pressures combined with low target potentials). These paremters (the target potential, working pressure, target-to-substrate distance, etc…) are intrinsic to each sputtering system. This value is very appealing from the technological point of view, as for example for the use of sputtered magnetostrictive films in micro-electro-mechanical systems (MEMS), where undesirable bending of the device must be avoided.

I.3.5. Experimental set-up at the IMM for *in-situ* stress measurement.

A schematic view of the experimental configuration for the *in-situ* stress measurement during sputtering deposition is shown in Figure 10. The cantilever orientation and that of the

optical detection system have been rotated 90º in the figure with respect to their real orientation for clarity reasons. The glass substrate cantilevers were 4 mm wide, 16 mm long and 0.125 mm thick. The cantilever/substrate is positioned inside the chamber, mounted on a clamped stainless-steel substrate holder, and clamped with a tungsten wire from one side. The substrate holder contains two metallic shields, avoiding heat radiation from the filament and consequently undesirable substrate bending. The incidence angle of the laser was almost normal. The laser beam deflections are measured in a segmented photodetector and denoted as Δx. The segmented photodetector detector consists of two sectors with a separation of about 200 μm connected in opposition to detect the difference between the laser beam intensity impinging on each sector, coupled to a low noise DC preamplifier and adequately filtered with a band pass 0-10 Hz. Sensitivity was of the order of 1mV/μm. A green Ar laser (λ = 532 nm, 1.5 mW), was used as a light source. It was found that the lateral stability of the beam during long time measurements was superior to that of red HeNe lasers. The initial substrate curvature r_0 was negligible.

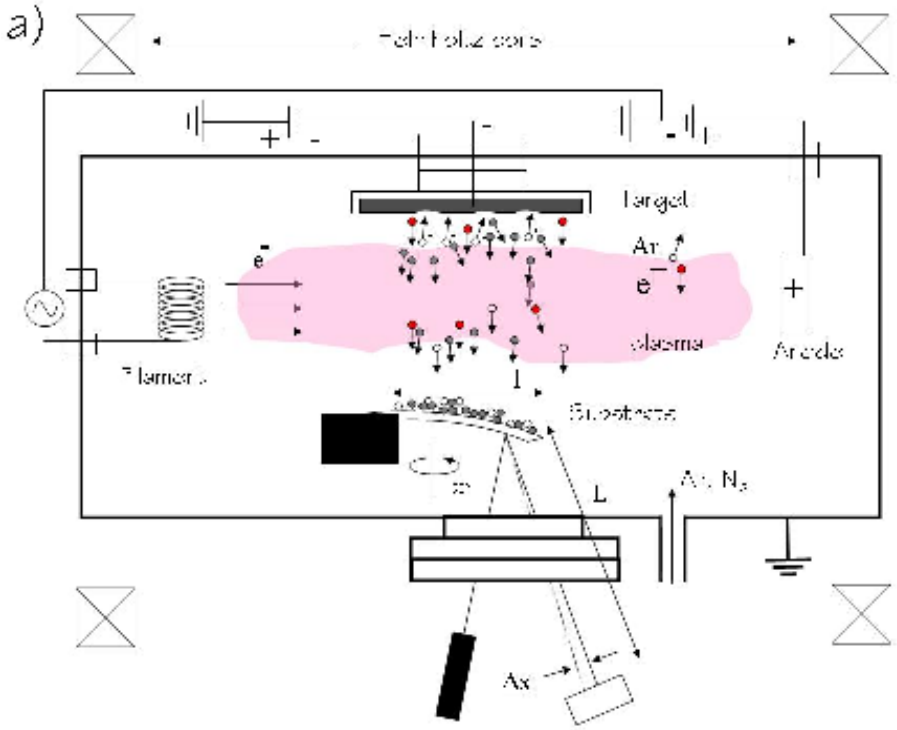

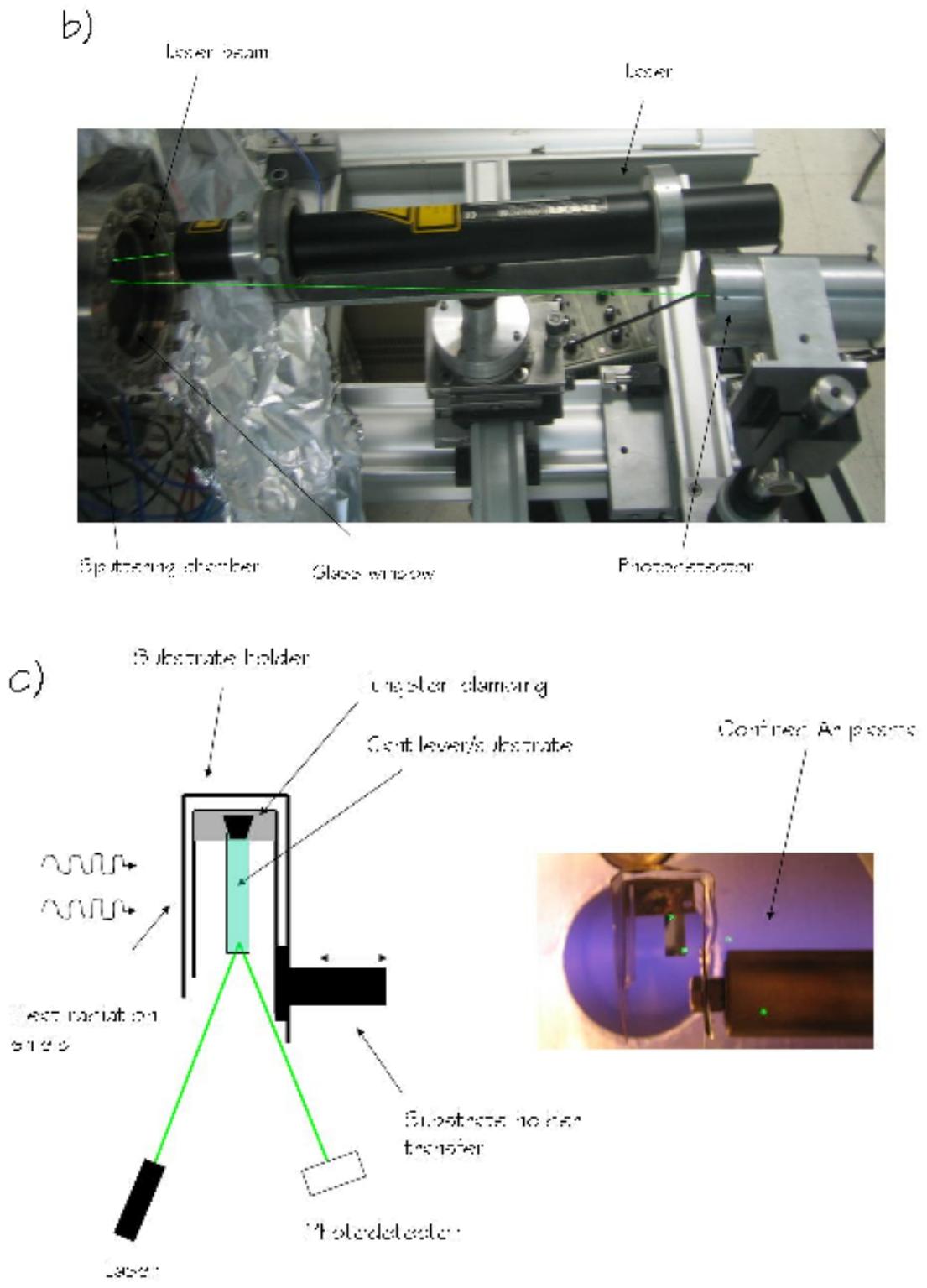

Figure 10 : a) Schematic diagram of the experimental setup dedicated to the in situ stress measurement during sputtering deposition. The laser incidence plane together with the geometry of the substrate/cantilever is rotated 90° in the picture for clarity reasons. b) Picture of the laser and segmented photodetector used for stress measurement. c) Schematic view of the substrate/cantilever mounted on a stainless-steel substrate holder. Picture of the cantilever beam and substrate holder during stress measurement. Notice the confined plasma.

I.4. Magnetic characterization techniques.

I.4.1. Principles of Magneto-Optical Kerr Effect (MOKE).

In this thesis, the films magnetic characterization was performed using MOKE techniques. In 1845 Michael Faraday [31] noticed that when the electromagnetic radiation passes through a magnetized material its polarization characteristics and/or intensity are modified. Some years later, in 1876, John Kerr [32] observed that the direction of vibration of plane polarized light was altered when the polarized ray was reflected from a mirror placed in a magnetic field. These modifications are known as magneto-optic (MO) phenomena. In particular, they are known by the name of the discoverers: the MO Faraday and Kerr effects. Both are related to the rotation of the plane of polarization of an incident plane polarized beam when it reflects (Kerr effect) or passes through (Faraday effect) a magnetized sample. The magneto-optic Kerr effect (MOKE) can be classified in three different configurations depending on the relative orientation of the magnetization of the sample *M* with respect to the sample surface and the plane of incidence. In this thesis, only the transversal Kerr effect geometry (the magnetization is within the sample plane and perpendicular to the plane of incidence) is used. This configuration can be seen in Figure 11.

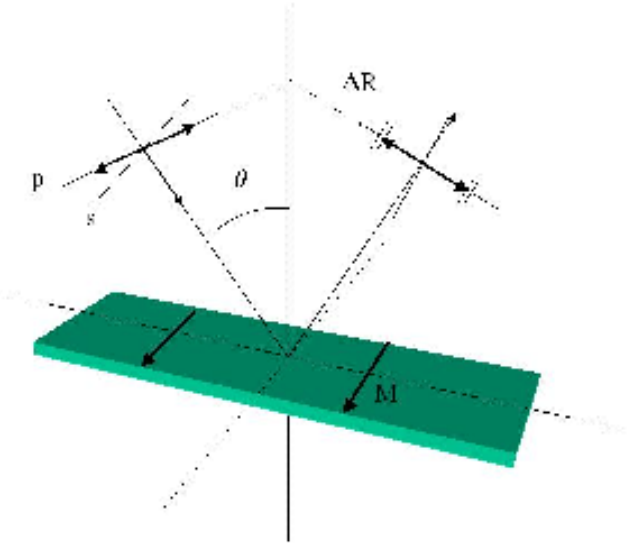

Figure 11 : Schematic of the transversal Kerr effect configuration.

The transversal Kerr effect is rather special since the effect consists of a modulation of the intensity of the light. The transversal MOKE setup uses this property to obtain B-H hysteresis loops of magnetic samples with in-plane magnetization. The relative reflectivity variation can be expressed as

$$\frac{\Delta R_{pp}}{R_{pp}} = \frac{R_{pp}(M_S) - R_{pp}(0)}{R_{pp}(0)} \qquad (4)$$

where $R_{pp}(Ms)$ is the *p*-reflectivity at saturation and $R_{pp}(0)$ is the *p*-reflectivity at zero field.

I.4.2. Experimental set-up at the IMM : Transversal Kerr and magneto-optical torque.

In the IMM setup, a He-Ne laser (λ=630 nm, 1.5 mW), that emits linearly polarized light, is used as a light source. The emitted light is focused by a lens and then hits the sample, that is placed into the Helmholtz coil. The reflected light is polarized and the intensity of the resulting beam is measured by a photodetector. Depending on the width of the reflected beam, a second lens might be used to focus the reflected light into the photodetector. According to what was previously explained, both polarizers should be in *p* position in order to maximize the ratio between the Kerr signal and the DC-signal. Moreover, an adjustable attenuator is also used to fine-tune the intensity of the reflected beam within the optimal range of the photodiode. The Helmholtz coil provide the external uniaxial field perpendicular to the plane of incidence. The coil is fed with a sinusoidal current and provides 70 Oe per ampere circulating through the windings. This sinusoidal current is controlled by a wave generator set at 5.1 Hz. This is very important since the simple setup itself is quite noisy due to laser light instability, ambient light and mechanical vibrations of the setup. Thus, provided an oscilloscope capable of averaging the signal received by the photodiode, low noise hysteresis loops might be easily obtained with no bandwidth loss. As mentioned above, the light intensity measured in the photodetector consists of two contributions. One of them is the reflected intensity (or DC-intensity) and the other one is the Kerr contribution. The latter represent a few fraction of the whole intensity so previously to the intensity enhancement in the oscilloscope, the DC component must be removed using a compensator.

The B-H hysteresis loops are finally obtained setting the intensity supplied to the coils as the X axis (which is proportional to the external applied field) and the Kerr component of the reflected intensity as the Y axis (which is proportional to the magnetization in the sample).

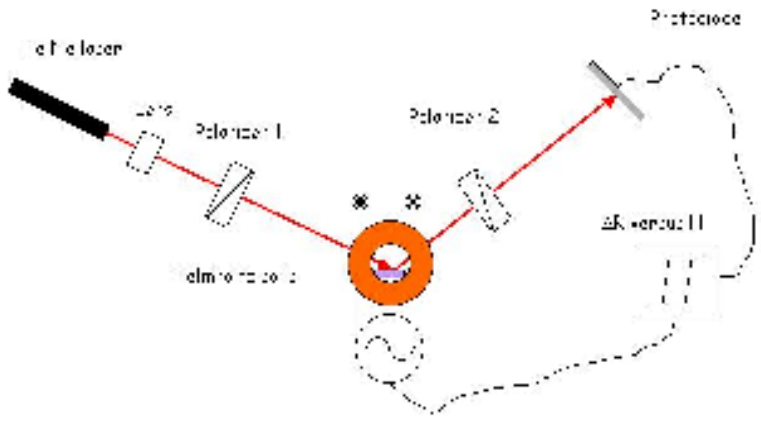

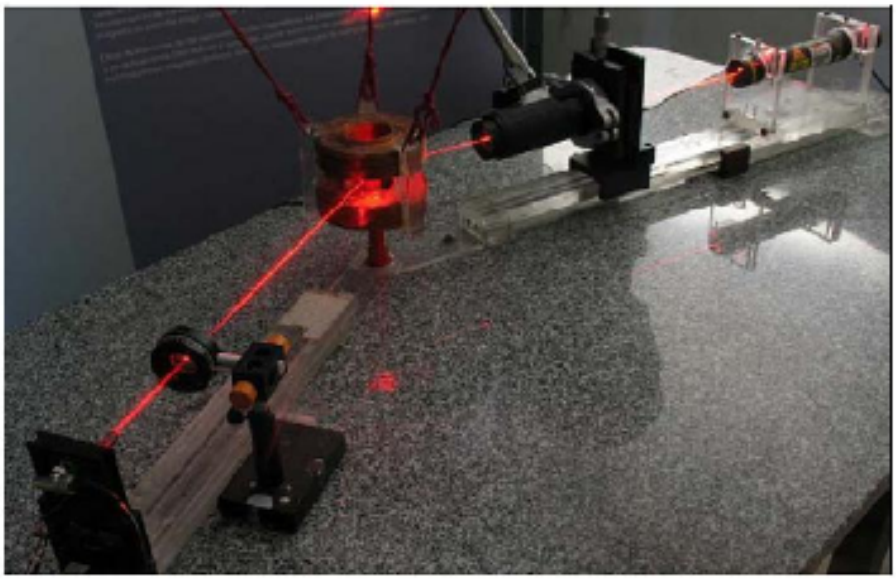

Figure 12 : Transversal Kerr schematic picture and picture of the IMM setup. The light from the He-Ne laser, focused by a lens is then p-polarized by Polarizer 1. After being reflected by the sample S, the beam is then p polarized by Polarizer 2. The resulting signal is then collected in a photodiode and sent to an oscilloscope (Y axis) together with the current supplied to the coils (X axis).

The magneto-optical torque method [33] was developed at the IMM. It is used to measure the magneto-optic response of the sample to a rotating magnetic field. The advantage of this method is that with a single measurement the anisotropy constants and their symmetry axes distribution is obtained. When a magnetic field *H* is applied in the plane of the sample, and its magnitude is high enough to guarantee a single domain state in every direction, the dependence of the reflectivity (R_{pp}) on the direction of the applied magnetic field (α) can be expressed, up to a second order terms in the magnetization, as

$$R_{pp}(\alpha) = R_0 + A\cos(\theta) + B\cos^2(\theta) \qquad (5)$$

where θ is the angle between the saturation magnetization and the axis perpendicular to the plane of incidence. A and B are coefficients which depend on the wavelength and the angle of incidence, for non-normal incidence B is much smaller than A (in our case B is typically 1% - 5% of A). This expression is derived from the reflection coefficient R_{pp} which quantifies the amplitude of the reflected p-polarized light into p-polarized light and is valid only when both the incident and the reflected light are p polarized (equation (5)).

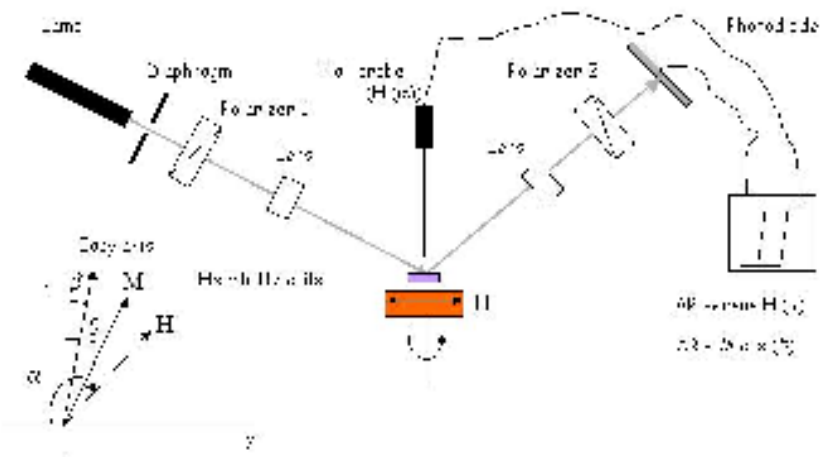

Figure 13 : Schematic picture of the magneto-optical experimental setup. a) The light from the lamp, is then p-polarized by Polarizer 1 and focused by a lens. After being reflected by the sample, the beam is focused by a second lens and p polarized by Polarizer 2. The resulting signal is then collected in a photodiode and sent to an oscilloscope (Y axis) together with the current supplied to the coils (X axis).

Therefore, the evolution of ΔR_{pp} = R_{pp} (α) - R_0 versus α represents a direct measurement of the changes in the direction of the magnetization as the magnetic field rotates.

For a continuous $Fe_{80}B_{20}$, the dependence of the reflectivity on the angle α for different values of the applied field magnitude H is shown in Figure 14. The easy axis is set perpendicular to the plane of incidence, parallel to the x axis. As we increase the magnetic field amplitude the shape of the signal is strongly modified. The observed changes reflect the variation of the angle between the applied field H and the saturation magnetization ('phase difference'). For a single domain system, this angle can be calculated by minimizing the magnetic free energy, which for the system sketched in Figure 10 can be expressed as:

$$E = K_u sen^2(\theta - \beta) - M_S H \cos(\alpha - \beta) \qquad (6)$$

where K_u is the uniaxial anisotropy constant, M_s is the saturation magnetization of the sample, H is the applied magnetic field, and β is the angle between the easy axis and the x axis.

Deriving the equation (6), it is obtained the projection of the magnetization along the x axis ($cos(\theta)$) as a function of the angle α,

$$\cos\theta = \cos\left(\alpha - arcsen\left(P_1\right) \cdot sen\left(2\left(\theta - P_2\right)\right)\right) \qquad (7)$$

where $P_1 = Ku/M_s H$ and $P_2 = \beta$.

The parameters P_1 and P_2 are obtained adjusting the measurement of $\Delta R_{pp}(\alpha)$ to the equation (7). These values determine the phase difference between the field and the magnetization, and the easy axis angle, respectively.

In the IMM setup, a magnet is mounted on a rotation stage driven by a electrical motor. The frequency of the rotation can be changed between 10 and 40 Hz. A light source is focused on the sample. The reflected p-polarized light is then focused to a Si photodetector. The signal from the photodetector is compensated from the direct-current (dc) offset and amplified. The measured signal is periodic, with a period that coincides with the rotating magnet. The angle of the applied rotating magnetic field with the plane of incidence (α) is monitored with a Hall probe.

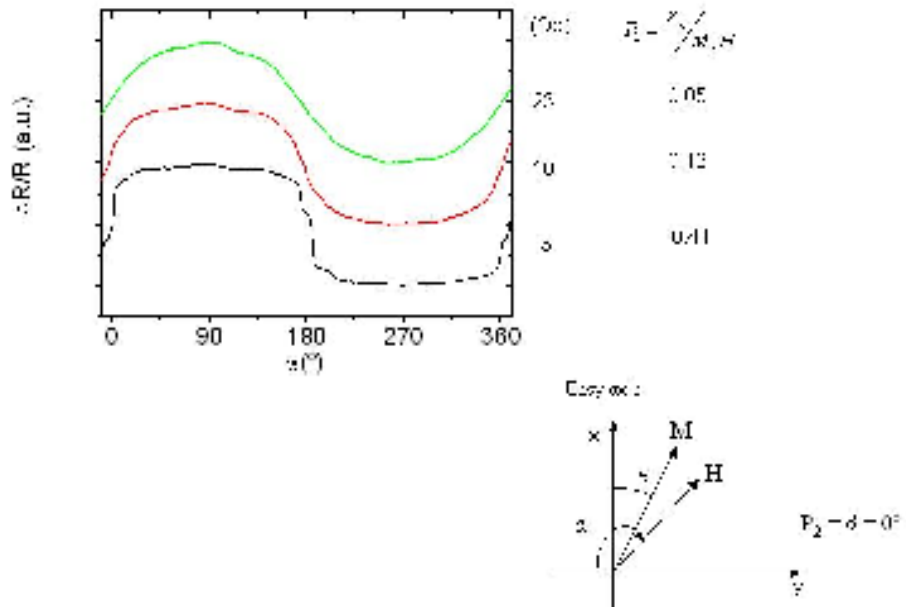

Figure 14 : Angular dependence of the reflectivity and the corresponding estimated parameters.

The angular dependence of the reflectivity as a function of the angle of the applied magnetic field is represented in Figure 14 for different *H* field magnitude values. The P_1 and P_2 parameters are calculated, giving rise to a anisotropy constant value of K_u = 1235 erg • cm $^{-3}$, which easy axis points parallel to the x axis. For this sample, the saturation magnetization M_s (1058 emu • cm $^{-3}$) was obtained by SQUID measurements

I.4.3. Magneto-elastic effects: Magnetostriction.

Magnetostriction is an abbreviation for Magneto-elastic-interaction. The effect was discovered as long ago as 1842 by Joule. As shown in Figure 15, when a substance is exposed to a magnetic field, its dimensions change [34]. This effect can be described as a coupling between the magnetic and elastic “subsystems” of a material. The change in dimension connected with the magnetization process is termed linear magnetostriction. The

deformation $\Delta l/l$ at magnetic saturation is called the saturation magnetostriction constant, λ_S. This value is usually small (~ 10^{-5}), intrinsic to the material and can be positive or negative.

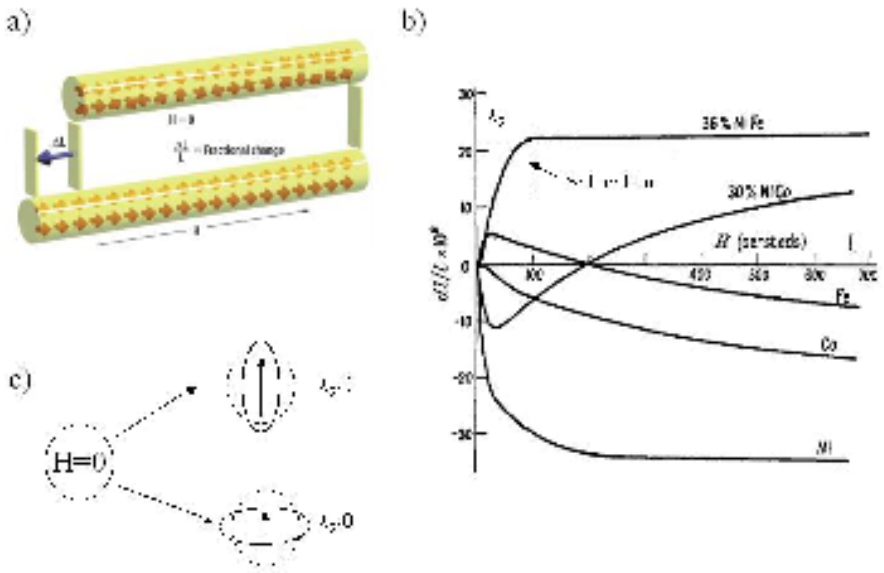

Figure 15 : a) illustration of the deformation (ΔL) induced in a bar with length L, while the magnetic domains are aligned parallel to the applied magnetic field. b) Evolution of the magnetostriction (λ=dl/l) as a function of the applied magnetic field. λ_S is the saturation magnetostriction coefficient. c) Schematic picture of Joule magnetostriction of a spherical sample with positive and negative magnetostriction coefficient. The spherical sample is transformed into a ellipsoid.

Cobalt is the pure material with higher λ_S at RT (-60 • 10^{-6}). Between the alloys, the highest Joule magnetostriction which has ever been observed at room temperature (RT) is that of Terfenol-D [35] (Ter : terbio, Fe:iron, NOL :"Naval Ordnance Laboratory and D : disprosium) with $\lambda_S \sim 10^{-3}$. In the case of the $Fe_{80}B_{20}$ amorphous alloy, the theoretical value is $\lambda_S = 32 \cdot 10^{-6}$ [36]. Due to its soft magnetic properties, this alloy is interesting because the maximum deformation or λ_S are obtained with smaller values of applied magnetic field.

Together with the deformation parallel to the applied magnetic field $\lambda_{||}$, there is a deformation in the perpendicular direction $\lambda_{\perp}$, as observed in Figure 16. The value of that deformation is $-\lambda_S/2$. Thus, the magnetostriction coefficient λ_S can be expressed as $\lambda_S = 2/3\ (\lambda_{||} - \lambda_{\perp})$, independently of the demagnetised state.

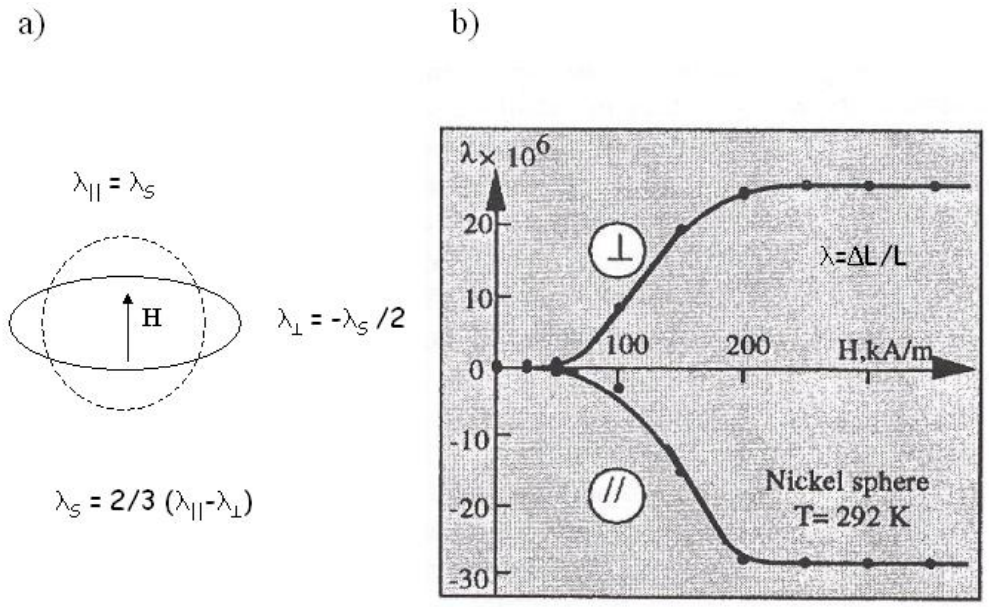

Figure 16 : a) Parallel ($\lambda_{||}$) and perpendicular/transversal ($\lambda_\perp$) deformation of a spherical sample for an applied magnetic field. b) Evolution of the magnetostriction (λ=dl/l) as a function of the applied magnetic field in the parallel (||) and perpendicular ($\perp$) direction corresponding to polycrystalline nickel (Etienne du Trémolet de Lacheisserie 'Magnetostricition : Theory and Aplications of Magnetoelasticity ' (CRC Press, 1993).

The value of λ_S in amorphous alloys is not, in general, smaller that the crystalline relatives. Actually, it is not clear how the magnetostriction value changes form an ordered to a disordered state. For example, it has been seen that the crystalline Co has a larger magnetostriction coefficient as compared with its alloys, as opposite to Fe.

When a magnetic field is applied to a ferromagnetic material, the domain structure changes in such a way as to increase the average magnetization parallel to the field. This can be accomplished in two ways: by a rotation of the magnetization or by a domain wall movement, as observed in Figure 17. This defines the two possible magnetization processes in any ferromagnetic substance. In amorphous ferromagnetic materials, both the rotation of the magnetization and the domain wall movement happen for lower fields than in their crystalline relatives. With respect to the magnetostriction, the change in dimensions is always associated to magnetization rotation [34]. Thus, while the magnetization is an odd function of the applied magnetic field, the magnetostriction is an even function of *H* in ferromagnets, as shown in Figure 17.

.

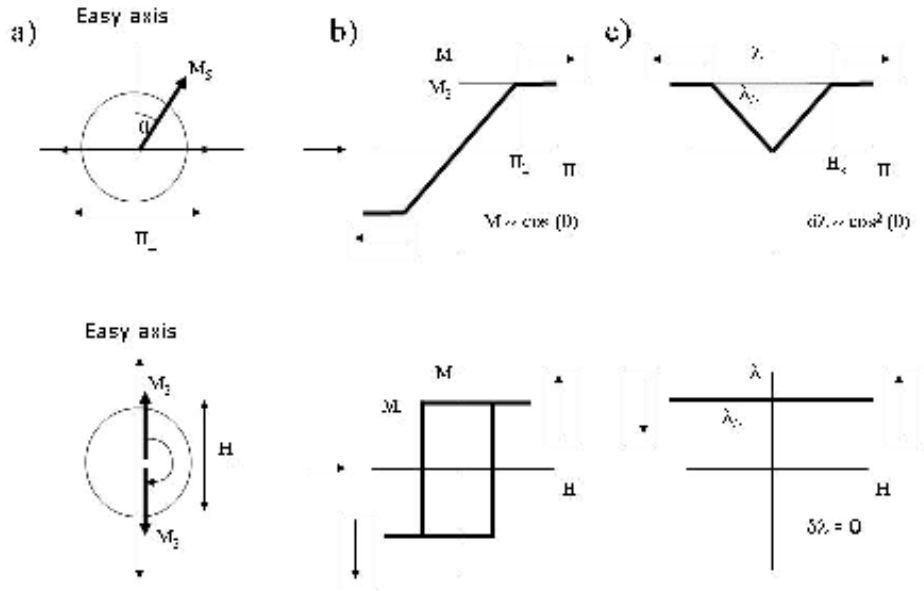

Figure 17 : a) Magnetization process of a single uniaxial ferromagnetic domain. θ is the angle between the applied magnetic field ad the easy axis. b) Magnetization as a function of the applied magnetic field H, when H is applied parallel or perpendicular to the easy axis. c) Magnetostriction as a function of the applied magnetic field (H), when H is applied parallel or perpendicular to the easy axis.

The magnetostriction varies not only with the magnetic field and the temperature, but also with the mechanical stresses. This stress dependence of the magnetostriction consists mainly in the modification of the shape of the M(H) curves -and hence of the λ(H) curves-, while the value of the saturation magnetostriction coefficient is usually nearly stress-independent. An inverse magnetostrictive effect, sometimes called Villary effect, is the dependence of the magnetization process on the stress. In the presence of an external or internal stresses, the magnetization will couple with the stresses via the magnetostriction to induce preferred directions for the magnetization. This coupling between the magnetization is dependent on the sign of λ_S and the stress as illustrated in Figure 18. For materials with $\lambda_S > 0$ the magnetization will rotate so as to lie along the direction of the uniaxial tensile stress, whereas it will lie perpendicular to an uniaxial compressive stress. The reverse is true for materials with $\lambda_S < 0$ as shown in Figure 18.

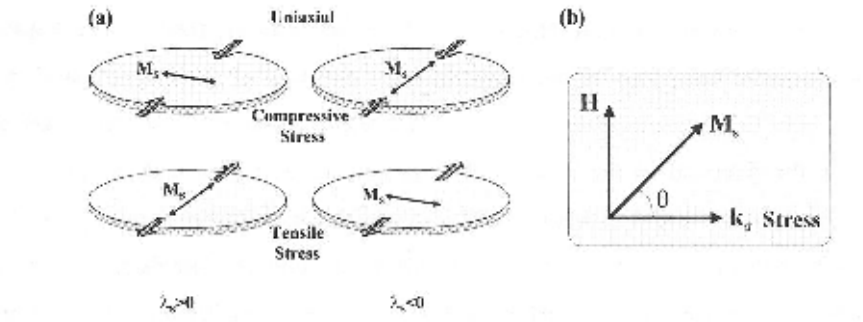

Figure 18 : Illustration of the stress induced anisotropy in positive and negative magnetostrictive materials. a) Anisotropy induced when an uniaxial compressive or tensile stress exists. B) Diagram illustrating the relationship between the stress and magnetization.

I.4.4. Experimental set-up at the IMM : Magnetostriction measurement.

The saturation magnetostriction constant can be determined both directly or indirectly. In indirect methods the stress sensitivity of a suitable magnetic property is analysed, as for example the magnetic anisotropy (Chapter III, Section III.2.2.). Direct measurements evaluate the elongation of a magnet depending on the magnetization direction. Every direct determination of a magnetostriction constant requires the measurement of a change in length between two different saturated states, usually parallel and perpendicular to the measuring direction.

For thin films there is a convenient direct method, the beam deflection method, that provides a reliable direct way for measuring magnetostriction [37]. A magnetostrictive thin-film material deposited on a nonmagnetic substrate is subjected to a magnetic field. As the magnetization rotates, the thin film expands (or contracts), creating a stress on the substrate, which causes the substrate and film to bend. Typically, a rectangular cantilever sample is clamped on one end and the deflection of the free end is measured, for example reflecting the laser beam from the free end of the cantilever to position sensitive photodetector, as observed in Figure 19.

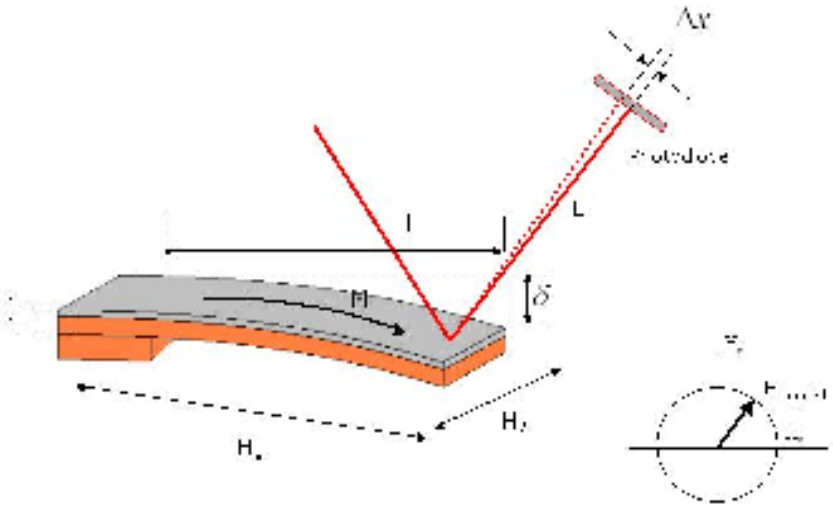

Figure 19 : Schematic of the direct magnetostriction measurement. A laser beam is reflected at the free end of the cantilever. Its deflection (δ) during magnetostrictive strain is measured at a two quadrants photodiode. L is the cantilever length, L Is the distance between the cantilever and the photodiode and Δx is the deflection measured at the photodiode.

The theory of elasticity [37] yields the following relation between the magnetostriction constant λ_S and the deflection of the free end of the cantilever for longitudinal δ_x and transverse δ_y magnetization. The result for a freely deformable and elastically isotropic substrate material is

$$\lambda_S = \frac{2}{3}(\lambda_x - \lambda_y) = -\frac{2}{9}\frac{\delta_x - \delta_y}{l^2}\frac{E_s h_s^2 (1+\upsilon_f)}{E_f h_f (1+\upsilon_s)} \quad (8)$$

where E_s , E_f , ν_s , ν_f , h_s and h_f are the Young's modulus, Poisson's ratio and thickness of the thin film and substrate respectively.

The magnetostrictive bending is detected optically by reflecting a laser beam from the free end of the cantilever to a two-quadrants photodetector, as illustrated in Figure 19. Using the following geometric relation:

$$\frac{\delta}{l} \approx \frac{\Delta x}{L} \quad (9)$$

where L is the distance between the substrate ad the photodiode, and Δx is the displacement measured in the photodiode, the equation (8) can be expressed as:

$$\lambda_S = -\frac{2}{9}\frac{\Delta x_{fot,x} - \Delta x_{fot,x}}{l \cdot L}\frac{E_s h_s^2 (1+\upsilon_f)}{E_f h_f (1+\upsilon_s)} \quad (10)$$

A magnetostriction measurement setup was designed and built at the IMM. A He-Ne laser (λ = 630 nm, 1.5 mW) is used as a light source. The emitted light hits the free end of the cantilever beam device at an angle close to normal incidence (85º). The cantilever is mounted in the centre of two orthogonal pairs of Helmholtz coils, that provide the external uniaxial or rotating field in the plane of the sample. The coils are fed with a sinusoidal current and provides 70 and 135 Oe per ampere circulating through the windings respectively. This sinusoidal current is controlled by a wave generator set at 5.1 Hz. A two quadrants photodetector with an integrated pre-amplifier is used to measure the laser beam deflection. Thus, provided an oscilloscope capable of averaging the signal received by the photodiode, low noise magnetostriction loops might be easily obtained with no bandwidth loss. The magnetostriction loops are finally obtained setting the intensity supplied to the coils as the X axis (which is proportional to the external applied field) and measured deflection in the photodetector as the Y axis (which is proportional to the magnetostriction strain).

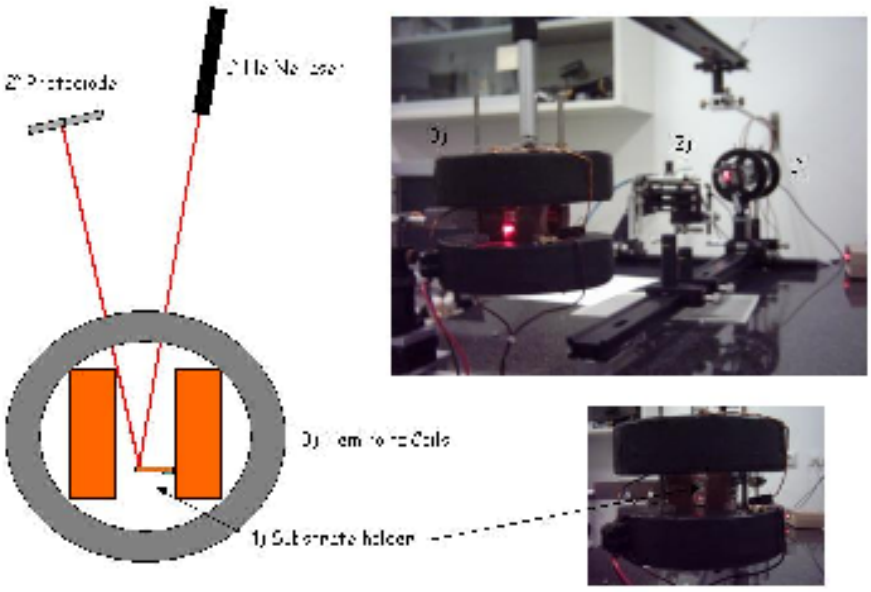

Figure 20 : Magnetostriction measurement sketch and IMM setup.

Two different kind of measurements were done, depending on the configuration of the applied magnetic field. For an exact measurement of the magnetostriction coefficient λ_S, the magnetic thin film is exposed to a rotating magnetic field parallel to the sample plane. A single domain state is ensured in every field direction. In this case, the measurement is independent of the initial demagnetised state (An experiment with a field applied along only one axis of a crystal yields no useful information on the magnetostriction constants, because then only some arbitrary demagnetised state and the saturated states can be compared). As no difference in the field-induced strain along the cantilever occurs for a 180º change in magnetization direction, magnetization rotating at a frequency ***f*** will produce at zero field a deflection that oscillates at a frequency 2*f*, as observed in Figure 21. The normalized magnetostriction (λ/λ_s) and the magnetization (*M*) are shown as a function of the angle θ of the applied magnetic field with the easy axis direction. From this measurement, the angle of the easy axis can be extracted, corresponding to a minimum of deformation or $\lambda(\theta)$. In this case, the easy axis is at $\theta \approx$ *-10, 170*º. For this measurement, a rotating magnetic field of amplitude 150 Oe was applied. The value of the magnetostriction coefficient was estimated from eq. (8). A 50nm thick $Fe_{80}B_{20}$ thin film was deposited onto a glass substrate cantilever, which dimensions were 4 mm wide, 16 mm long and 0.125 mm thick. The distance between the photodiode and the substrate was 1m.

Unfortunately, the values of the Young's modulus and the Poisson's ratio were not available for amorphous sputtered $Fe_{80}B_{20}$ films. Those values were assumed to be the same as that of $Fe_{80}B_{20}$ ribbons, 0.3 [38] and 166 GPa [39] respectively. The strain state and the structure of the ribbon and film are likely different, with the possibility of different mechanical properties. The uncertainty in the elastic constants gives a systematic error, which is much

greater than the errors in the magnetostriction measurement setup. On the other hand, Young's modulus and the Poisson's ratio of the glass substrates were obtained from the manufacturer [40]. These values are 60-80 Gpa and 0.22 respectively. The obtained magnetostriction coefficient of the amorphous $Fe_{80}B_{20}$ thin film was $\lambda_s = 27 \cdot 10^{-6}$, quite close to the one reported in the literature $\lambda_S = 32 \cdot 10^{-6}$ [36].

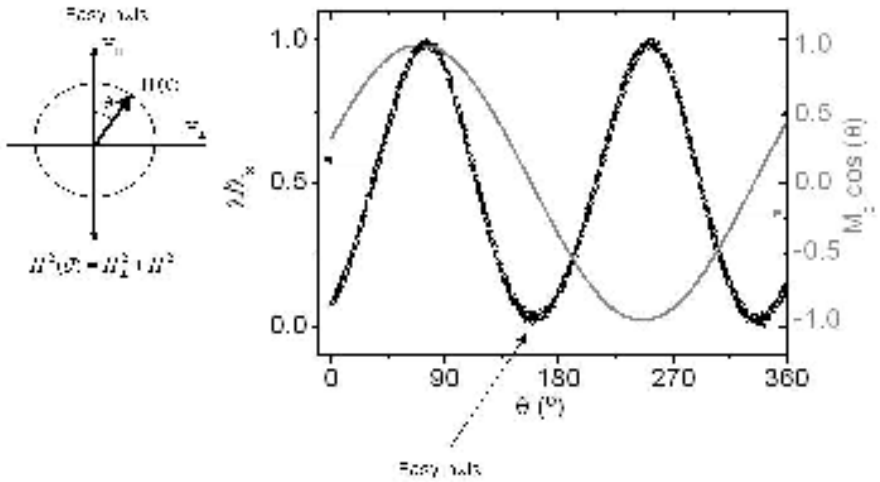

Figure 21 : Evolution of the normalized magnetostriction and magnetization as a function of the angle θ of the applied magnetic field with the easy axis direction for a amorphous $Fe_{80}B_{20}$ thin film of 50nm thickness. A rotating magnetic field is applied in the plane of the sample, ensuring that the sample is magnetically saturated in every direction.

If the magnetic filed is applied parallel to a given direction, the magnetostriction loop is also measured, being interesting for evaluating the magnetization process. In this case, an uniaxial magnetic field is applied along a direction using a Helmholtz coil independently. Information about the anisotropy field is obtained, as observed in Figure 22. For this measurement, a magnetic field of amplitude 150 Oe was applied parallel to the hard axis direction. The obtained anisotropy field was H_k =13 Oe.

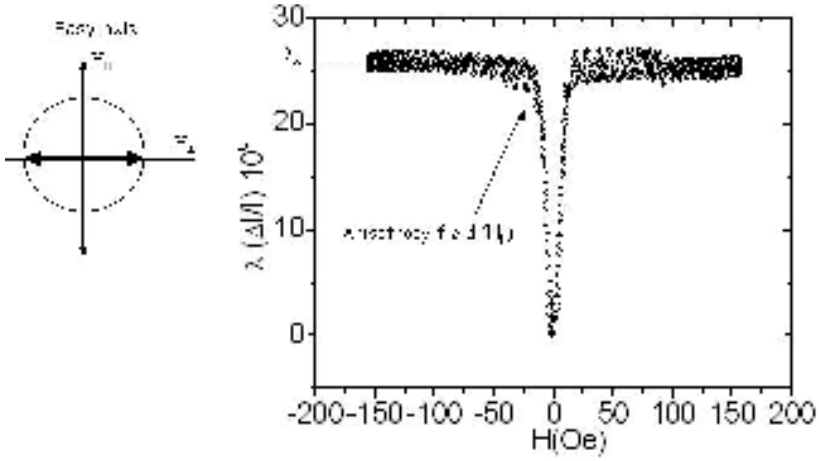

Figure 22 : Evolution of the magnetostriction as a function of the applied magnetic field parallel to the hard axis direction. A value of the anisotropy field is obtained.

I.5. Molecular Beam Epitaxy (MBE).

A III-V Molecular Beam Epitaxy (MBE) system was used in this thesis to grow the multilayer heterostructures for nano-electro-mechanical systems (NEMS) fabrication. There are different heteroepitaxial techniques to grow semiconductor heterostructures. The two most commonly employed are metal organic chemical vapour deposition (MOCVD) and molecular beam epitaxy (MBE). MOVCD is desired over MBE for production optoelectronic devices, mainly because it allows simultaneous deposition on several wafers. Here, we focus on MBE, the growth procedure that is often preferred on research because of the ability of *in-situ* diagnostics such as reflection high energy electron diffraction (RHEED) [41].

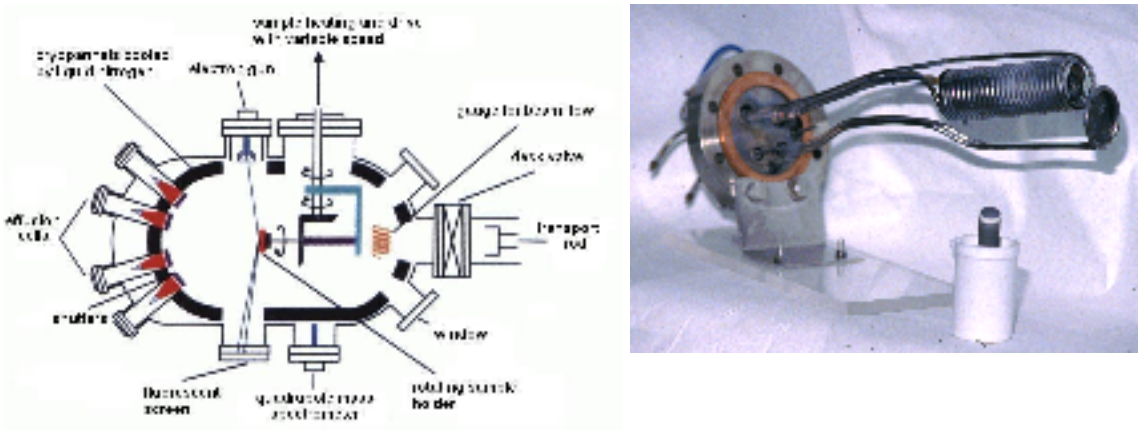

Figure 23 : Schematic picture of an MBE chamber (left) and a silicon Knudsen cell.

A schematic picture of an MBE chamber is given in Figure 23. In a vacuum chamber, several effusion cells (Knudsen cells) are present. Each cell contains a single and pure material such as In, As, Ga, P, Al, Sb, Si or Be. The effusion cell is heated to evaporate molecules from the material that, thanks to the UHV, will form a ballistic molecular beam that will not chemically react before it reaches the heated substrate. A shutter in front of the effusion cell controls the molecular beam and thus selects the desired materials for deposition. The flux from each cell is controlled by the cell temperature, which is used to vary the composition of the deposited alloy or the growth rate, which is typically a few angstrom per second. The walls of the chamber are kept at 77 K so that any atoms that may be lost from the beam and hit the wall are condensed. Substrates can be rotated to improve the homogeneity of the sample.

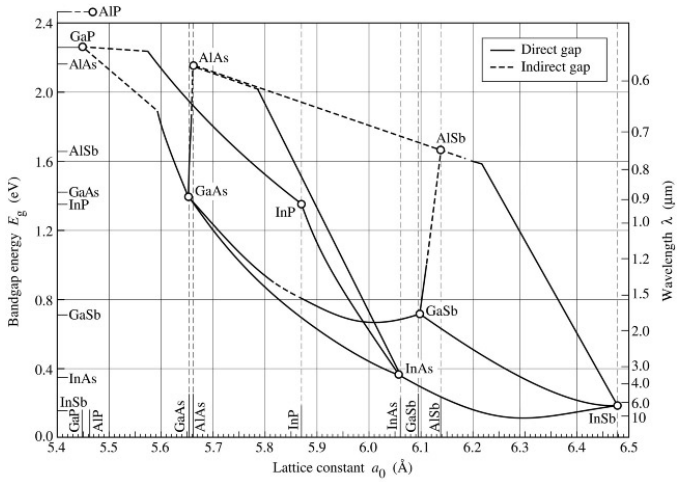

Figure 24 : Lattice constant versus bandgap energy for various III-V semiconductors at room temperature.

By changing the shutters during growth semiconductor heterostructures are obtained with sharp interfaces. The choice of combination of alloys depends on whether a lattice match is required (alloys on the same vertical line on Figure 24, for example. AlAs/GaAs) or on the desired electronic properties [42]. The most useful tool for *in-situ* diagnosis during the growth is the monitoring of the RHEED pattern. Here, a RHEED gun emits high energy electrons (~ 10keV) that are reflected for the sample and hit a phosphor screen. From the RHEED signal information can be gained on the growth process, for instance the diffraction pattern will depend on the surface reconstruction of the sample.

I.6. Patterning techniques.

Two approaches, termed bottom-up and top-down, can be used to study the effect of a reduced dimensionality [43]. Bottom-up techniques include MBE techniques, in particular, self-assembly and self-organization procedures. Self-assembly consists of a random deposition of adatoms all along the substrate surface subsequently followed by a growth on random nucleation sites. On the other hand, self-organization consists of a regular distribution of the adatoms all along the substrate surface. Both self-assembly and self-organization have the advantage of being techniques capable of patterning large areas what make them useful and worthwhile for large scale fabrication.

Contrary to bottom-up techniques, top-down methods consists in reducing the dimensionality from bulk material by lithographic techniques. The term lithography refers to a three step method consisting on an uniform resist coating of the sample or substrate, followed by an exposure and ended with a development of the coating. Lithographic techniques can be classified into three main categories: lift-off, electrodeposition and etching [44]. The first two are post-deposition methods in which the pattern transfer is performed on the substrate subsequently followed by a thin film growth. The etching is performed directly on a previously grown thin film. In all these three cases a pattern must be done on an uniformly deposited –

spinned– resist by performing an exposition on it, commonly to electrons (e-beam lithography), UV light (photolithography) and X-ray (X-ray photolithography). Depending on the exposition method, a mask might be needed. For example, e-beam lithography is a method with no physical mask, performed using a scanning electron microscope (SEM), whereas in photolithography the whole sample is exposed to the radiation of a UV light source and a mask is needed to selectively radiate certain areas of the sample. During the exposition, the chemical properties of the resist are locally changed. This allows to selectively remove either the exposed or the non-exposed parts submerging the sample into a chemical agent known as developer. This step in which the pattern is transferred to the resist is known as development. It is noteworthy that the resolution limit of the lithographic techniques is eventually determined by the radiation wavelength. While the e-beam lithography might reach a resolution of 10 nm, conventional photolithography resolution limit is around one micrometer.

The etching technique consist of the removal of material from a thin film using either chemical or physical processes. Thus, after growing a thin film on a substrate and uniformly coating it with resist, the pattern is transferred to the resist by exposition plus development. The next step of removing the material not covered by the resist can be done either chemically (known as wet etching), physically by ion bombardment (known as dry etching) or by a combination of both (reactive ion etching). Wet etching is an isotropic method that causes tilted patterns. On the contrary, dry etching yields sharp profiles and therefore is more used for ultrafine structures. After performing the etching, the residual resist must be removed either stripping it with an oxygen plasma or by chemical means.

As shown in Figure 25, either positive or negative resist can be used in the etching technique. If positive resist is used, the resist removed during development is the exposed one (Figure 25.a)). In contrast, when using negative resist, the non-exposed part is removed during development (Figure 25.b)). A complete description of the etching technique and a list of etching recipes for some common materials can be found in [45]. In both the lift-off technique (Figure 25.c)) and the electrodeposition (Figure 25.d)), the thin film is grown after performing the development of the resist. Thus, the first step of both processes is the spin coating of the substrate, followed by an exposition of the pattern in either positive or negative resist and by a subsequent development. The main difference between lift-off and electrodeposition is the way the material is grown on the patterned substrate. In the case of the lift-off, the material is sputtered or evaporated in low pressure chambers, whereas in electrodeposition the material is deposited by current circulation through an electrolyte. Lift-off method is more suited to fabricate planar patterns since both the resist coated and non-coated areas are covered by the grown material. Therefore, in order to properly remove the remanent resist after the pattern transfer, it is mandatory a large ratio resist vs. grown material. Both lift-off and etching have been used to fabricate the micro-mechanical systems presented in this thesis. In each case either e-beam lithography or optical lithography has been used.

E-beam lithography is performed using a Scanning Electron Microscope (SEM) and a electron-sensitive resist (Polymethylmethacrilate, PMMA). Elements of some tens of nanometers diameter and very different shapes may be obtained using this technique. In addition, this method is quite slow and very expensive compared to optical techniques. UV optical lithography might pattern very large areas using a mask but its resolution limit only allow elements size in the range of the microns.

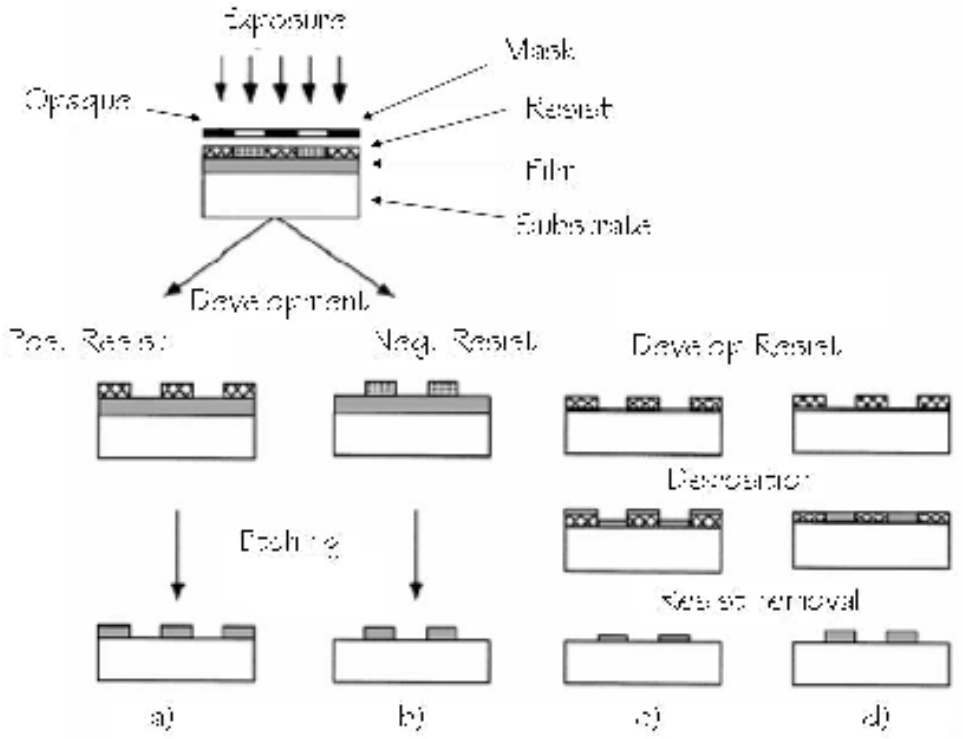

Figure 25 : Schematic picture of lithographic processes. a) positive resist and etching, b) negative resist and etching, c) lift-off and d) electrodeposition.

References.

[1] S. I. Shah, *"Sputtering: Introduction and general discussion",* Ed. D. A. Glocker and S. I. Shah, *"Handbook of Thin Film Process Technology"*, IOP Publishing (1995).

[2] T. C. Tisone and J. B. Bindell*, "Low Voltage triode sputtering with a confined plasma",* J. Vac. Sci. Technol., **11**, 519 (1974).

[3] M. Volmer and A Weber, *"Nuclei formation in supersaturated states"*, Z. Phys. Chem., **119**, 277 (1926).

[4] F. C. Frank and H. J. van der Merwe, *"One-dimensional dislocations. Static theory",* Proc. Roy. Soc. London. Ser. A, **198**, 205 (1949).

[5] Ivan N. Stranski and L. Von Krastanow, Abhandlungen der Mathematisch-Naturwissenschaftlichen Klasse. Akademie der Wissenschaften und der Literatur in Mainz, **146**, 797 (1939).

[6] J. M. Albella, *'Láminas delgadas y recubrimientos: Preparación, propiedades y aplicaciones'* Colección Biblioteca de Ciencias, Editorial CSIC (2003).

[7] B. A. Movchan and A. V. Demchishin, *"Investigations of the structure and properties of thick Ni, Ti, W, Al2O3, and ZrO2 vacuum deposited films",* Phys. Met. Metallogr., **28,** 83 (1969).

[8] J. A. Thornton, *"Influence of substrate temperature and deposition rate on structure of thick sputtered Cu coatings"*, J. Vac Sci. Technol., **12,** 830 (1975).

[9] R. Koch, *"The intrinsic stress of polycrystalline and epitaxial thin metal films"* J. Phys.: Condens. Mater., **6**, 9519 (1994).

[10] A. K. Sinha, H. J. Levinstein and T. E. Smith, *"Thermal stresses and cracking resistance of dielectric films (SiN, Si_3N_4, and SiO_2) on Si substrates"*, J. Appl. Phys., **49**, 2423 (1978). H. K. Pulker, *"The origin of mechanical stress in vacuum-deposited MgF2 and ZnS film"*, Thin Solid Films, **59**, 65 (1979).

[11] G. G. Stoney, *"The tension of metallic films deposited by electrolysis"*, Proc. R. Soc. London A, **32**, 172 (1909).

[12] F. J. von Preissig, *"Applicability of the classical curvature-stress relation for thin films on plate substrates"* ,J. Appl. Phys., **66**, 4262 (1989). G. Moulard, G. Contoux, G. Gardet, G. Motyl and M. Courbon*, "Improvement of the cantilever beam technique for stress measurement during the physical vapor deposition process",* J. Vac. Sci. Technol. A, **16**, 736 (1998).

[13] L. B. Freund, J. A. Floro and E. Chason, *"Extensions of the Stoney's formula for substrate curvature to configurations with thin substrates or large deformations"*, Appl. Phys. Lett., **74,** 1987 (1999).

[14] R. W. Hoffman*, 'Physics of thin films'*, ed G. Hass and R. E. Thun (New York: Academy) **3**, 211 (1966).

[15] R. Koch and R. Abermann, *"Microstructural changes in vapour-deposited silver, copper and gold films investigated by internal stress measurements",* Thin Solid Films, **140**, 217 (1986).

[16] R. Koch, D. Winau, A. Führmann and K. H. Rieder, *"Growth-mode-specific intrinsic stress of thin silver films",* Phys. Rev. B, **44**, 3369 (1991).

[17] C. W. Mays, J. S. Vermaak and D. Kuhlmann-Wilsdorf, *"On surface stress and surface tension II : Determination of surface stress of gold"* Surf. Sci. **12**, 134 (1968).

[18] R. Abermann, R. Koch and R. Kramer, *"Electron microscope structure and internal stress in thin silver and gold films deposited onto MgF2 and SiO substrates" ,* Thin Solid Films **58**, 365 (1982).

[19] R. Abermann*, "Internal stress of vapour-deposited aluminium films: Effect of O2 and water vapour present during film deposition",* Thin Solid Films, **186**, 233 (1990).

[20] J. A. Thornton and D. W. Hoffman*, "Stress-related effects in thin films",* Thin Solid Films, **171**, 5 (1989).

[21] A. Mazuelas, A.Ruiz, F. Ponce and F. Briones, *"Structural characterization of GaP/GaAs superlattices"*, J. Phys. D: Appl. Phys., **26**, A167 (1993).

[22] P. P. Buaud, F.M. d'Heurle, E.A. Irene, B.K. Patnaik and N.R. Parikh, *"Stress-related effects in thin films"* , J. Vac. Sci. Technol. B, **9**, 2536 (1991).

[23] R. Abermann*, "Internal stress of vapour-deposited aluminium on aluminium substrate films: Effect of O2 and water incorporated in the substrate,* Thin Solid Films, **188**, 385 (1990).

[24] M. Murakami, *"Deformation in thin films by thermal strain"*, J. Vac. Sci. Technol. A, **9**, 2469 (1991).

[25] R. C. Cammarata*, "Surface and Interface Stress Effects in Thin Films"*, Prog. Surf. Sci., **46**, 1 (1994).

[26] D. W. Hoffman and J. A. Thornton*, "Internal stresses in sputtered chromium"* Thin Solid Films, **40**, 355 (1976).

[27] W. D. Westwood, *"Calculation of deposition rates in diode sputtering systems"*, J. Vac. Sci. Technol., **15**, 1 (1978).

[28] K. Meyer, Ivan K. Schuller and Charles M. Falco, *"Thermalization of sputtered atoms"*, J. Appl. Phys., **52**, 5803 (1981).

[29] D. W. Hoffman and M. R. Gaerttner, *"Modification of Evaporated Chromium by Concurrent Ion Bombardment "*, J. Vac. Sci. Technol., **17**, 425 (1980).

[30] Y. G. Shen, *"Effect of deposition conditions on mechanical stresses and microstructure of sputter-deposited molybdenum and reactively sputter-deposited molybdenum nitride",* Materials Science and Engineering A, **359**, 158 (2003).

[31] M. Faraday, *'Experimental researches in electricity. Nineteenth series'*, Phil. Trans. Soc., **136**, 1 (1846).

[32] J. Kerr, *'On rotation of the plane of polarization by reflection from the pole of a magnet'* Phil. Mag., **3**, 332 (1877).

[33] G. Armelles, J. L. Costa-Krämer, J. I. Martin, J. V. Anguita, J. L. Vicent, *'Anisotropy measurements in mesoscopic magnets by magneto-optical torque'*, Appl. Phys. Lett., **77**, 2039 (2000)

[34] Etienne du Trémolet de Lacheisserie, *'Magnetostrcition : Theory and Aplications of Magnetoelasticity '* CRC Press, 47 (1993).

[35] A. E. Clark, '*Magnetostrictive rare earth-Fe2 compounds'*, in '*Ferromagnetic Materials'*, Vol.1, Wohlfarth, E. P., Ed., North-Holland, (1980).

[36] R. C. O'Handley, *'Magnetostriction on transition-metal-metalloid glasses: Temperature dependence*', Phys. Rev. B., **18**, 930 (1978).

[37] R. Gontarz, H. Ratajczak and, P. Šuda, *'Magnetostriction of Thin Ni-Films',* Phys. Stat. Sol., **6**, 909 (1964). E. Klokholm, *'The measurement of magnetostriction in ferromagnetic thin films',* IEEE Trans. Magn., **MAG-12**, 819 (1976).

[38] H. U. Kunzi, '*Glassy metals II*'. Ed. H. Beck and H. J. Guntherodt, Springer-Verlag (1983).

[39] E. Luborsky, '*Amorphous Metallic Alloys'*. Butterworths 203 (1984).

[40] Menzel-Glasser coverslips.

[41] Robin F. C. Farrow, *'Molecular beam epitaxy. Applications to key materials'*. Noyes publications, New Jersey, (1995).

[42] Y. Yu, Manuel Cardona, *'Fundamentals of Semiconductors'*. Springer, Peter, (2005).

[43] Marc J. Madou, '*Fundamentals of Microfabrication : The Science of Miniaturization*'. CRC Press (2002).

[44] J. I. Martin, J. Nogués, K. Liu, J. L. Vincent, I. K. Schuller, *'Ordered magnetic nanostructures',* J. Magn. Magn. Mat., **256**, 449 (2003) and references therein.

[45] J. L. Vossen, W. Kern (Eds.), *'Thin film processes'*, Academic Press, New York (1978)

II

Accumulated stress in amorphous $Fe_{80}B_{20}$ thin films during sputtering deposition.

II.1. Introduction. 41

II.2. Experimental details. 41

II.3. *In-situ* stress measurements during $Fe_{80}B_{20}$ thin film deposition. 41

II.3.1. Regime I : initial instantaneous compression. 42

II.3.2. Regime II : interaction between amorphous islands and substrate. 44

II.3.3. Regime III : 'Atomic peening effect' due to ion/atom bombardment. 45

II.4. Total accumulated stress as a function of the deposition parameters. 46

II.5. Monte-Carlo simulation: kinetic energy of arriving atoms. 47

II.6. X-ray diffraction measurements of the $Fe_{80}B_{20}$ thin films. 50

II.7. Atomic Force Microscopy (AFM) measurements of the $Fe_{80}B_{20}$ thin films. 51

II.7. Conclusions. 52

References. 52

II.1. Introduction.

It is well know that when a thin film is deposited onto a micro-electro-mechanical system (MEMS), as for example a micro-cantilever, the imbalanced residual stress in the two layers usually deflects the micro-cantilever upwards or downwards, decreasing the functionality and reliability of the micro-cantilever. The reduction of the accumulated stress in deposited thin films is a major research effort for the development of micro-electro-mechanical devices, as for example, membranes, micro-cantilever based infrared detectors, etc… [1]. In this thesis, amorphous magnetostrictive $Fe_{80}B_{20}$ thin films are proposed to be used as actuators for Atomic Force Microscopy (AFM) micro-cantilever. In this chapter, the main objective is to optimize the deposition parameters to achieve near-zero stress $Fe_{80}B_{20}$ thin films, avoiding cantilever curvatures due to the imbalanced residual stress in the two layers. The substrate curvature induced by the deposited film is measured *in-situ* during film growth and quantitatively related to the film accumulated stress. Firstly, the growth mechanism of the amorphous thin films is discerned: an initial island formation and coalescence followed by a continuous thin film growth. Then, for the continuous films, the total accumulated stress is measured, for a wide range of sputtering pressures and target potentials, to achieve near zero stress amorphous $Fe_{80}B_{20}$ thin films to be used in micro-mechanical actuators.

II.2. Experimental details.

Amorphous $Fe_{80}B_{20}$ films were deposited on glass cantilevers/substrates in the triode sputtering system described in Chapter I, Section I.2.4., from a commercial target of nominal composition $Fe_{80}B_{20}$. The deposition was carried out either varying the Ar working pressure in the range $(2 – 25) \cdot 10^{-3}$ mbar (for a fixed target potential of -2.0 kV) or varying the target potential between -0.5 and -2.0 kV (for a fixed Ar working pressure of $8 \cdot 10^{-3}$ mbar). The target to substrate distance was 8 cm and the base pressure was in the low 10^{-9} mbar range. The angle of deposition was chosen at 45º with respect to normal incidence. The deposition time for all the films was 300 seconds, producing thicknesses that varied from 30 to 70 nm, as measured with AFM and profilometer techniques.

II.3. *In-situ* stress measurements during $Fe_{80}B_{20}$ thin film deposition.

The evolution of the accumulated stress for $Fe_{80}B_{20}$ films during the early stages of deposition as a function of the film thickness is shown in Figure 1. In this case, different Ar gas pressures were used, whereas the target potential was kept constant to -2.0 kV. Three regimes are clearly distinguished in Figure 1: I, II and III. They are discussed in detailed in what follows.

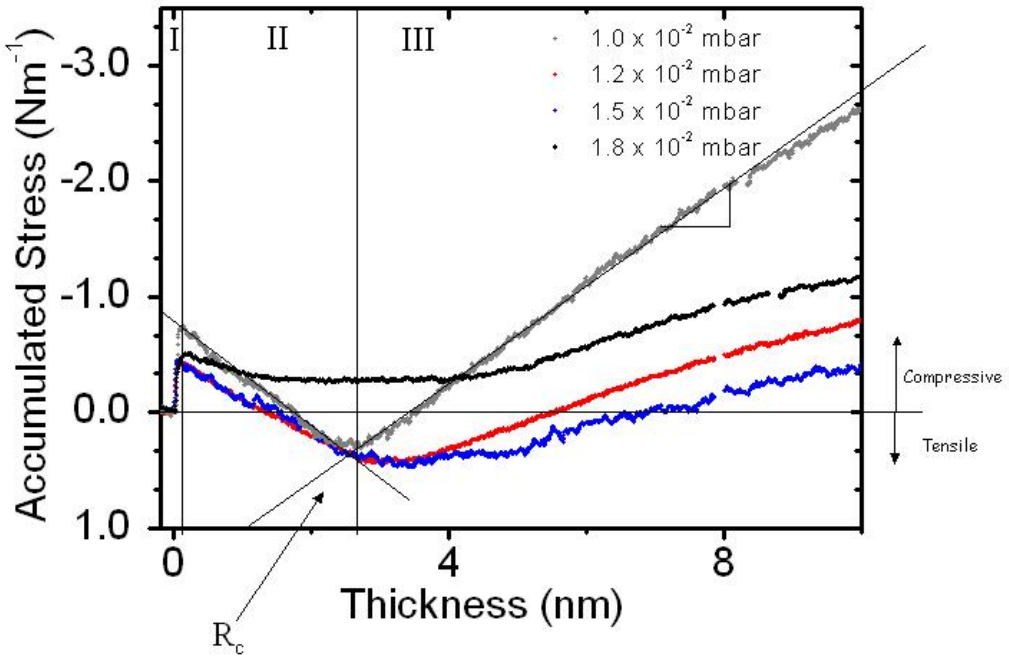

Figure 1 : Accumulated stress evolution as a function of the film thickness for four different pressures and a fixed target potential of –2kV during the early stages of deposition. Three stress regimes are clearly distinguished. Regime I: initial instantaneous compression: thermal induced curvature. Regime II: Pre-coalescence tensile regime related with the interaction between the discontinuous film and substrate. Regime III: compressive stress due to 'ion peening' or bombardment.

II.3.1. Regime I : initial instantaneous compression.

This regime is a nearly instantaneous rise of a compressive stress when the target potential is switched on (Figure 2.a)). This effect is reversible, disappearing when the target potential is switched off. This is shown in Figure 2.b), where the stress evolution is plotted as a function of the deposition time. At 300 seconds, which is the deposition time for all the samples, an abrupt apparent tensile relaxation is observed when the target potential is switched off, which magnitude is of the order of the initial compressive stress (regime I). A similar effect, that develops during Volmer-Weber growth of polycrystalline low melting point films [2], has been associated with adatom-surface interactions. However, in the case of amorphous metallic films, surface diffusion is strongly limited, and no large adatom population is expected. Therefore, in our case this effect should rather originate on an effective surface heating due to thermalization of the impinging atoms kinetic energy and chemical bonds formation. The difference between the effective surface temperature and the bulk gives rise to a substrate bending equivalent to a surface stress of compressive character. The amplitude of this effect is proportional to the instantaneous deposited power and depends on the thermal dilatation coefficient and heat capacity of the substrate. With respect to the sputtering parameters, it depends indeed strongly on the target potential, as shown in Figure 2.c). This effect does not contribute to the total

accumulated stress, but can stimulate the generation the nucleation sites and increase the substrate surface temperature (and consequently the adatom mobility).

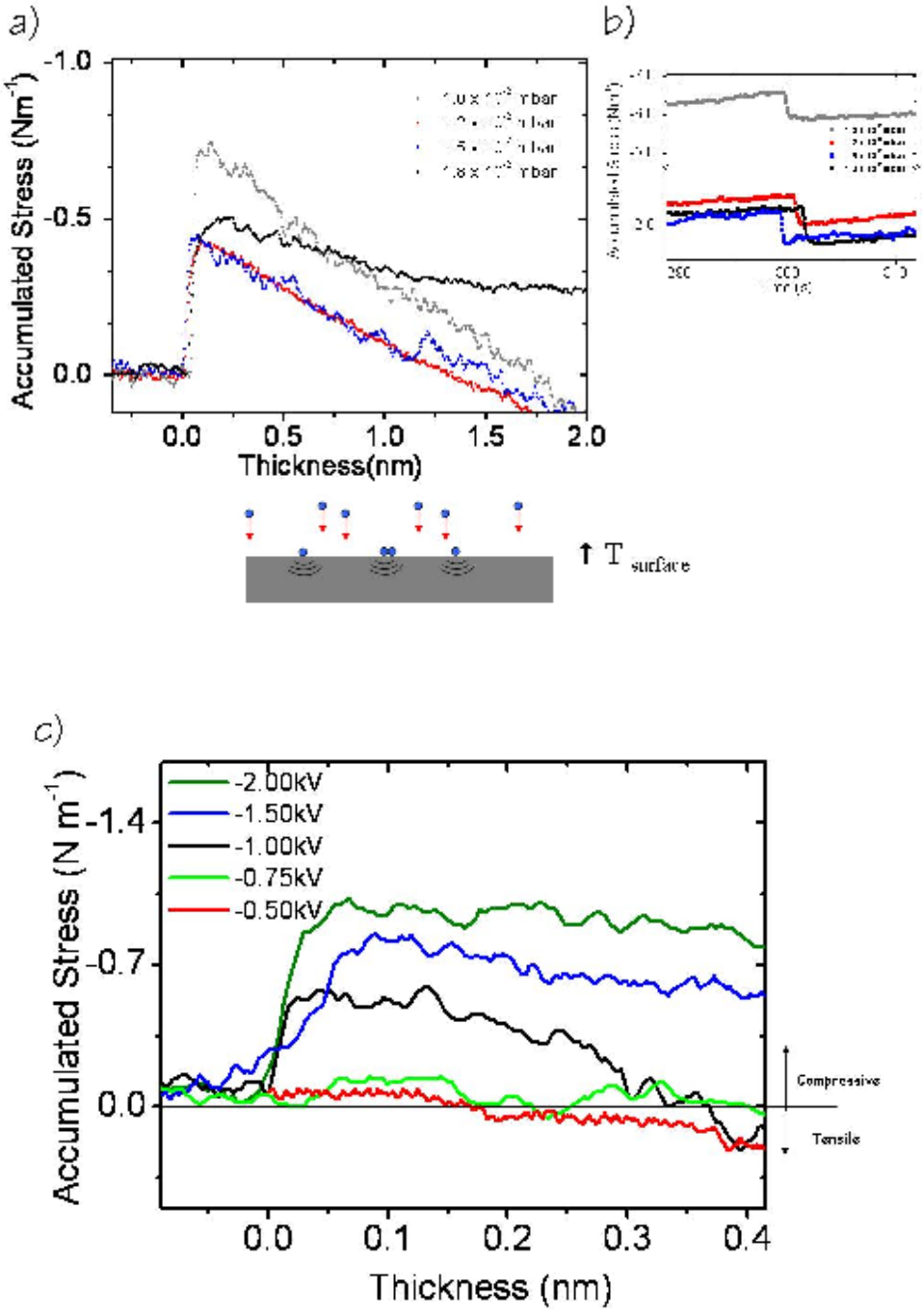

Figure 2 : a) Accumulated stress evolution as a function of the film thickness for four different pressures and a fixed target potential of –2.0 kV during the early stages of deposition. b) Accumulated stress evolution as a function of the deposition time for four different pressures and a fixed target potential of –2.0 kV during the last stages of deposition. It is shown that the compressive stress appearing in Regime I is reversible when the target potential is switched off. Schematic picture of the arriving atoms (in blue) heating the substrate surface (gray) giving rise to a surface heating. c) Accumulated stress evolution as a function of the film thickness for five different target potentials and a fixed Ar working pressure of 8 • 10^{-3} mbar, during the Regime I. It is shown that the amplitude of this regime depends strongly on the target potential and consequently on the deposited power.

II.3.2. Regime II : interaction between amorphous islands and substrate.

Therefore, the accumulated stress during the initial few nanometers growth (Regime II) is clearly tensile, corresponding to the interface stress increase that accompanies the nucleation of very small islands interacting with the glass substrate surface. The interface stress between glass substrate and those islands seems to be the dominant source of the large component of tensile stress measured. The mean size and aspect ratio (interface to volume) of the islands depends also on the surface temperature, surface migration of adatoms and density of nucleation sites, making the quantitative description of this regime a very complicated issue. Confirming the above arguments, it has also been found experimentally that the stress sign and magnitude in Regime II depends strongly on the type of substrate, as shown in Figure 3, where two different substrates were used: mica and glass. In the case of mica, opposite sign for Regime II was found, probably due to the completely different surface chemistry as compared with that of glass.

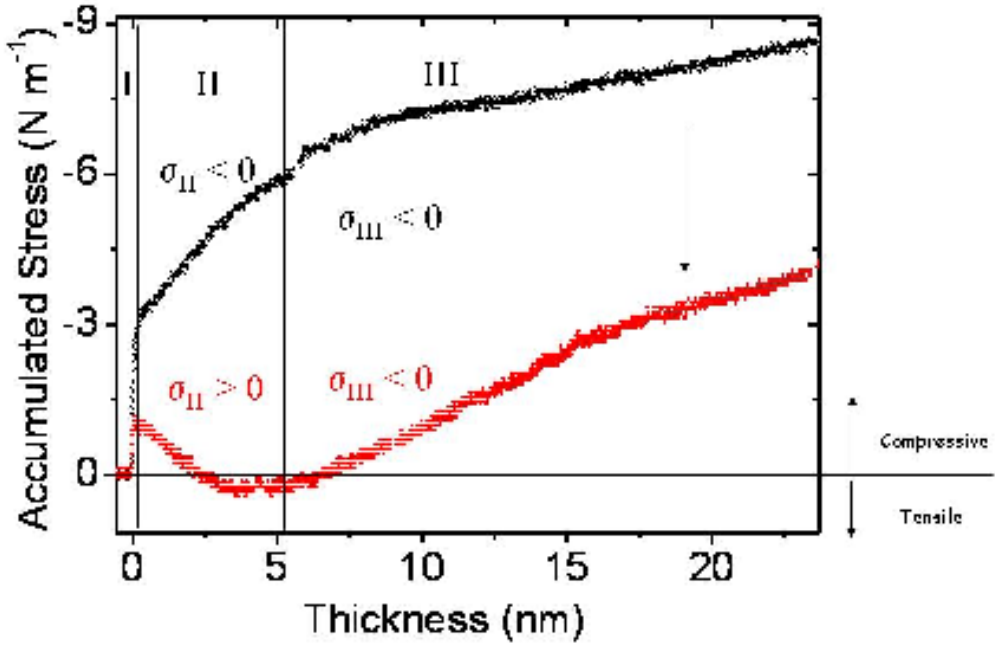

Figure 3 : Accumulated stress evolution as a function of the film thickness for two different substrates: mica (black line) and glass (red line), and for the same deposition conditions: -2.0 kV target potential and 8 • 10^{-3} mbar working gas pressure . It is shown a change in the sign of Regime II. Once the thin films are continuous (Regime III), the same stress behavior is observed.

The measured tensile stress is found to be lower for higher Ar working pressures, as shown in Figure 1, i.e., for lower energy of the arriving atoms and correspondingly a lower surface diffusion. This tensile stress reaches a saturation value at about 18 • 10^{-3} mbar. Taking into account that amorphous films usually exhibit a columnar structure due to self shadowing effects, a lower density of $Fe_{80}B_{20}$ films grown at higher Ar pressure is expected [3], with a higher density of voids, defects, etc…

A critical thickness can be defined at the point between this initial tensile (II) and the compressive regime (III) which follows (R_C in Figure 1). At this thickness, corresponding to the minimum of the accumulated stress vs thickness curve, film becomes continuous and coalescence or building of a columnar structure takes over [4]. This was also corroborated with measurements of the electrical resistance. For amorphous $Fe_{80}B_{20}$ thin films sputtered on glass substrates, the value of the critical thickness was studied as a function of the working gas pressure. The critical thickness increases for higher Ar working pressures, as shown in Figure 4.

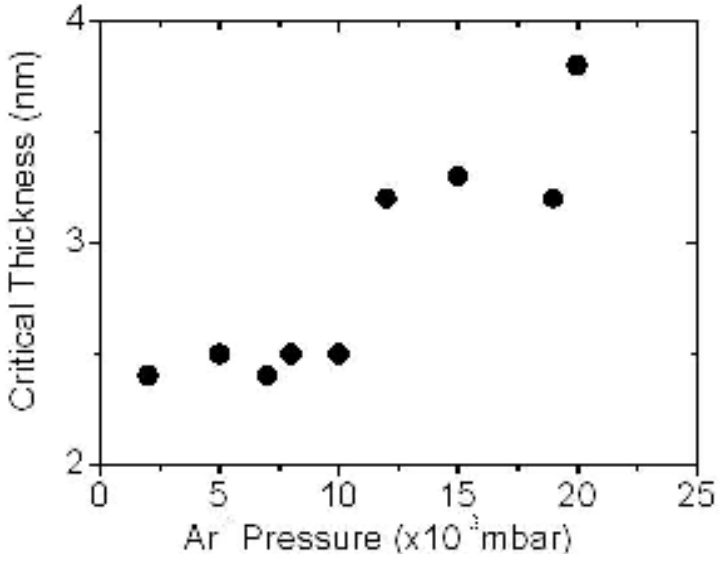

Figure 4 : Dependence of the critical thickness (R_C) on the deposition pressure. The dots are the measurements of the minimum of the total accumulated stress curve, i.e., the points at which the accumulated stress in Regime II changes sign.

II.3.3. Regime III : 'Atomic peening effect' due to ion/atom bombardment.

The origin of the compressive stress in Regime III is the 'atomic peeing effect', due to either the deposited atoms or reflected neutral atoms bombarding the continuous film [5]. As explained in Chapter I, Section I.3.4., this effect accumulates linearly with the film thickness and is strictly dependent on the kinetic energy of the impinging atoms on the growing film. This arriving energy depends on the target potential and the thermalization capacity of the sputtering gas filling the space between the target and the substrate. This effect can be seen in Figure 5, where the accumulated stress evolution during the Regime III is shown as a function of the film thickness for different working gas pressures and a fixed target potential of –2.0 kV. In the 10^{-3} mbar pressure regime, the compressive stress is higher for lower working pressures, i.e., for higher kinetic energy of the arriving atoms.

This effect should disappear when the atoms arrive to the substrate attenuated. Thus, several strategies can be used to avoid this distortion produced by the energetic atoms. Either an increase in the working gas pressure or a decrease in the target potential can be used.

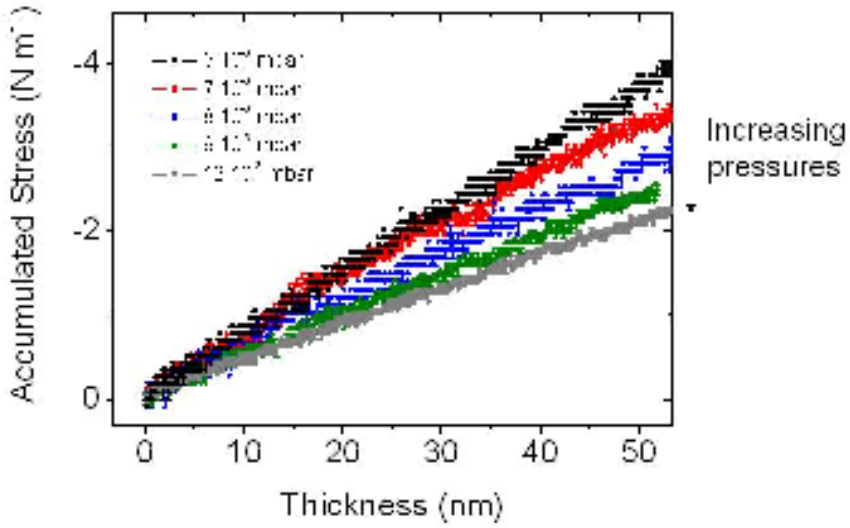

Figure 5 : Linear part of the accumulated stress evolution in Regime III as a function of the film thickness for different Ar working pressures and for a fixed target potential of –2kV. The 'atomic peening effect' is lower for higher Ar working pressures.

For amorphous sputtered $Fe_{80}B_{20}$ thin films, two main competitive stress contributions of opposite sign are present. For higher energy of the arriving atoms, the film is under a strong compressive accumulated stress due to the 'atomic peening effect', while if the energy is lowered, the columnar structure and the high density of grain boundaries gives rise to a strong tensile accumulated stress [Chapter I, Section I.3.3]. The competition of these two phenomena allows us to have, for a set of deposition conditions, thin films in which the accumulated stress is compensated (not relaxed).

II.4. Total accumulated stress as a function of the deposition parameters.

The total accumulated stress was studied as a function of the deposition parameters either by changing the Ar working pressure or the target potential independently.

In the first case, the target potential was kept constant to –2.0 kV while the working gas pressure was varied between (2 – 25) • 10^{-3} mbar. For these deposition parameters, the total accumulated stress in the films after five minutes deposition time is shown in Figure 6. This accumulated stress decreases as the working pressure increases, until a value of 15 • 10^{-3} mbar, where the total stress remains constant to a value of –1 GPa. Then, the total stress is compressive for all the range due to the ion peening effect. Under these conditions, the residual stress cannot be compensated varying only the pressure at a fixed target potential of –2.0 kV. As it will be explained in the last section, this compressive stress is due to the strong energy of the back-reflected atoms.

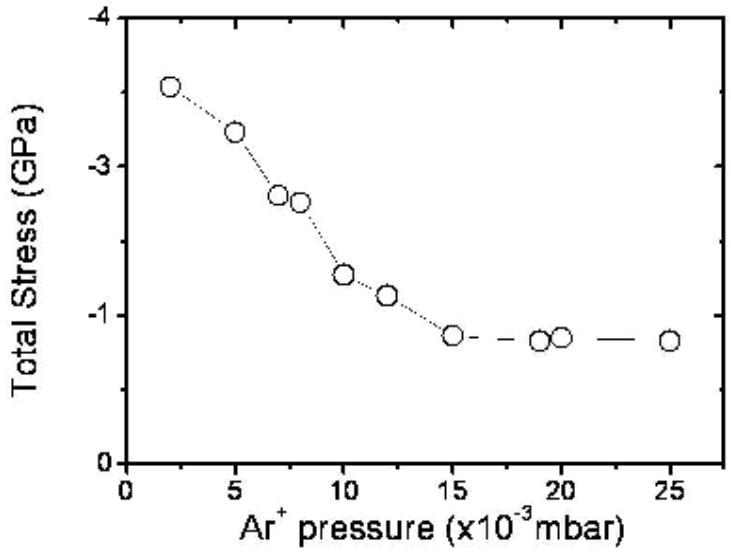

Figure 6 : Total accumulated stress as a function of the working pressure for a fixed target potential of –2.0 kV. The accumulated stress is compressive for all the range due to the ion peening effect.

In the second case, the working gas pressure was kept constant to $8 \cdot 10^{-3}$ mbar while the target potential was varied between – 0.5 kV and – 2.0 kV. The total accumulated stress in the films after five minutes deposition time is shown in Figure 7. It can be seen that the stress was compensated at around – 0.7 kV target potentials, obtaining near zero accumulated stress amorphous $Fe_{20}B_{20}$ films.

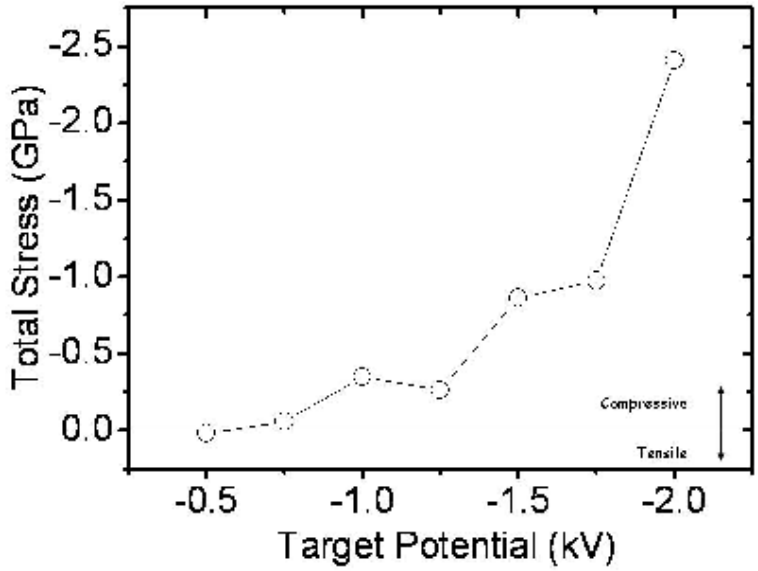

Figure 7 : Total accumulated stress as a function of the target potential for a fixed working pressure of $8 \cdot 10^{-3}$ mbar. This accumulated stress is compensated at –0.7 kV target potential .

II.5. Monte-Carlo simulation: kinetic energy of arriving atoms.

As shown in the previous section, the accumulated stress in amorphous sputtered thin films, depends strongly on the kinetic energy of the arriving atoms. Thus, an estimation of those energies was performed to compare with the experimental results obtained by stress measurement. Monte Carlo simulations of the sputtering process describe quantitatively the experimental results. The energy distributions of sputtered Fe, B and Ar atoms ejected from the target were calculated together with the residual energy distribution as a function of distance traveled through the Ar sputtering gas, for different working pressures as in earlier publications [6]. From these results, we can extract the distance at which the energy of the atoms are reduced to the thermal energy (k_BT) of the gas. This distance is called thermalization distance, and increases with the mass and energy of the atoms and with decreasing working gas pressure.

The first calculation is the kinetic energy spectrum of the sputtered and back-reflected atoms. For a target potential of -2.0 kV, the spectrum of the sputtered atoms has a strong peak at energies of a few eV and a long tail up to energies close to the incident ion energy. However, for back-reflected ions, the spectrum of energies has a strong peak for energies in the range of a few hundred of eV, as it is shown in Figure 8.

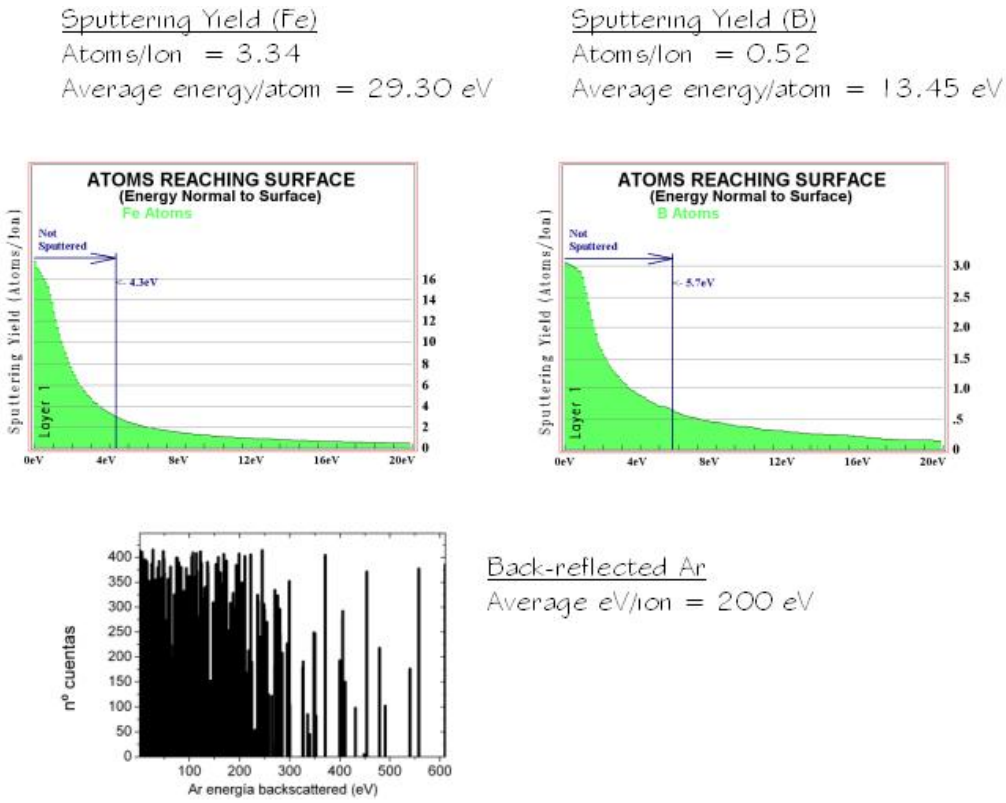

Figure 8 : Initial energy distribution for sputtered Fe and B and for back-reflected Ar at the surface of the targets. Argon gas accelerating voltage was –2.0 kV. The spectrum of the sputtered atoms has a strong peak at energies of a few eV and a long tail up to energies close to the incident ion energy. A value of average energy per atom is estimated.

To estimate the thermalization distance, a Monte-Carlo simulation that uses the kinetic gas theory was performed. This distance is the product of the mean free path of an atom (that

depends on the pressure of the sputtering gas, the atom diameters and the mass of the atoms) traveling through a gas and the number of collisions between the atom and the gas atoms until it reduces its energy to the thermal energy of the gas (k_BT). In Figure 9 it is shown the energy loss of the sputtered atoms due to collisions with the sputtering gas as a function of the traveled distance for our working conditions (initial energy of Ar+ = 2 keV, target-substrate distance = 8cm and a working gas pressure of $15 \cdot 10^{-3}$ mbar).

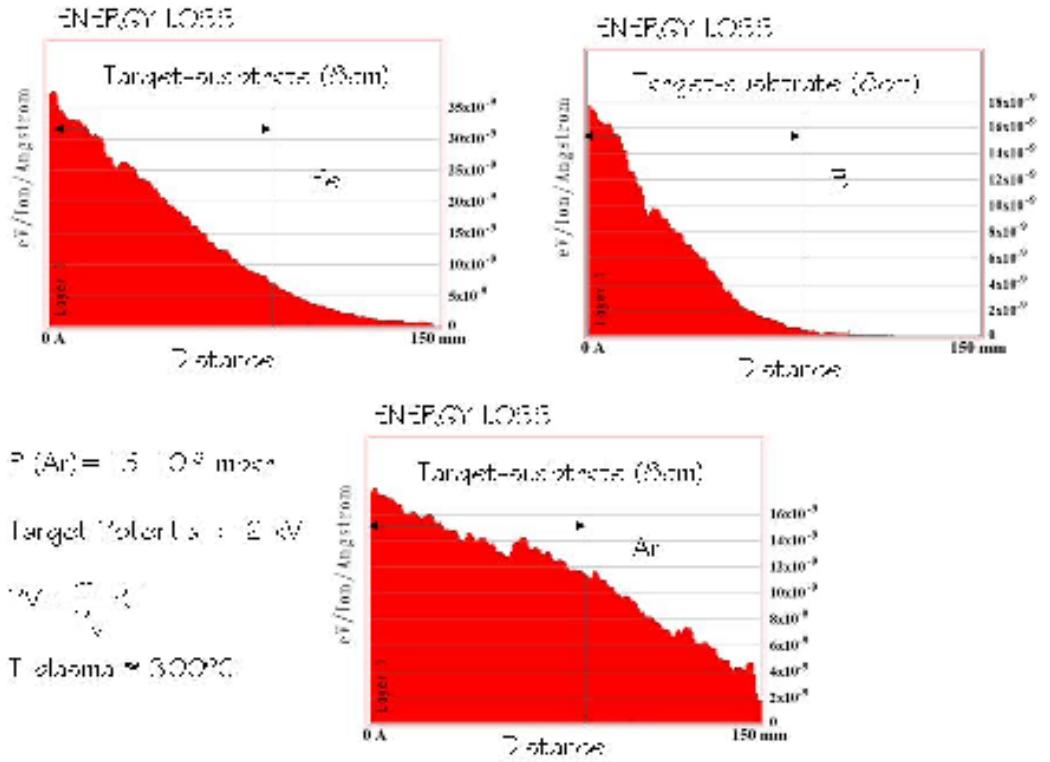

Figure 9 : Average Fe, B and Ar energies as a function of the distance traveled. Ar gas pressure was 15 • 10^{-3} mbar and the plasma temperature was estimated to 300ºC.

It is shown that iron and boron atoms reach the substrate almost thermalized at $15 \cdot 10^{-3}$ mbar, while Ar atoms do not arrive thermalized at the substrate in our pressure range ($2 – 25 \cdot 10^{-3}$ mbar). The calculated thermalization distance of the Ar+ ions for a working pressure of $15 \cdot 10^{-3}$ mbar was 15 cm. This is consistent with the stress measurements, in which the 'atomic peening effect' (linear part Regime III) still appears in the 10^{-2} mbar pressure regime. This means, that with a target potential of –2.0 kV, even when the iron and boron atoms are probably thermalized (above $1.5 \cdot 10^{-2}$ mbar), the ion peening effect still appears, due to reflected Ar. Although these Ar energetic particles arrive at the substrate attenuated by gas scattering they are not still at thermal equilibrium with the substrate, giving rise to a surface bombardment of the film. For that reason, the value of the target potential must be lowered.

As shown in Figure 7, for lower values of target potential, the effect of the atomic peening is strongly reduced and the stress changes from compressive to tensile as expected for low

mobility sputtered films that exhibit a columnar growth, such a Cr, W or amorphous films. [Ref Koch]. A Monte Carlo simulation was performed for the optimal working conditions (initial energy of Ar+ = 0.7 keV, target-substrate distance = 8 cm and a working gas pressure of $8 \cdot 10^{-3}$ mbar). In Figure 10 it is shown the energy loss of the sputtered atoms due to collisions with the sputtering gas as a function of the traveled distance for our working conditions. Firstly, it is shown that iron and boron atoms clearly reach the substrate thermalized. Secondly, Ar back-reflected atoms reduce the film surface bombardment, but are not still thermalized. This demonstrates that a low Ar bombardment is necessary to achieve $Fe_{20}B_{20}$ films with near zero accumulated stress, compensating the tensile stress due to the columnar growth that appears in low energy deposited atoms.

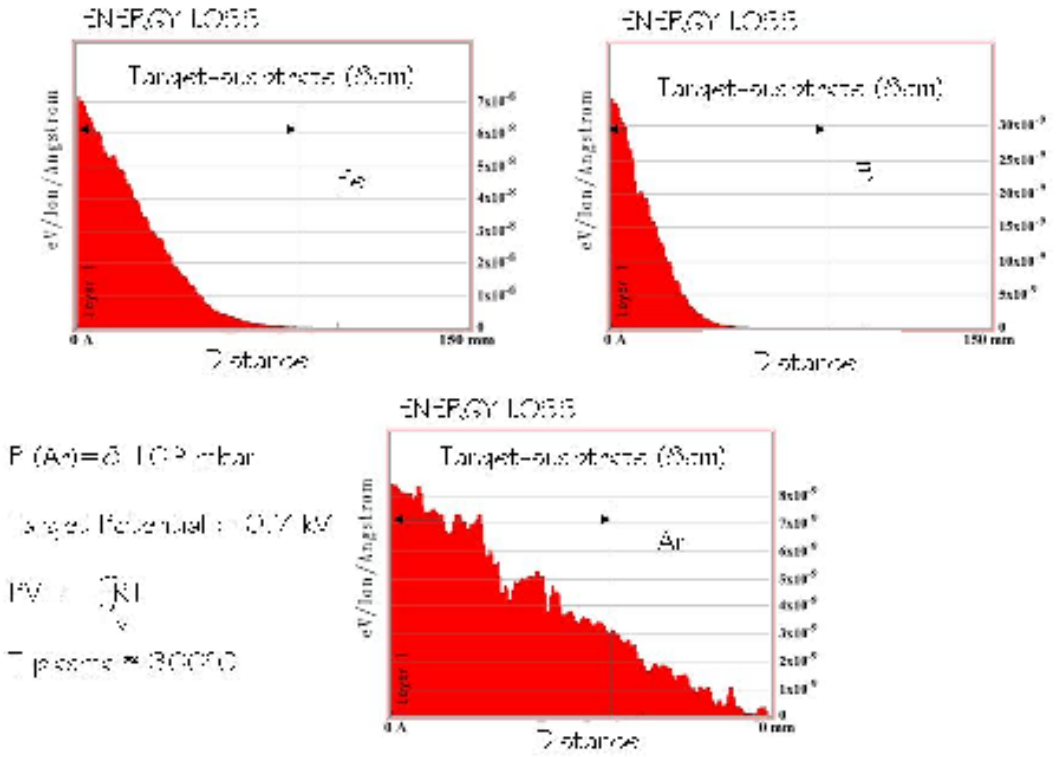

Figure 10 : Average Fe, B and Ar energies as a function of the distance traveled. Ar gas pressure was $8 \cdot 10^{-3}$ mbar and the plasma temperature was estimated to 300ºC.

II.6. X-ray diffraction measurements of the $Fe_{80}B_{20}$ thin films.

X-ray diffraction analysis were performed on a range of the $Fe_{80}B_{20}$ films deposited to study its accumulated stress. As no sharp diffraction peak was observed for thin films whatever the sputtering working conditions, all the deposited films can be termed amorphous, as shown in Figure 11.a). However, for longer deposition times (15min) and high target potential (-2.0 kV) the films crystallize and a diffraction peak at 2θ = 44.42º appears in the diffactogram, as shown

in Figure 11.b). This peak is closed to the (112) of the Fe_3B tetragonal alloy. This observation is in good agreement with the results of previous experiments, which show the crystallization of the amorphous $Fe_{80}B_{20}$ films by annealing [7]. The hysteresis loops of crystallized Fe-B films show a higher value of the coercitivity (~ 60 Oe) combined with a tetragonal anisotropy. In this case, crystallization is due to an increase of the temperature of the sample for long deposition times, probably due to the high energetic bombardment of the film during deposition. Keeping the target potential below -1.0 kV results in amorphous films for at least 1 hour deposition time.

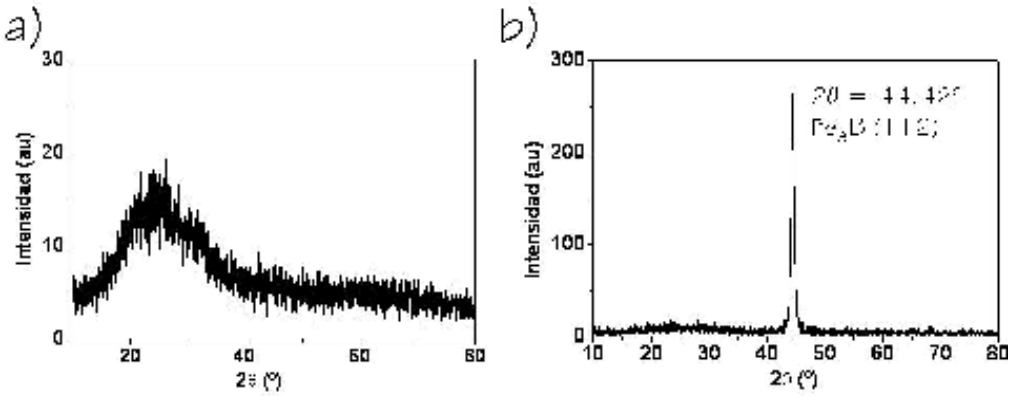

Figure 11 : a) X-ray diffractogram of a $Fe_{80}B_{20}$ thin film deposited at -2kV target potential, 8 • 10^{-3} mbar working gas pressure and 5 minutes deposition time. No sharp peak is observed. b) X-ray diffractogram of a $Fe_{80}B_{20}$ thin film deposited at -2.0 kV target potential, 8 • 10^{-3} mbar working gas pressure and 15 minutes deposition time. It is observed a sharp peak at 2θ = 44.42º, which is very closed to the (112) of the Fe3B tetragonal alloy.

II.7. Atomic Force Microscopy (AFM) measurements of the $Fe_{80}B_{20}$ thin films.

Atomic Force Microscopy (AFM) studies were performed on a range of the $Fe_{80}B_{20}$ films deposited to study its accumulated stress. No differences in the surface roughness were found, even when $Fe_{80}B_{20}$ films deposited with high energy of the arriving atoms (for example: -2.0 kV target potential and 5 • 10^{-3} mbar working gas pressure) were compared with films deposited with low energy of the arriving atoms (for example: -0.7 kV target potential and 8 • 10^{-3} mbar working gas pressure). As shown in Figure 12, $Fe_{80}B_{20}$ films exhibit very flat surfaces, with 0.3 – 0.5 nm of roughness.

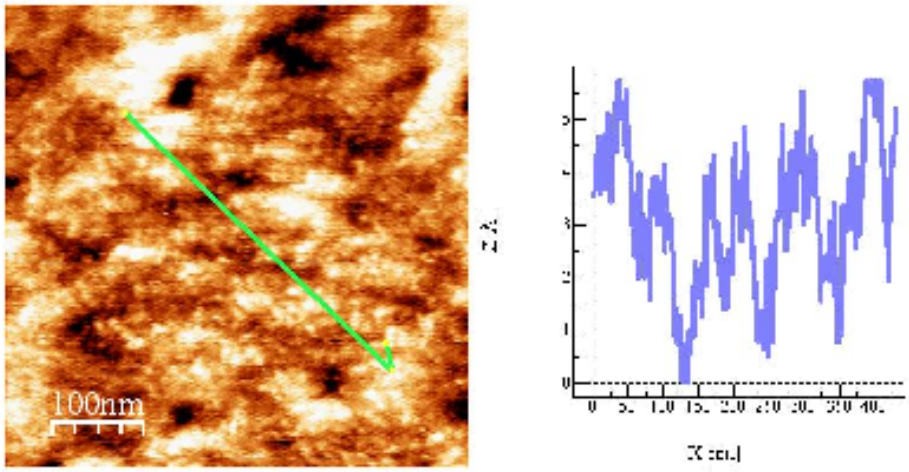

Figure 12 : Topographic image and corresponding scan profile of an amorphous $Fe_{80}B_{20}$ thin film deposited at -2.0 kV target potential, 5 • 10^{-3} mbar working gas pressure.

II.7. Conclusions.

In-situ stress measurements during sputtering of amorphous $Fe_{80}B_{20}$ films were presented. The glass substrate curvature is measured optically during growth and quantitatively related to the deposition induced accumulated stress. Three markedly different regions of stress have been distinguished. An initial apparent compressive stress related with the heat transfer of energetic arriving atoms as the target bias is turned on. This apparent stress disappears after switching the target potential off. A second regime where a tensile stress develops as islands nucleate and grow. A maximum of tensile stress occurs as the islands coalesce. Finally, a regime of compressive stress develops due to an 'atomic peening' mechanism. The deposition parameters of sputtered amorphous $Fe_{80}B_{20}$ films were optimized to achieve near zero stress amorphous $Fe_{80}B_{20}$ thin films to be used in micro-mechanical actuators.

References.

[1] S. Huang and X. Zhang. *'Study of gradient stress in biomaterial cantilever structures for infrared applications'*, Micromech. Microeng., **17**, 1211 (2007).

[2] C. Friesen and C. V. Thompson*, 'Reversible Stress Relaxation during Pre-coalescence Interruptions of Volmer-Weber Thin Film Growth'*, Phys. Rev. Lett., **89**, 126103 (2002).

[3] S. Dina, U. Geyer, and G. V. Minnigerode, *'Macroscopic intrinsic stress formation in amosphous CuTi films',* Ann. Phys., **4**, 623 (1995).

[4] R. Koch, *'The intrinsic stress of polycrystalline and epitaxial thin metal films',* J. Phys,: Condens. Matter, **6**, 9519 (1994).

[5] J. A. Thornton and D. W. Hoffman, '*Stress related effects in thin films',* Thin Solid Films, **171**, 5 (1989).

[6] Kevin Meyer, Ivan K. Schuller and Charles M. Falco, *'Thermalization of sputtered atoms',* J. Appl. Phys., **52**, 5803 (1981).

[7] A. S. Dehlinger, J. F. Pierson, A. Roman and Ph. Bauer, *'Properties of iron boride films prepared by magnetron sputtering'*, Surface and Coatings Technology, **174**, 331 (2003).

III

Magnetic anisotropy control in amorphous $Fe_{80}B_{20}$ as a function of the deposition parameters.

III.1. Introduction. 57

III.2. Magnetic anisotropy of deposited films. 57

III.2.1. Growth induced: angle deposition. 58

III.2.2. Stress induced. 60

III.2.3. Field induced. 61

III.3. Magnetic anisotropy of sputtered amorphous $Fe_{80}B_{20}$ thin films. 62

III.3.1. Balance of two contributions: stress induced and field induced anisotropy. 63

III.3.2. Balance of three contributions: stress , field and oblique incidence anisotropies. 68

III.3.2.a) Thick glass substrate. 70

III.3.2.b) Thin glass substrate (B) which long edge is parallel to the applied magnetic field……. 74

III.3.2.c) Thin glass substrate (C) which long edge is perpendicular to the applied magnetic field. 77

III.3.3. Magnetic anisotropy as a function of the target potential. 80

III.4. Conclusions. 82

References. 82

III.1. Introduction.

Magnetostrictive materials have attracted significant interest for sensor and actuator applications [1,2]. Due to their unique non-contact actuation, magnetostrictive materials are particularly appealing for wireless applications. In most sensor applications, a large magnetostriction needs to be induced at low magnetic field, hence requiring materials that have a combination of large saturation strain (λ_s) and low saturation field (H_k). On the other hand, the incorporation of these materials into micro-electromechanical systems (MEMS) requires a good control of the film magnetic anisotropy. For actuators, the maximum magnetostrictive strain is obtained when the magnetic moments are rotated coherently. Such a rotation is conveniently achieved by the application of an external magnetic field along the hard axis of an element which has a well defined uniaxial anisotropy. It is therefore essential, not only from the point of view of sensor applications, but also from that of understanding the material's magnetic behavior, that the magnetic anisotropy of the material is well defined, since the magnetic anisotropy strongly affects the magnetization process and therefore the shape of the B-H hysteresis loop. This chapter is concerned with the magnetic anisotropy of amorphous $Fe_{80}B_{20}$ thin films deposited by triode sputtering. A significant in-plane uniaxial magnetic anisotropy is observed in the as-deposited films. A fine control of the film final anisotropy direction due to the competition of *field induced, stress induced* and *oblique induced anisotropies* is achieved as a function of the deposition parameters. In addition, the resulting magnetic properties of amorphous $Fe_{80}B_{20}$ thin films are correlated with the measured stress studied in Chapter II, for the wide range of sputtering pressures [(2 - 25) • 10^{-3} mbar] and target potentials [(-0.5 to -2.0) kV].

III.2. Magnetic anisotropy of deposited films.

Magnetic materials display a directional dependence of their properties, and this is a consequence of the magnetic anisotropy. The magnetic anisotropy describes the preference of the magnetization to lie in a particular direction. In 1926 Honda and Kaya [3] discovered that the magnetization process in Fe single crystals is different in different crystallographic directions. In the absence of any applied external magnetic field the magnetization rests more comfortably in the <100> direction, called 'easy axis', whilst the <111> directions are said to be hard axis of magnetization. The easy and hard directions can be distinguished by the magnetic field needed to achieve magnetic saturation. This form of magnetic anisotropy is referred to as the *crystal anisotropy*, or *magnetocrystalline anisotropy*, which is intrinsic to the material. The crystal anisotropy originates from the spin-orbit interaction where the spin is coupled to the electron orbit. When a magnetic field is applied to rotate the spins, it also attempts to reorientate the electron orbit which is coupled to the crystal lattice.

The intrinsic crystal anisotropy is not preserved in amorphous materials, since the crystal field rapidly averages to 'zero' on a macroscopic scale because of the amorphous arrangement of the atoms. On the local scale, it can be assumed that there is some 'crystalline' anisotropy because of nearest interactions, which will be very of short range, and therefore the average macroscopic crystal anisotropy is closed to, or equal, to zero. It should be remembered that ferromagnetism is a result of the exchange energy which is mainly dominated by the interaction between adjacent electron spins and their separations. Instead a number of other magnetic anisotropies exist, which are usually induced in some manner, giving rise to a magnetic anisotropy which is uniaxial in direction. This means that there is a single, preferred direction, which for thin films is usually in the plane of the film due to the shape anisotropy. The tendency for the magnetization to lie along such an easy axis, can be expressed as an anisotropy energy density, E_K, as a function of *sin* θ:

$$E_k = K_u \sin^2 \theta \qquad (1)$$

where θ is the angle between the easy axis and the direction of magnetization and K_U is the uniaxial anisotropy constant (erg • cm^{-3}). It can be seen from these expressions that the anisotropy energy is a minimum when the magnetization is parallel to the easy axis (θ = 0º,180º), and is a maximum when magnetization is perpendicular to the easy axis (θ = 90º, 270º).

The magnitude of the induced anisotropy is usually monitored by measuring the anisotropy constant K_U (using Magneto-optical torque [4]) or the anisotropy field H_K (applied magnetic field necessary to saturate in the hard axis direction) which is related to the anisotropy constant:

$$K_u = \frac{1}{2} M_S \cdot H_K \qquad (2)$$

where M_S, is the saturation magnetization or magnetic moment per volume unit (emu • cm^{-3}).

For a given shape of the specimen, in the absence of 'magnetocrystalline' anisotropy, the direction of the easy axis in amorphous ferromagnetic materials are entirely determined both by stresses, either residual or applied or by the application of a magnetic field during deposition or annealing. The interaction between stresses and the magnetization is accordingly of primordial importance in the magnetic characteristics of the amorphous metals.

III.2.1. Growth induced: angle deposition.

The sputtering parameters have a significant effect on the structural and magnetic properties of a depositing film. As shown in Chapter II, at high sputtering energies (low

sputtering pressures and high target potentials) the films are in a state of high compressive stress, whereas at low sputtering energies (high sputtering pressures and low target potentials) a columnar texture can develop in the depositing film [5]. The columnar structure is formed by the self-shadowing of the incident atoms by the atoms already incorporated into the growing film. This columnar texture gives rise to a perpendicular anisotropy, because of the shape induced anisotropy of the columns. The magnetization prefers to lie along the length of the columns because of the lower magnetostatic energy. The columns, which are formed by the process of columnar growth, are dependent upon the angle at which the impinging atoms arrive at surface of the film. An empirical expression relates the angles of the impinging atoms, α, and the angle, β, at which the columns are formed, by the following equation [6]:

$$2 \tan \beta = \tan \alpha \qquad (3)$$

This is illustrated in Figure 1.a), where the columnar structure for atoms impinging at α = 30º is shown. In general, the formation of the columnar direction is not equal to the direction of the impinging atoms as expressed by equation (4). Columnar growth is strongly dependent on the deposition parameters and can develop in both sputter or evaporation deposition techniques. This columnar structure has also the effect of lowering the density of the films because of the more open structure which, in turn, has the effect of lowering saturation magnetization, besides severely degrading the magnetic properties of the material by inducing a perpendicular anisotropy in thin films.

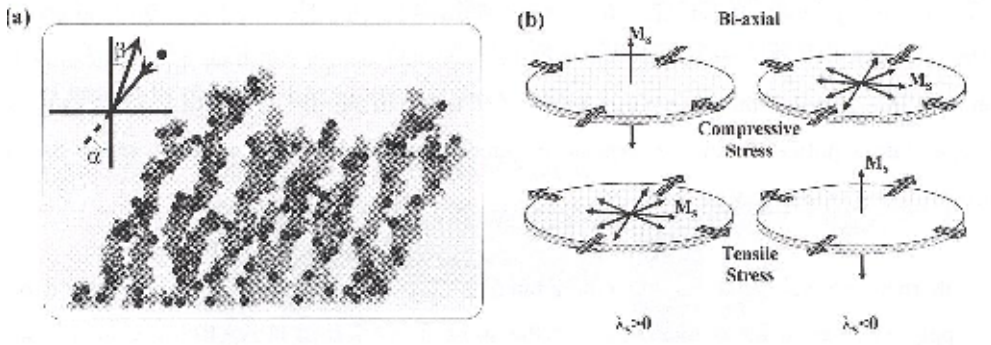

Figure 1 : a) Columnar structure for impinging atoms at α=30º to the substrate surface (Ref. 7). b) Anisotropy induced when a biaxial or higher order compressive or tensile stress exists.

For magnetostrictive films the intrinsic stresses induced during deposition have a strong influence on its magnetic anisotropy. Films deposited at high sputtering kinetics (for example lower pressures at high target potentials) show compressive stresses and no columnar structure formation, due to the atomic peening effect (Chapter I, Section I.3.4.). The magnetization will couple with the stresses induced through the magnetostriction to produce a growth induced anisotropy which can be perpendicular to the plane of the film. The direction of the anisotropy induced is dependent upon the sign of the magnetostriction and also the sign and the type of stress (uniaxial, biaxial, isotropic…) present within the film. This is illustrated in Figure 1.b). For

a perpendicular anisotropy to be induced in a film, the stresses induced therefore must be at least biaxial in form to rotate the magnetization out of the plane of the film as shown in Figure 1.b). It is unlikely that a film deposited either by sputtering or vapour deposition will develop a uniaxial stress direction, because of the random nature of the growth process. The intrinsic stresses which occur will be very random in direction on a local scale, giving rise to stresses which are likely to be isotropic in nature and which can account for the perpendicular anisotropy.

III.2.2. Stress induced.

Stresses in thin films can also be extrinsically induced due to the differing thermal expansion coefficients of the film and substrate as the film/substrate system cools after the deposition and contracts by different amounts. A film which is deposited onto a substrate which has a larger thermal expansion coefficient will be placed in a state of compressive stress, whereas a substrate with lower thermal expansion coefficient will place the deposited film in a state of tensile stress. If the stress is either bi-axial or isotropic, an uniaxial anisotropy may be induced, depending on the sign of magnetostriction (Figure 1.b)). For substrates and films with similar expansion coefficients which are deposited at low deposition temperatures, this problem is usually avoided.

An alternative method of inducing an uniaxial anisotropy during the deposition is to apply an external mechanical stress to the substrate which will induce a stress of opposite sign [7]. The substrate is mechanically clamped over a knife edge at its two extreme points. The strain in the film depends directly on the radius of curvature induced in the samples, as shown in Figure 2.

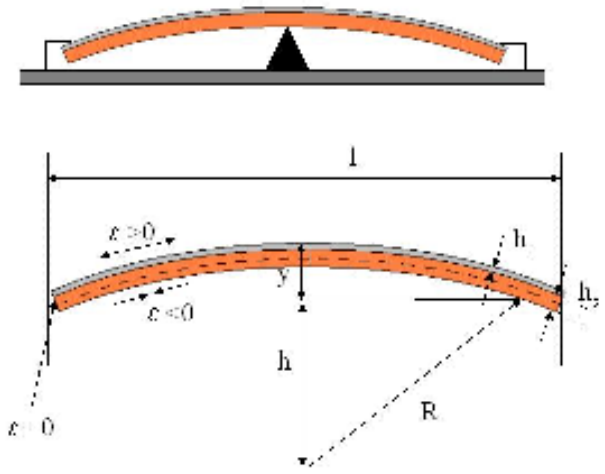

Figure 2 : Schematic of the experimental method used for the introduction of mechanical strain into the film/substrate. Illustrative profile of the bent substrate from which the radius of curvature is calculated.

This radius of curvature *R* can be estimated from Figure 2, using the following geometric relation:

$$R^2 = \left(\frac{l}{2}\right)^2 + h^2 \tag{4}$$

Substituting *l* = *R*- *y*, and assuming *l* >> *y*, leads to:

$$R = \frac{l^2 + 4y^2}{8y} \approx \frac{l^2}{8y} \tag{5}$$

Assuming that the central element of the slide remains unstrained, the tensile strain in the top surface of the substrate is given by the following expression referring to labels shown in Figure 2.

$$\varepsilon = \frac{\Delta P}{P} = \frac{2\pi(R - h_f) - 2\pi(R - {h_s}/{2} - h_f)}{2\pi(R - {h_s}/{2} - h_f)} = \frac{h_s}{2R - h_s - 2h_f} \approx \frac{h_s}{2R} \tag{6}$$

where $R >> h_s, h_f$ was assumed, being *h* the thickness of the film and the substrate respectively.

On the other hand, the saturation magnetostriction constant λ_S can be calculated from the variation of the strain induced magnetic anisotropy field, H_k, with the applied stress σ [8] using the following equation:

$$\lambda_s = \frac{M_S}{3}\frac{H_k}{\sigma}, \sigma = \varepsilon E_S \tag{7}$$

where M_s is the saturation magnetization of the thin films, ε is the value of the strain and finally E_s, is the Young's modulus of the substrate.

III.2.3. Field induced.

Inducing an uniaxial anisotropy by the application of a magnetic field parallel to the plane of the depositing film is a widely used technique. The magnetic field must be sufficient to saturate the sample and to ensure single domain existence. An uniaxial anisotropy appears, that is attributed to the short-range directional ordering of the atomic pairs (e.g. Fe-Fe) [9] . The kinetic energies of the impinging sputtered atoms, which tend to be mobile at the surface of the film, allow a preferred orientation that minimises the energy of the system of like atomic pairs

and aligns then parallel to the magnetic field. The domain structure for such a demagnetised sample displays a strong preference for the domain walls to lie parallel to the induced easy axis. The directional ordering obtained is much larger in the depositing films compared to conventional magnetic annealing were the directional ordering is not as high. In our sputtering system, the magnetic field is provided by a Hemlholtz coil that are used to confine the plasma.

III.3. Magnetic anisotropy of sputtered amorphous $Fe_{80}B_{20}$ thin films.

The magnetic properties of a metallic glass, such as magnetic anisotropy, coercive field, permeability, etc... are extremely sensitive to the structure and can be tailored within certain ranges continuously maintaining the amorphous structure [10]. The magnetic anisotropy of magnetostrictive $Fe_{80}B_{20}$ thin films deposited by triode sputtering was found to be a balance of three contributions : *stress induced*, *field induced* and *oblique incidence anisotropy*. This balance is determined by the film deposition parameters and substrate shape/thickness. For example, it was measured that *oblique incidence anisotropy* starts to develop for target potentials around -1.0 kV, disappearing for larger values even when the deposition angle relative to the direction perpendicular to the surface of the substrate was up to 60º. Thus, for $Fe_{80}B_{20}$ films grown at -2.0 kV of target potential, *oblique incidence anisotropy* is canceled and only two contributions to the anisotropy are present in the balance: *field induced* and *stress induced anisotropy*.

It was also shown that if the film accumulates stress, the shape and thickness of the substrate affect the final film magnetic anisotropy direction. For thick enough substrates, able to avoid bending due to the film deposited stress, the film accumulated stress is isotropic, avoiding the existence of any preferred direction for the easy magnetization axis as a consequence of the magneto-elastic coupling (if no *field induced* or *oblique induced anisotropy* is present). But, in the case of the thin glass cantilevers used for stress measurement, bending of the cantilevers is found to be larger in the long dimension edge than that of the short dimension, giving rise to a film stress anisotropy and consequently a preferred direction for the easy magnetization axis, as a consequence of the magneto-elastic coupling.

In this chapter, the magnetic anisotropy is studied as a function of the deposition parameters for two different cases. In the first case, a high target potential is used, -2.0 kV, giving rise to a film magnetic anisotropy that is a balance of only two different contributions: *stress induced* and *field induced anisotropy*. In the second case, the target potential is lowered to -1.0 kV to study the effect of the angle deposition, applied magnetic field and shape/thickness of the substrate in the film magnetic anisotropy.

All the deposited films exhibit an overall uniaxial magnetic anisotropy, as shown in Figure 3, where the angular dependence of the remanence for a film deposited at -2.0 kV and 8 • 10^{-3} mbar is shown. There is a clear hard magnetization axis direction with linear and reversible B-H hysteresis loops corresponding to a magnetization change that occurs by coherent spin rotation. Depending on the deposition parameters, the values of the anisotropy field H_k vary between 5 Oe and 25 Oe. Perpendicular to this hard magnetization axis there is an easy magnetization axis direction along which B-H hysteresis loops are square. The magnetization reversal along the easy axis takes place by domain wall nucleation and propagation. Depending on the deposition parameters, values of the coercive field H_c between 4 Oe and 15 Oe were obtained.

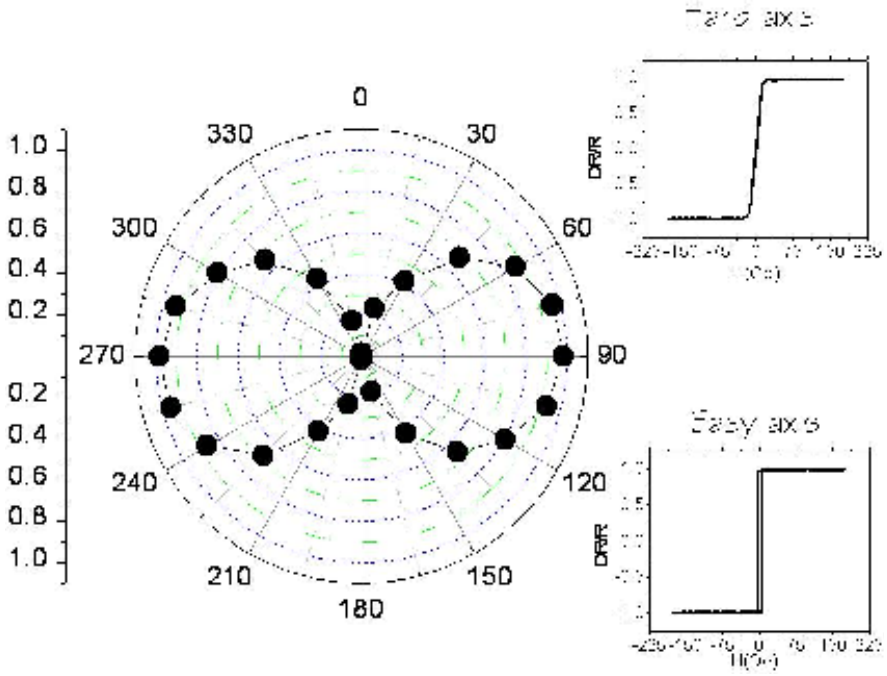

Figure 3 : Angular dependence of the remanence for a $Fe_{80}B_{20}$ film deposited at -2.0 kV and 8 • 10^{-3} mbar of Ar working pressure. The insets show the hard and easy axis loops. DR/R are the normalized reflectivity changes as a function of the applied magnetic field.

The value of the anisotropy field H_k was determined by two different techniques : a) the study of the B-H hysteresis loops, where H_k was obtained from the saturation field along the hard magnetization axis, and b) magneto-optical torque (Chapter I, Section I.4.2.). The value of H_k was the same within 5%. The value of the coercive field H_c was obtained from the B-H hysteresis loops along the easy magnetization axis.

III.3.1. Balance of two contributions: stress induced and field induced anisotropy.

Amorphous $Fe_{20}B_{20}$ films were grown on thin glass cantilevers and thick substrates with the following deposition parameters: a fixed target potential of -2.0 kV, a wide range of

sputtering pressures [(2 - 25) • 10^{-3} mbar] and 45º angle deposition. The resulting film magnetic anisotropy was found to be a balance of two different contributions: *stress induced* and *field induced anisotropy.* The film B-H hysteresis loops along the easy and hard axis directions are shown in Figure 4.a) and b).

As explained in Chapter I, Section I.2.4., all the $Fe_{20}B_{20}$ films were grown under a small external applied magnetic field used to confine the plasma. This magnetic field gives rise to an uniaxial anisotropy resulting from a directional short range atomic pair-ordering in the amorphous matrix with a preferred direction imposed by the direction of the film magnetization during deposition [11]. For thicker substrates (1 mm), in which bending due to the film accumulated stress is not possible, the easy magnetization axis points parallel to the direction of the plasma confinement field in all the pressure range, as corroborated for three different pressures in the low [2 • 10^{-3} mbar], medium [12 • 10^{-3} mbar] and high sputtering pressures [25 • 10^{-3} mbar]. However, in the case of the thin glass cantilevers/substrates used to measure the film stress, the deposited film exhibit a different behavior of its magnetic anisotropy, depending its direction on the sputtering pressure.

As shown in Figure 4.c), the short edge of the substrate/cantilever is placed parallel to the applied magnetic field. For lower sputtering pressures, the film easy axis points along the direction of the plasma confinement field., i.e. parallel to the short edge of the glass substrate/cantilever. But, for sputtering pressures above 8 • 10^{-3} mbar, the film easy axis direction starts deviating from the plasma confining field direction and turns perpendicular at about 14 • 10^{-3} mbar, as shown in Figure 4.d). This means that *field induced anisotropy* is dominant for lower sputtering pressures where the energy of the arriving atoms is higher, but as pressure increases, there is a change in the uniaxial anisotropy that is attributed to an additional anisotropy (K_{add}), where $K_{total} = K_{induced} \pm K_{add}$ with $H_k = 2\ K_{total} / M_s$. The positive sign is for parallel and the negative sign is for perpendicular anisotropies. In the latter , K_{total} is negative and represents an anisotropy rotated 90° from the field induced anisotropy. This additional uniaxial anisotropy appears only in the case of thin glass substrates, rejecting the possibility of an magnetic anisotropy appearance due to the effect of oblique angle incidence. It is the result of a stress imbalance in the amorphous $Fe_{80}B_{20}$ film, due to the fact that the net film accumulated stress, in this case in the compressive direction, is not isotropic. It also depends on the shape of the substrate as explained below in II.3.2).

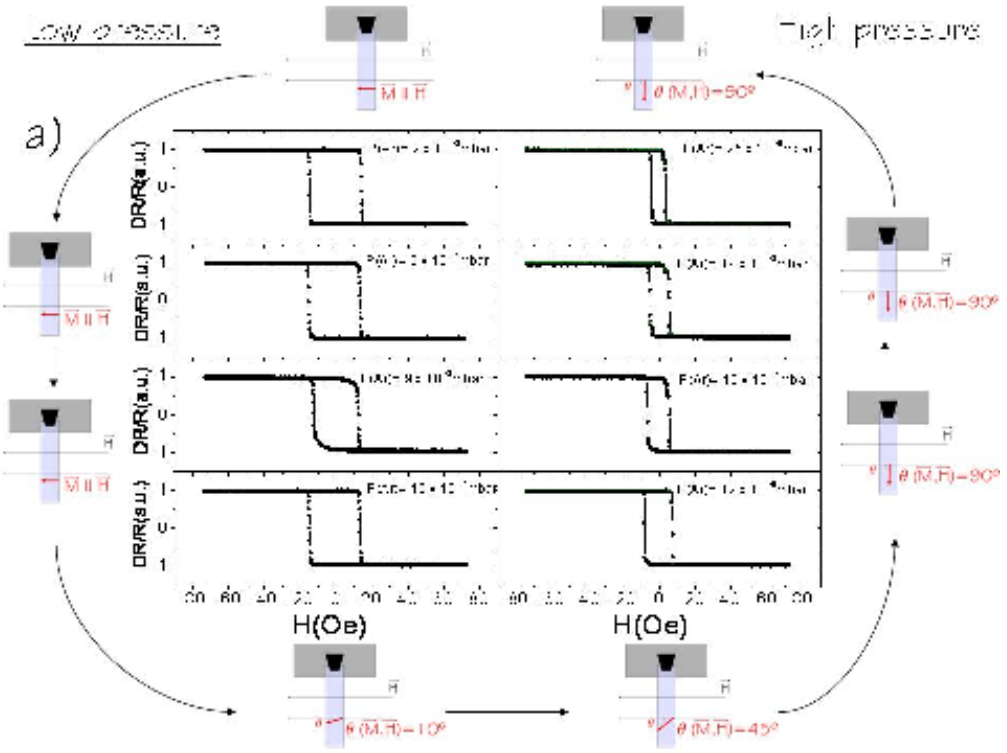
a)
DR/R(a.u.)
H(Oe)
H(Oe)
M ∥ H
θ (M,H)=90°
θ (M,H)=10°
θ (M,H)=45°

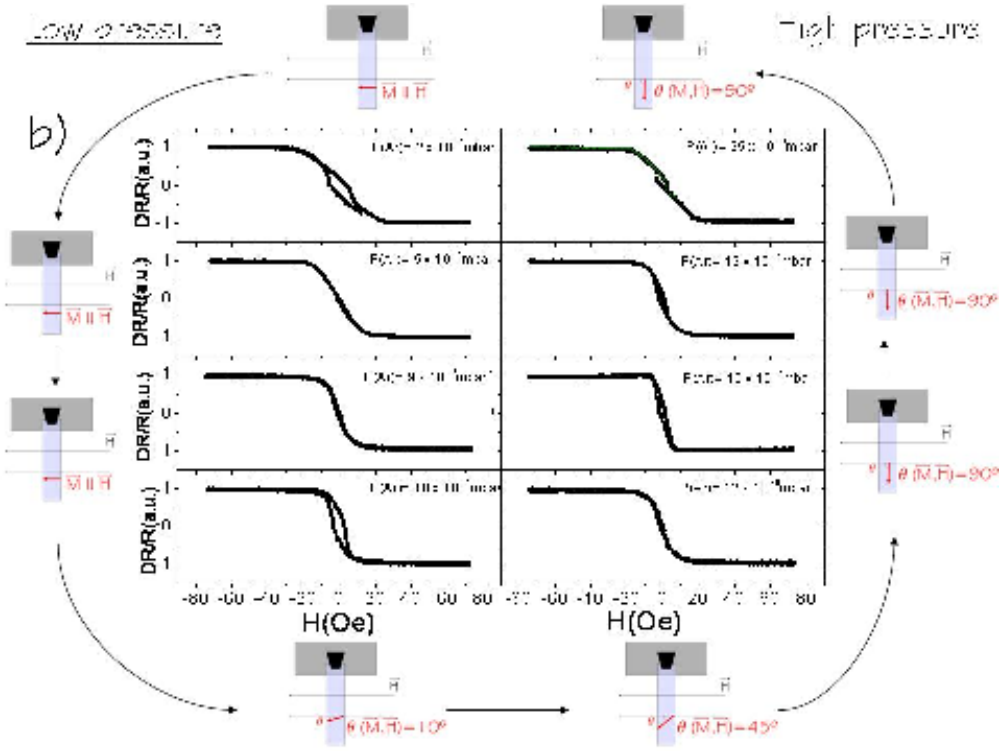
b)
DR/R(a.u.)
H(Oe)
H(Oe)
M ∥ H
θ (M,H)=90°
θ (M,H)=10°
θ (M,H)=45°

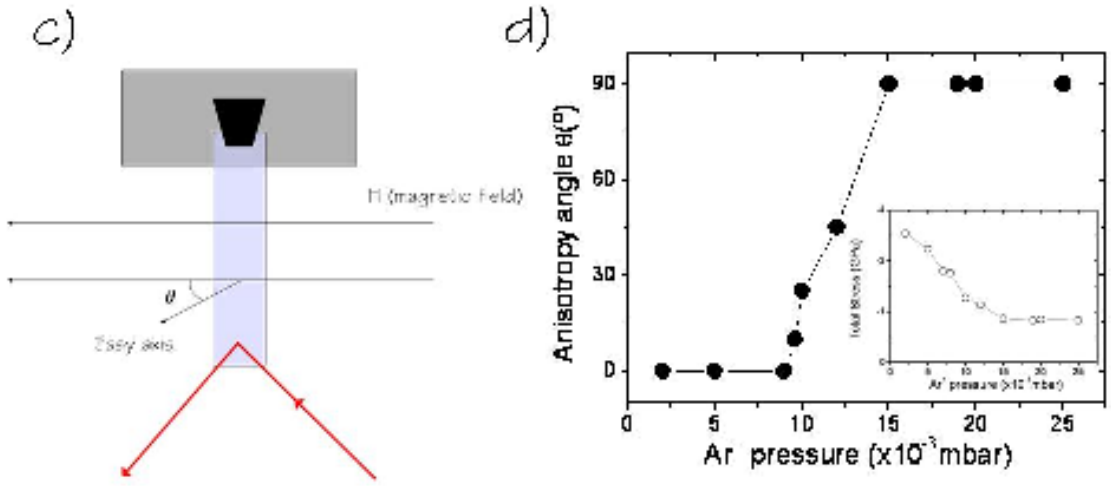

Figure 4 : a) B-H hysteresis loops along the easy magnetization axis for various working pressures. b) B-H hysteresis loops along the hard magnetization axis for various working pressures. c) Schematic picture of the substrate/cantilever used to measure the film accumulated stress and its orientation relative to the applied magnetic field. d) Anisotropy angle direction as a function of the Ar working pressure for a fixed target potential of -2.0 kV. Inset: Total accumulated stress as a function of the Ar working pressure (Figure 6, Chapter II).

In our experimental setup, the cantilever/substrate shape and placement renders the long dimension edge free to bend and the short dimension edge constrained near the clamping. As calculated in earlier works [12], depending on the cantilever length-to-width ratio, there is an one-dimensional (1D) or two-dimensional (2D) bending of the substrate/cantilever, as shown in Figure 5. In the 1D case, measurable curvature or stress relaxation exists only along the length of the substrate. This means that stress along the film width direction accumulates, as shown in Figure 5.a). In the 2D case, a measurable curvature or stress relaxation exists both along the length and width of the substrate. This means that accumulated stress is isotropic in the film, as shown in Figure 5.b). Depending on the cantilever length to width ratio we can have the first (1D), the second (2D) or an intermediate state in which accumulated stress is not isotropic in the film, as observed in Figure 5.c). For very small aspect ratios (larger width than length), the effect of the clamping is to restrict the bending to a purely one-dimensional case (1D). However, for the other extreme of a very long sample the dimensionality approaches two (2D), as expected. In our case, the long dimension edge of the substrate/cantilever is approximately four times larger than that of the short dimension. For this aspect ratio, the beam deformation is not purely two dimensional as observed in Figure 5.c), giving rise to a stress imbalance in the substrate curvature and consequently in the deposited film. Thus, the net accumulated stress is larger in magnitude along the short direction, and as experimentally shown enough to rotate the magnetic anisotropy through magnetoelastic effects. A positive saturation magnetostriction constant combined with a compressive stress results in an easy axis perpendicular to the stress direction, and consequently parallel to the long axis direction.

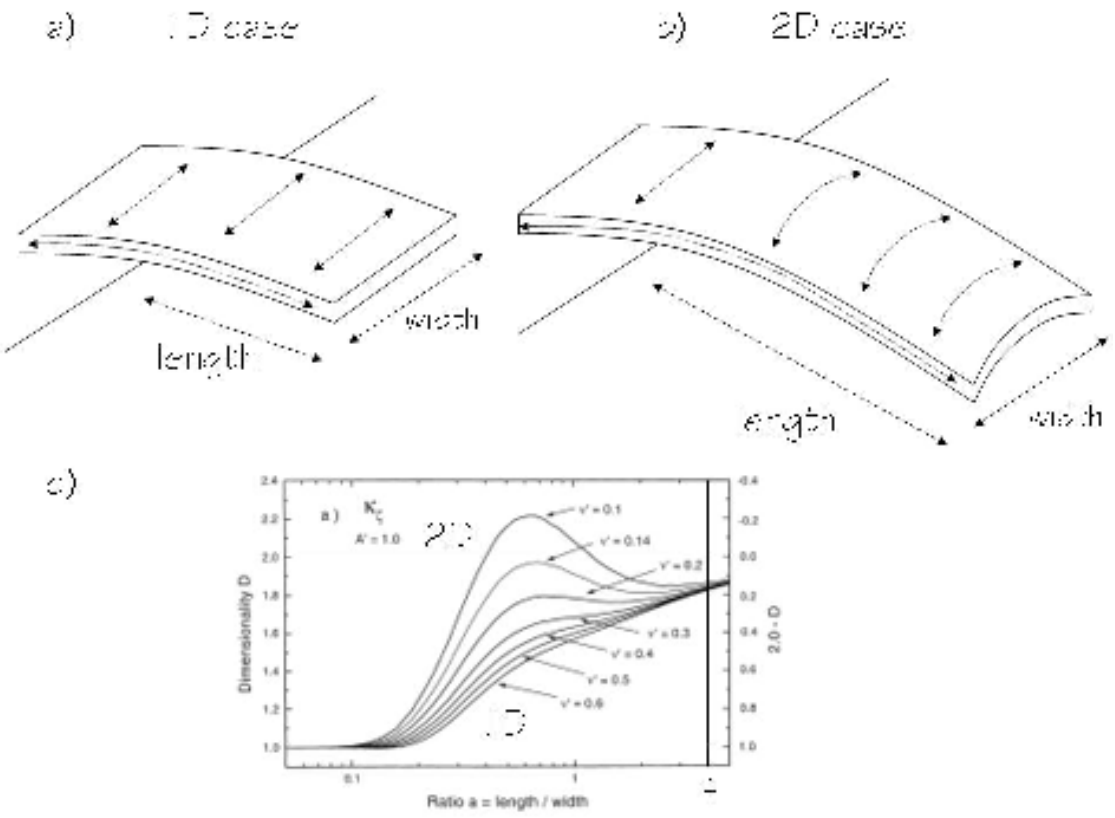

Figure 5 : Dimensionalities of the bending curvatures referring to the deflection for elastic beams clamped at one edge and loaded with an isotropic stress on one surface as a function of the aspect ratio.

As shown in Figure 6.a), the value of the film anisotropy constant K_{total} changes sign at about 14 • 10^{-3} mbar. This value was measured using a magneto-optical torque technique explained in Chapter I, Section I.4.2. The value of the film coercive field H_c from B-H hysteresis loops along the easy magnetization axis as a function of the working pressure is represented in Figure 6.b). A low ~4 Oe coercive field is achieved at pressures above 20 • 10^{-3} mbar. In a high magnetostrictive material, usually residual inhomogeneous stress inherent to the fabrication process hinders domain wall motion [13]. This is corroborated with the fact that coercive field H_c follows the same behavior as the film total accumulated stress represented in the inset of Figure 6.b).

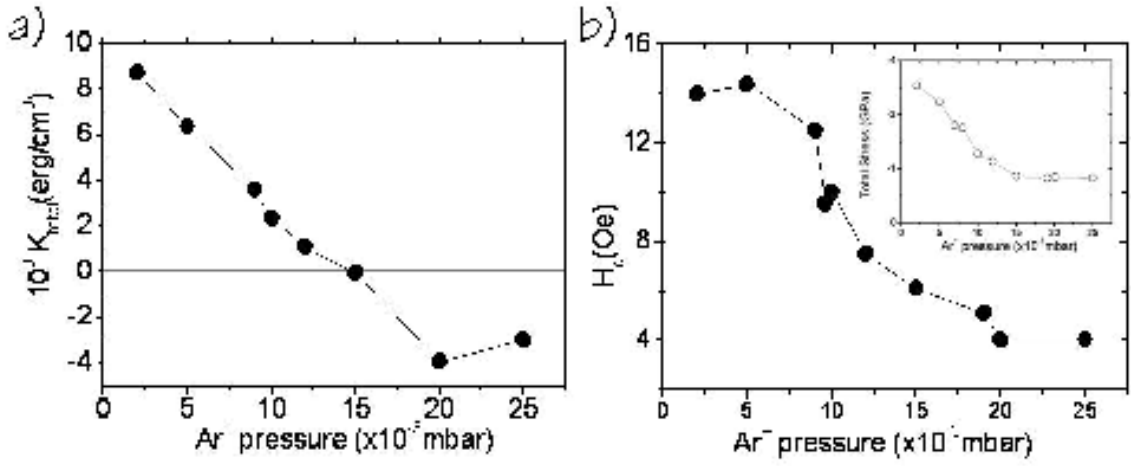

Figure 6 : a) Film anisotropy constant K_u and b) and coercive field Hc as a function of Ar working pressure measured using the magneto-optical torque technique and transversal MOKE. The studed films were deposited at a fixed target potential of –2.0 kV. Inset: Total accumulated stress as a function of the Ar working pressure (Figure 6, Chapter II).

III.3.2. Balance of three contributions: stress , field and oblique incidence anisotropies.

Amorphous $Fe_{20}B_{20}$ films were grown on thin glass cantilevers and thick substrates with the following deposition parameters: target potential (-1.0 kV), Ar working pressure ($8 \cdot 10^{-3}$ mbar) and different deposition angles α, relative to the direction perpendicular to the surface of the substrate (0º, 30º, 45º and 60º) as illustrated in Figure 7.a). In this case, the in-plane projection of the oblique incidence angle is perpendicular to the direction of the applied magnetic field. The film total accumulated stress is slightly compressive, as shown in Figure 7 of Chapter II. Films deposited in an off axis arrangement are found to have an additional uniaxial magnetic anisotropy as a result of the oblique incidence of the atomic flux onto the substrate [Section III.2.1.]. This extra anisotropy increases with increased oblique angle. Then, the resulting magnetic anisotropy is a balance of three different contributions: *stress induced*, *field induced anisotropy* and *oblique incidence anisotropy.* As explained in Section III.2.1., this uniaxial magnetic anisotropy induced in thin films deposited by oblique incidence has long been established [14,15], and it is generally associated with the film microstructure and surface morphology [16,17]. Both of these film properties are intimately related to a self-shadowing of the incident atom by the atoms already incorporated into the film growth [18,19] leading to a formation of columnar structures that tilt toward the deposition direction with respect to the substrate normal. This phenomena produces a *uniaxial magnetic anisotropy* parallel to the plane of incidence, as illustrated in Figure 7, where the columnar structure for atoms impinging at α = 30º is shown. It is also shown that the hard axis saturation field increases with the oblique deposition angle.

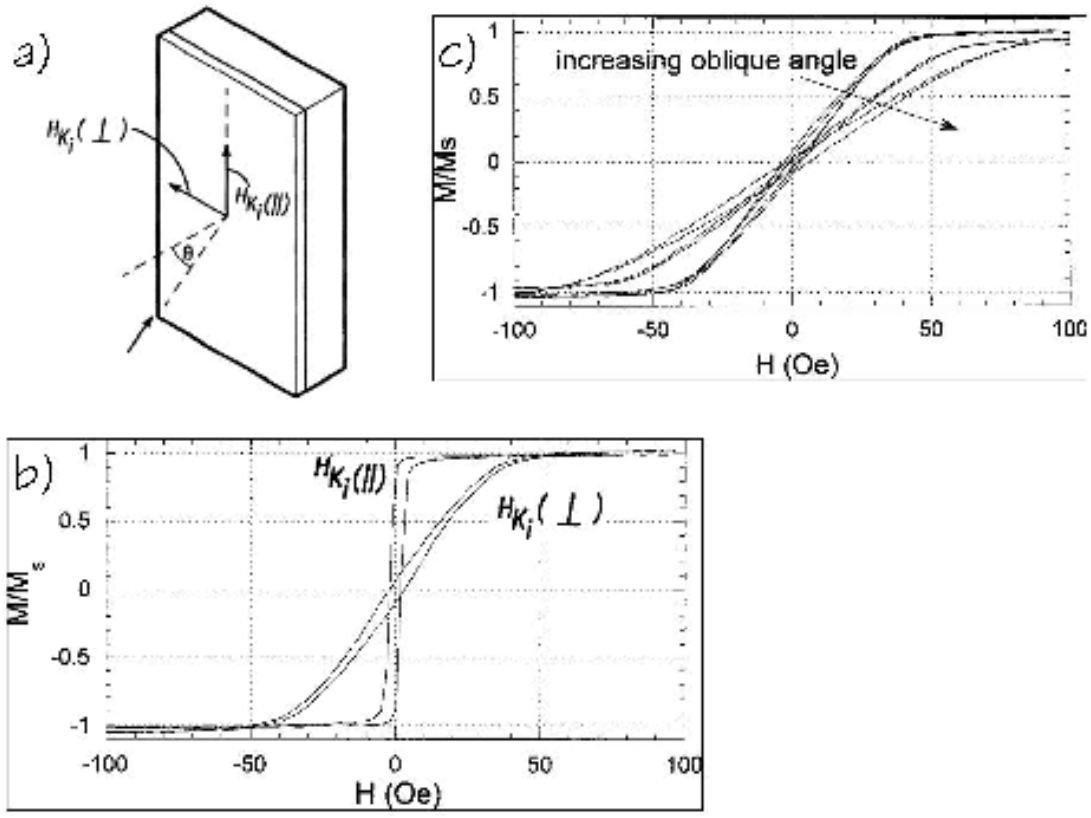

Figure 7 : a) Oblique view of the substrate with a material layer being deposited at a non-zero deposition angle. b) Hard axis and easy axis hysteresis loops for Fe-Co-B sputtered films [20]. c) Hard axis hysteresis loops for Fe-Co-B sputtered films with increasing oblique incidence of the atomic flux angle.

Three different substrates were deposited at the same time for different deposition angles α : a thick glass substrate (A) unable to bend due to the film accumulated stress, a thin glass substrate whose long edge is parallel to the applied magnetic field (B), and a thin glass substrate whose long edge is perpendicular to the applied magnetic field (C), as shown in Figure 8. In the case of substrate B, the *stress magnetic anisotropy* should add to the field induced anisotropy, but in the case of substrate C, the *stress magnetic anisotropy* should add to the *oblique incidence anisotropy*. So, it is proposed that if some differences in the film magnetic anisotropy between substrates B and C exist, will demonstrate the effect of the substrate geometry in the film final magnetic anisotropy.

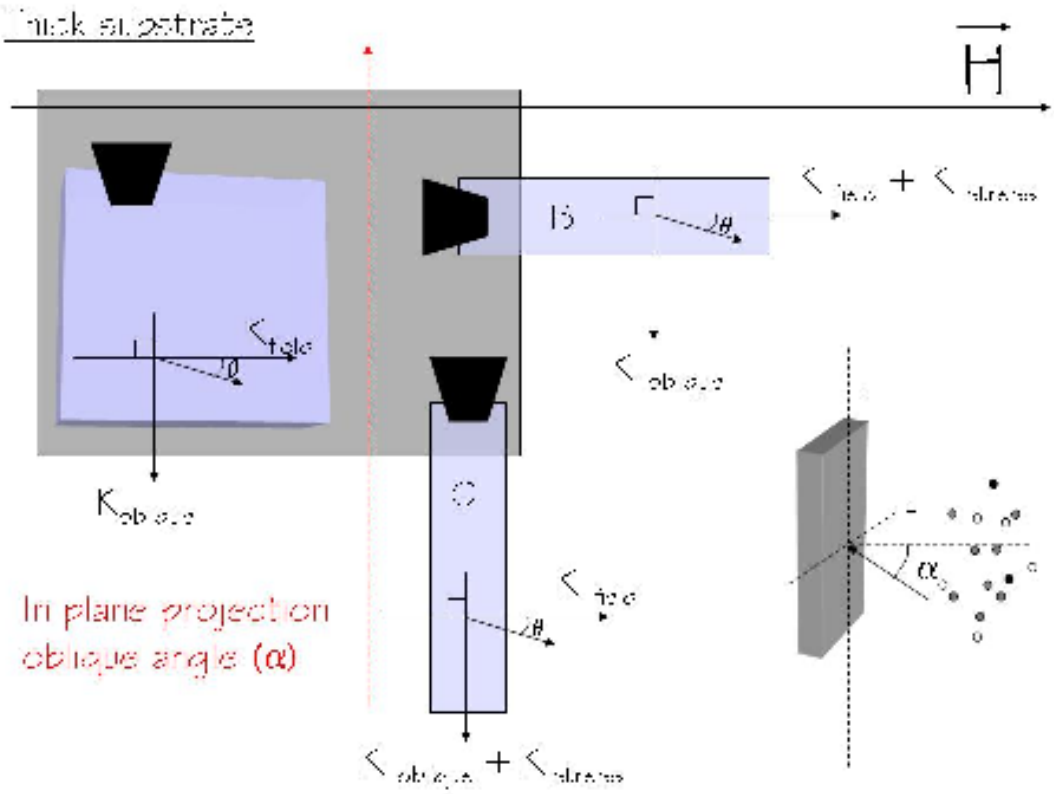

Figure 8 : Three different substrates were deposited at the same time for different deposition angles (α) : a thick glass substrate (A), a thin glass substrate which length in parallel to the applied magnetic field (B) so as to add the effect of stress to the field induced anisotropy, and a thin glass substrate which length in perpendicular to the applied magnetic field (C) so as to add the effect of stress to the oblique incidence anisotropy. The oblique incidence magnetic anisotropy is perpendicular to the field induced magnetic anisotropy in the three cases.

III.3.2.a) Thick glass substrate.

As illustrated in Figure 8, the in-plane projection of the oblique angle was perpendicular to the applied magnetic field. For lower angle deposition (α ~ 0º), the film easy axis magnetization points parallel to the applied magnetic field. But as the deposition angle increases, the film easy axis starts deviating from the plasma confining field direction and turns perpendicular at about α = 45º, as shown in Figure 9, where the B-H hysteresis loops along the hard and easy magnetization axis are shown. This means that *field induced anisotropy* is dominant for lower deposition angles, but as deposition angle increases, there is a change in the uniaxial anisotropy that is attributed to the *oblique incidence anisotropy* ($K_{oblique}$), where $K_{total} = K_{induced} - K_{oblique}$ with $H_k = 2 \bullet K_{total} / M_s$. In this case, the substrate bending due to the accumulated stress is not possible, avoiding any anisotropic behaviour of the accumulated stress that can result in a favourable film easy axis direction.

A similar result was reported in the literature for sputtered amorphous Fe-Co-B films [20], in which the field induced anisotropy direction was chosen perpendicular to the oblique induced anisotropy direction. It was shown that if substrates size is bigger than the target size, a rotation

of the magnetic anisotropy is shown from regions inside the target edge to regions further away from the centre of the target. Films deposited in regions of the substrate inside the target edge show a field induced anisotropy, decreasing the anisotropy field in the vicinity directly above the target edge. Further away from the centre of the target, the uniaxial anisotropy was found to rotate 90º and then began to increase with distance, due to the oblique induced anisotropy. Moreover, the easy axis coercive field was found not to depend strongly on substrate angle deposition.

The B-H hysteresis loops along the hard and easy magnetization axis for different deposition angles are shown in Figures 9.a)–e). The film easy and hard axis direction are schematically represented in red and blue respectively.

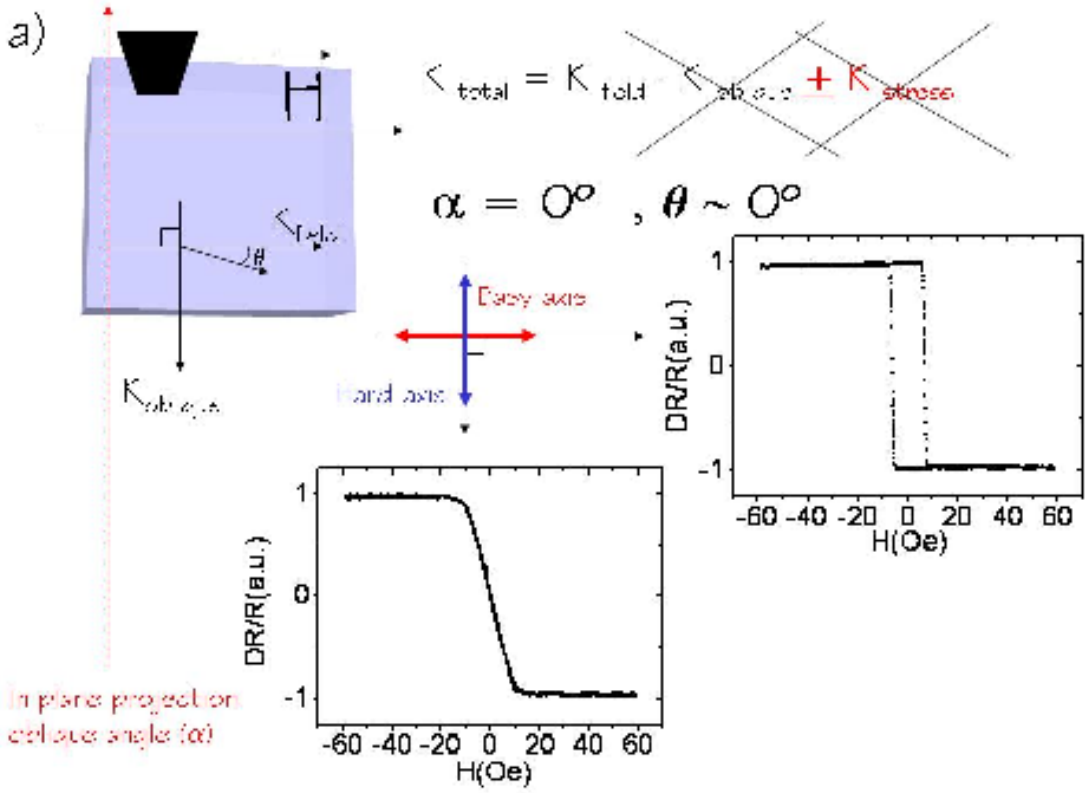

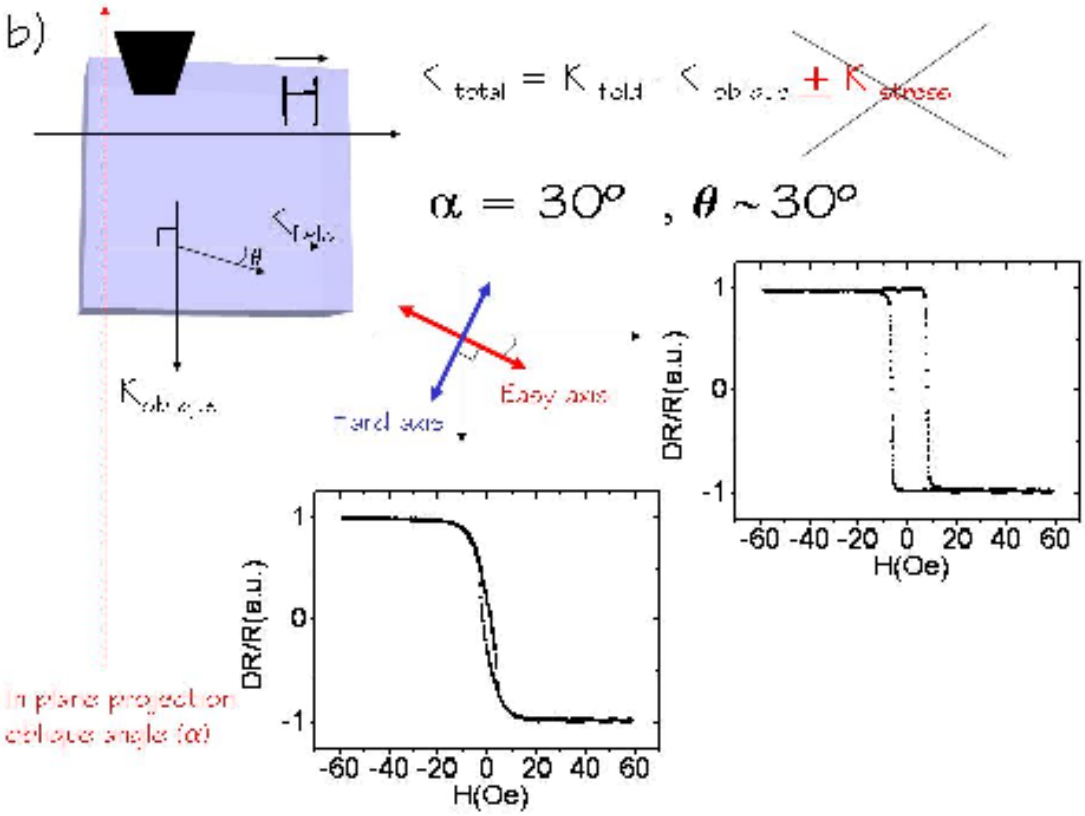
b)
H
$K_{total} = K_{fold} + K_{shape} + K_{stress}$
$\alpha = 30°$, $\theta \sim 30°$
Easy axis
Hard axis
In plane projection of the shape angle (α)
DR/R(a.u.)
H(Oe)

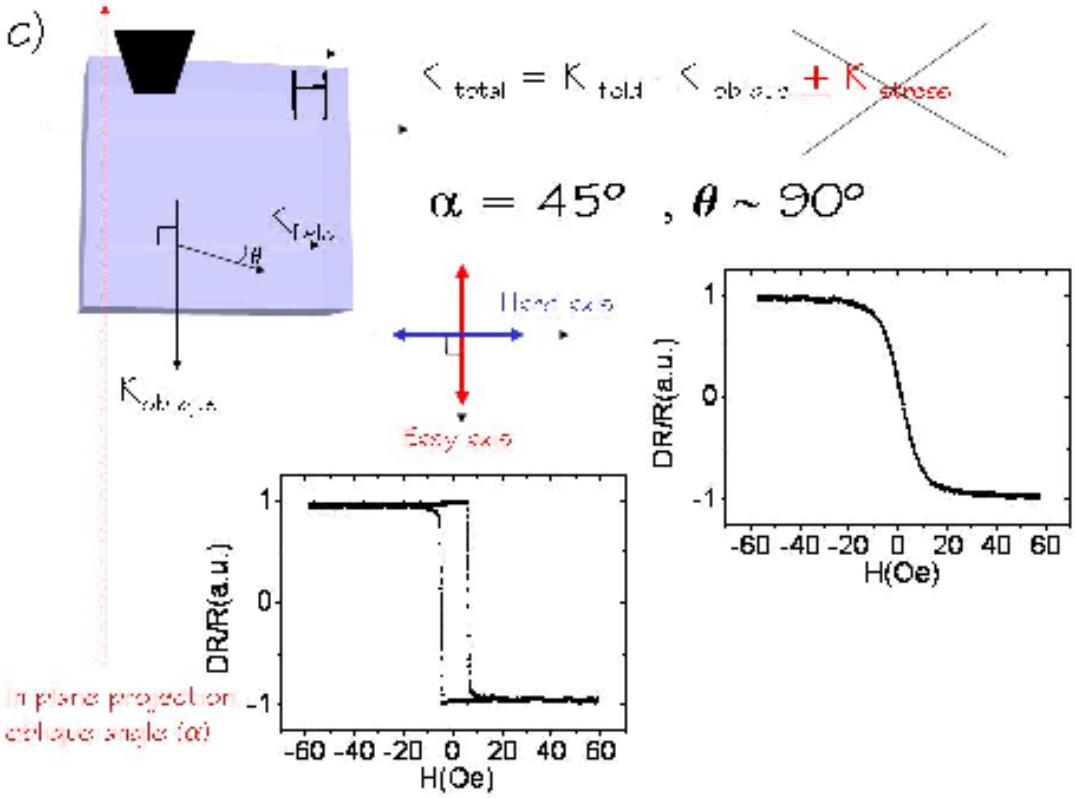
c)
H
$K_{total} = K_{fold} + K_{shape} + K_{stress}$
$\alpha = 45°$, $\theta \sim 90°$
Easy axis
In plane projection of the shape angle (α)
DR/R(a.u.)
H(Oe)

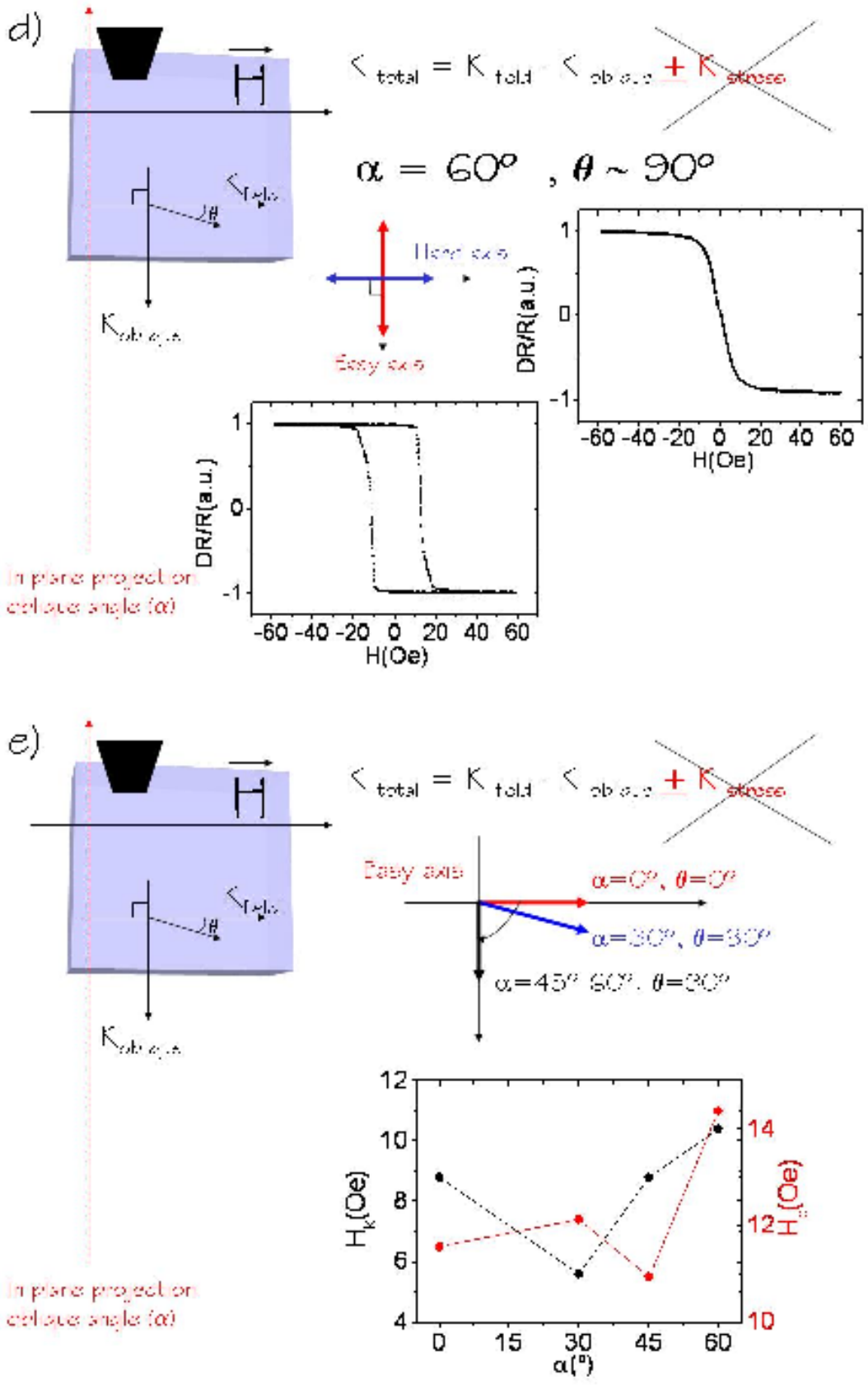

Figure 9 : a)-d) Hard and easy magnetization axis loops and easy axis direction for a thick glass substrate (A) and four different deposition angles (α) .e) Anisotropy angle direction (θ), coercive field (H_c) extracted from the easy axis loops and anisotropy field (H_k) extracted from the hard axis loops.

III.3.2.b) Thin glass substrate (B) which long edge is parallel to the applied magnetic field.

In this case, the in-plane projection of the oblique incidence angle was perpendicular to the applied magnetic field, while the direction of the *stress induced anisotropy* was parallel. The combination of these orthogonal anisotropies gives rise to a total anisotropy that can be expressed as $K_{total} = (K_{induced} + K_{stress}) - K_{oblique}$. Increasing the angle of deposition, the anisotropy rotates up to 45º rising the value of the anisotropy field with the angle of deposition as shown in Figure 10, where the B-H hysteresis loops along the hard and easy magnetization axis are shown. This means that *field induced anisotropy* is dominant for lower deposition angles, but as deposition angle increases, there is a change in the uniaxial anisotropy that is attributed to the *oblique incidence anisotropy* ($K_{oblique}$). But, as a different from the case of the thicker substrate (A), the easy axis direction does not rotate 90º. As substrate bending due to the film accumulated stress was possible, an anisotropic behaviour of the accumulated stress gives rise to a favourable easy axis direction, in this case parallel to the long edge. It can be then stated that the *stress induced anisotropy* compensates the effect of the *oblique induced anisotropy*.

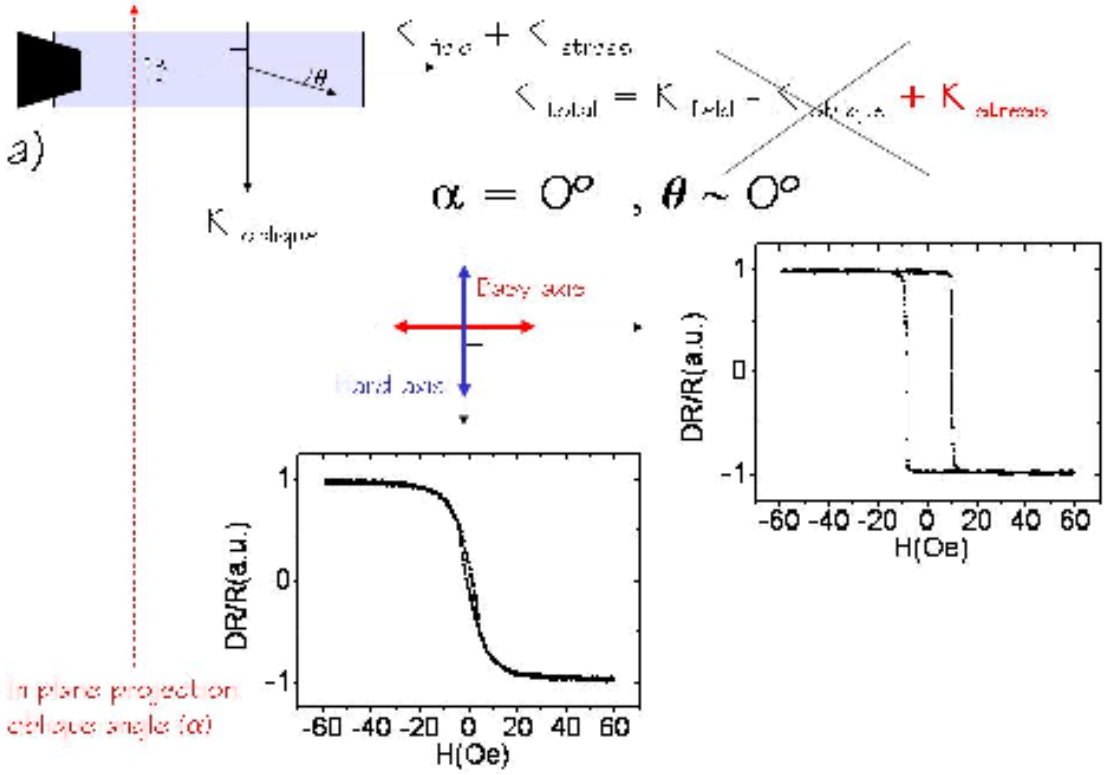

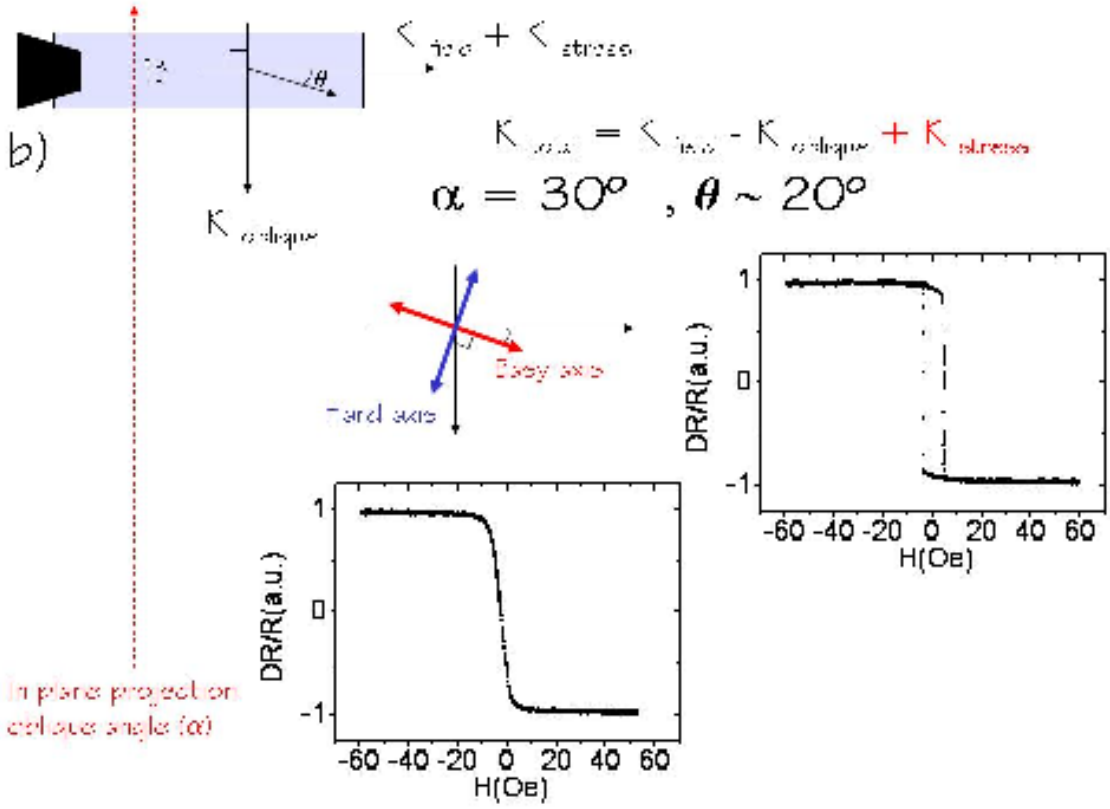
b)
$K_{oblique}$
$K_{total} = K_{face} - K_{oblique} + K_{stress}$
$\alpha = 30°$, $\theta \sim 20°$
Easy axis
Hard axis
In plane projection
oblique angle (α)
DR/R(a.u.)
H(Oe)
1
0
-1
-60 -40 -20 0 20 40 60

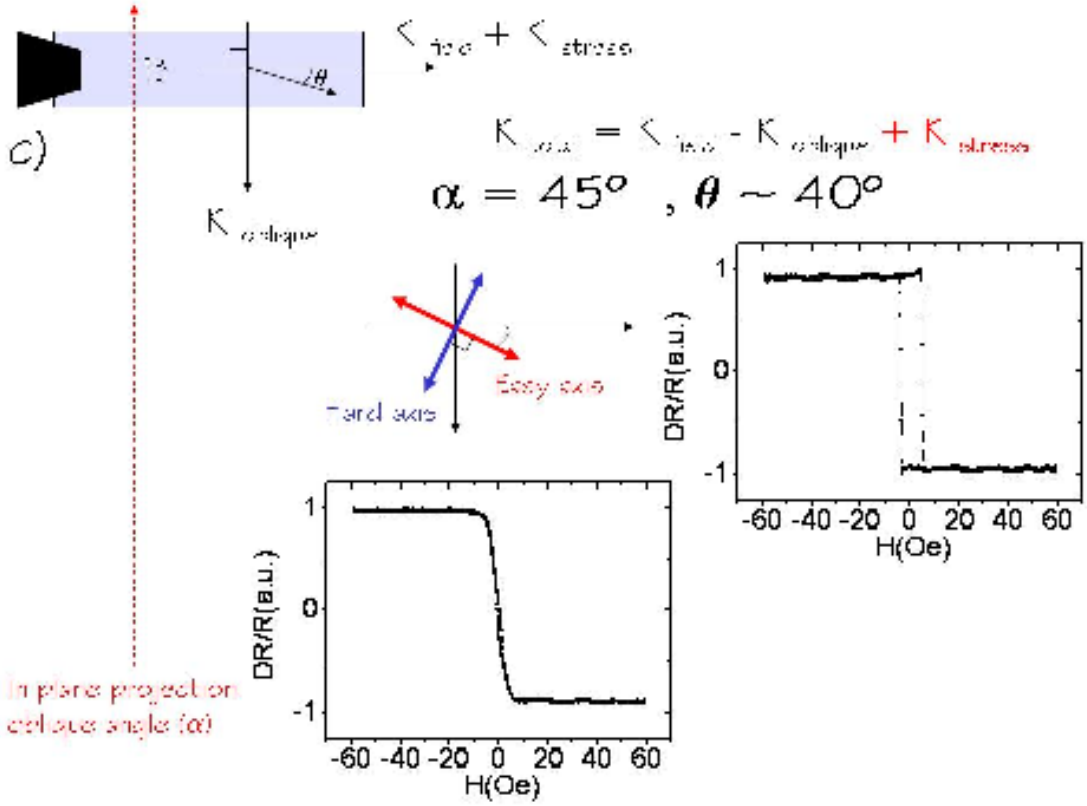
c)
$K_{oblique}$
$K_{total} = K_{face} - K_{oblique} + K_{stress}$
$\alpha = 45°$, $\theta \sim 40°$
Easy axis
Hard axis
In plane projection
oblique angle (α)
DR/R(a.u.)
H(Oe)
1
0
-1
-60 -40 -20 0 20 40 60

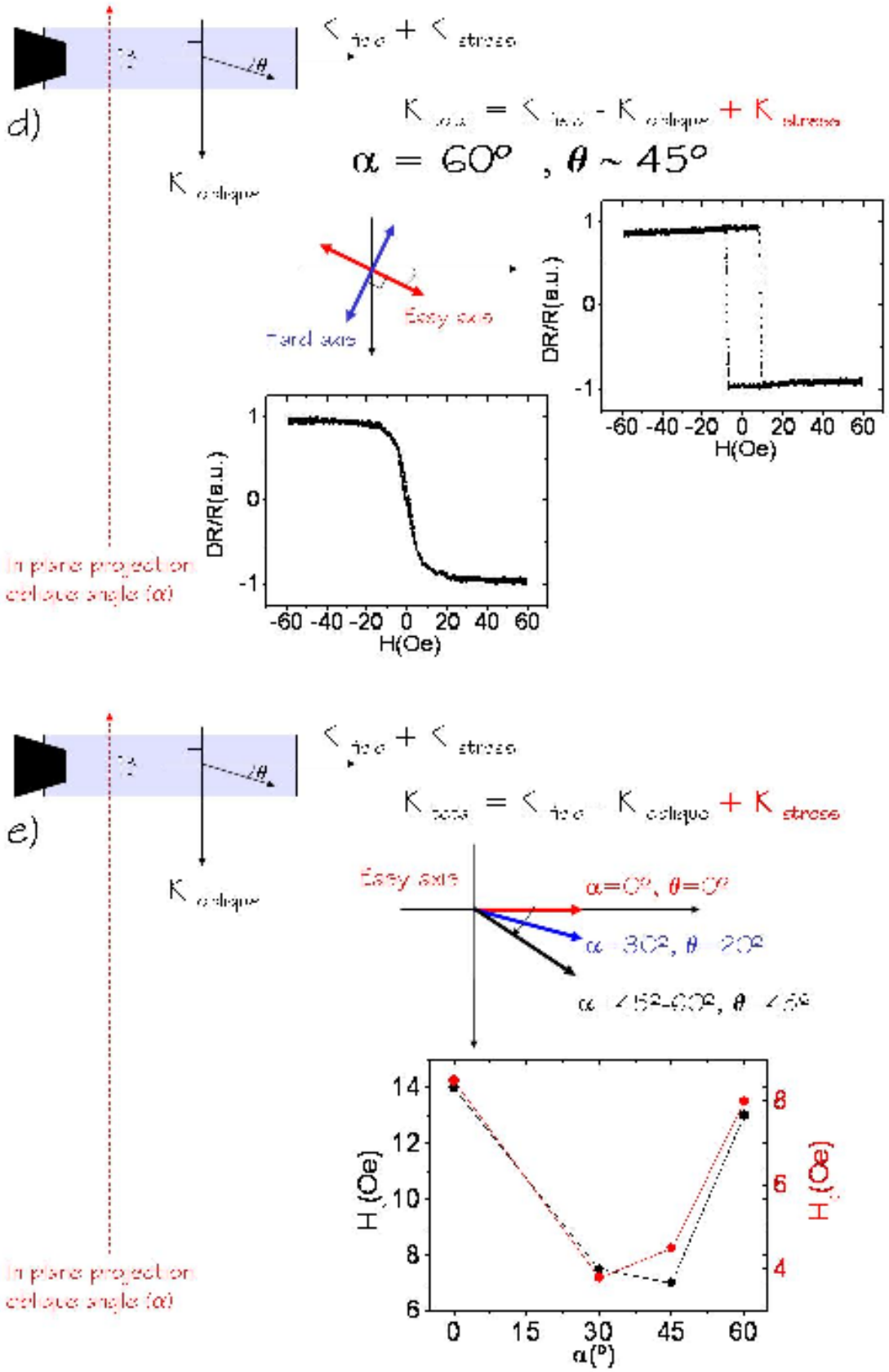

Figure 10 : a)-d) Hard and easy magnetization axis loops and easy axis direction in the case of a thin glass substrate (B) which long edge is parallel to the applied magnetic field and for four different deposition angles (α). e) Anisotropy angle direction (θ), coercive field (H_c) extracted from the easy axis loops and anisotropy field (H_k) extracted from the hard axis loops.

III.3.2.c) Thin glass substrate (C) which long edge is perpendicular to the applied magnetic field.

In this case, the in-plane projection of the oblique incidence angle together with the direction of the *stress induced anisotropy* are perpendicular to the applied magnetic field. The combination of these orthogonal anisotropies gives rise to a total anisotropy that can be expressed as $K_{total} = (K_{induced}) - (K_{stress} + K_{oblique})$. Increasing the angle of deposition, the anisotropy turns perpendicular, increasing the value of the anisotropy field with the angle of deposition as shown in Figure 11, where the B-H hysteresis loops along the hard and easy magnetization axis are shown. This means that *field induced anisotropy* is dominant for lower deposition angles, but as deposition angle increases, there is a change in the uniaxial anisotropy that is attributed to *oblique incidence anisotropy* ($K_{oblique}$) combined with *stress induced anisotropy* (K_{stress}). But, as different from the case of the thin substrate (B), the second effect assists the easy magnetization axis to rotate for higher deposition angles (α). As substrate bending due to the accumulated stress was possible in this case, an anisotropic behaviour of the accumulated stress gives rise to a favourable easy axis direction, in this case parallel to the substrate long edge. The effect of the *stress induced anisotropy* adds to the effect of the *oblique induced anisotropy*.

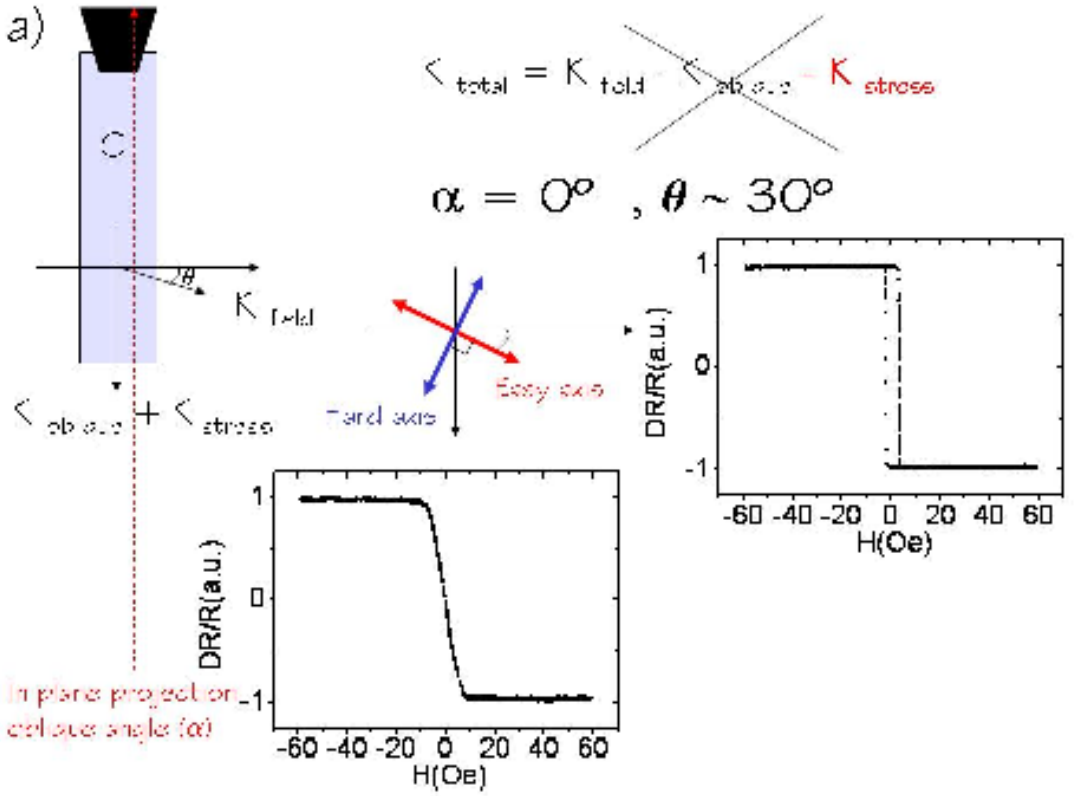
a)
$K_{total} = K_{field} + K_{oblique} + K_{stress}$
$\alpha = 0°$, $\theta \sim 30°$
K_{field}
$K_{oblique} + K_{stress}$
Hard axis
Easy axis
In plane projection of oblique angle (α)
DR/R(a.u.)
H(Oe)
1
0
-1
-60 -40 -20 0 20 40 60

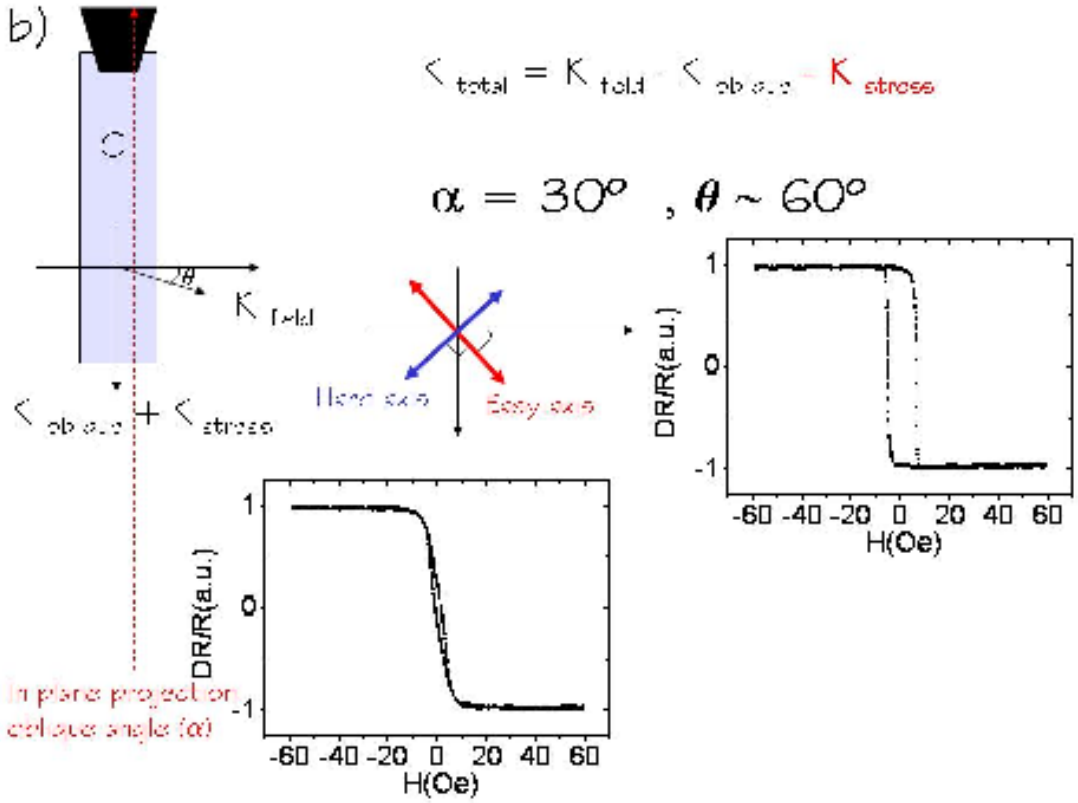
b)
$K_{total} = K_{field} + K_{oblique} + K_{stress}$
$\alpha = 30°$, $\theta \sim 60°$
K_{field}
$K_{oblique} + K_{stress}$
Hard axis
Easy axis
In plane projection of oblique angle (α)
DR/R(a.u.)
H(Oe)
1
0
-1
-60 -40 -20 0 20 40 60

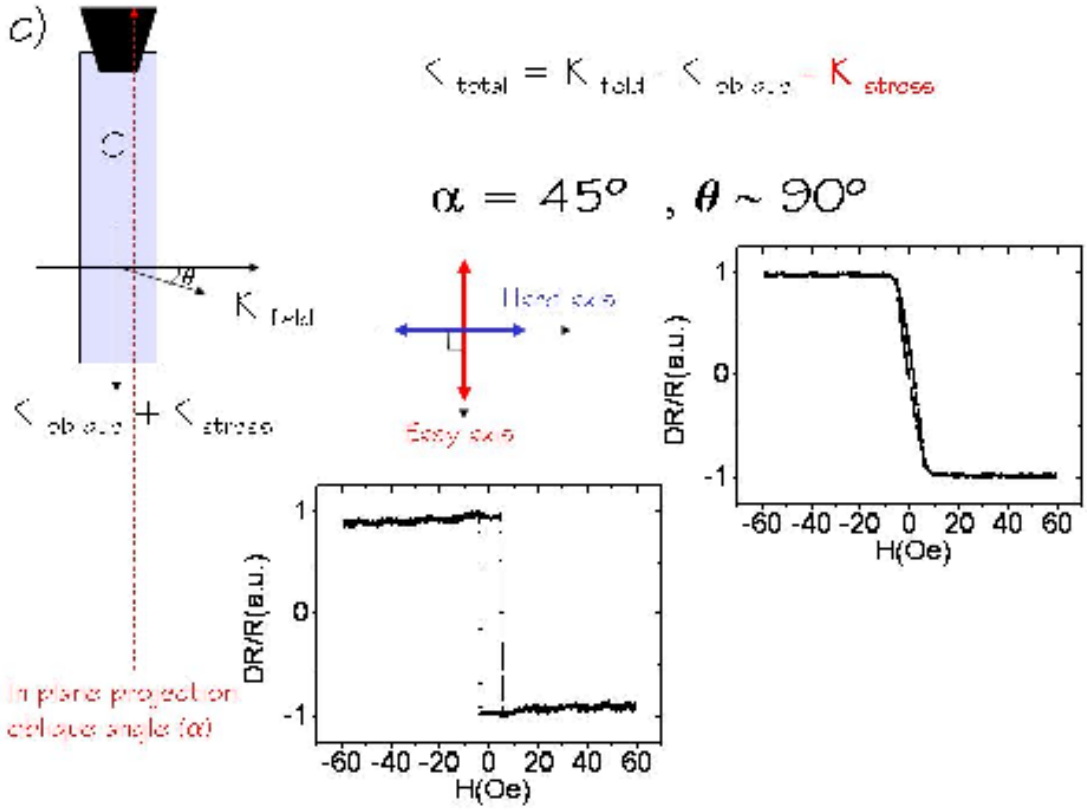
c)
$K_{total} = K_{fold} + K_{shape} + K_{stress}$
$\alpha = 45°$, $\theta \sim 90°$
Hard axis
Easy axis
DR/R(a.u.)
H(Oe)
In plane projection of the wire angle (α)

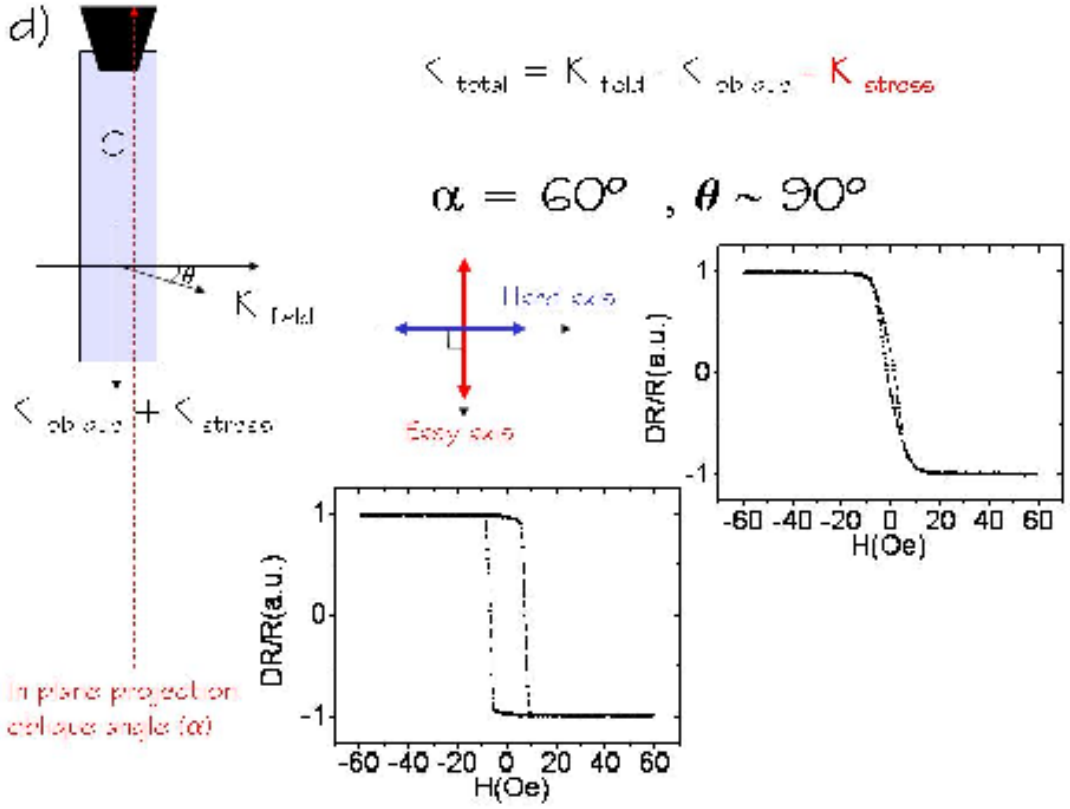
d)
$K_{total} = K_{fold} + K_{shape} + K_{stress}$
$\alpha = 60°$, $\theta \sim 90°$
Hard axis
Easy axis
DR/R(a.u.)
H(Oe)
In plane projection of the wire angle (α)

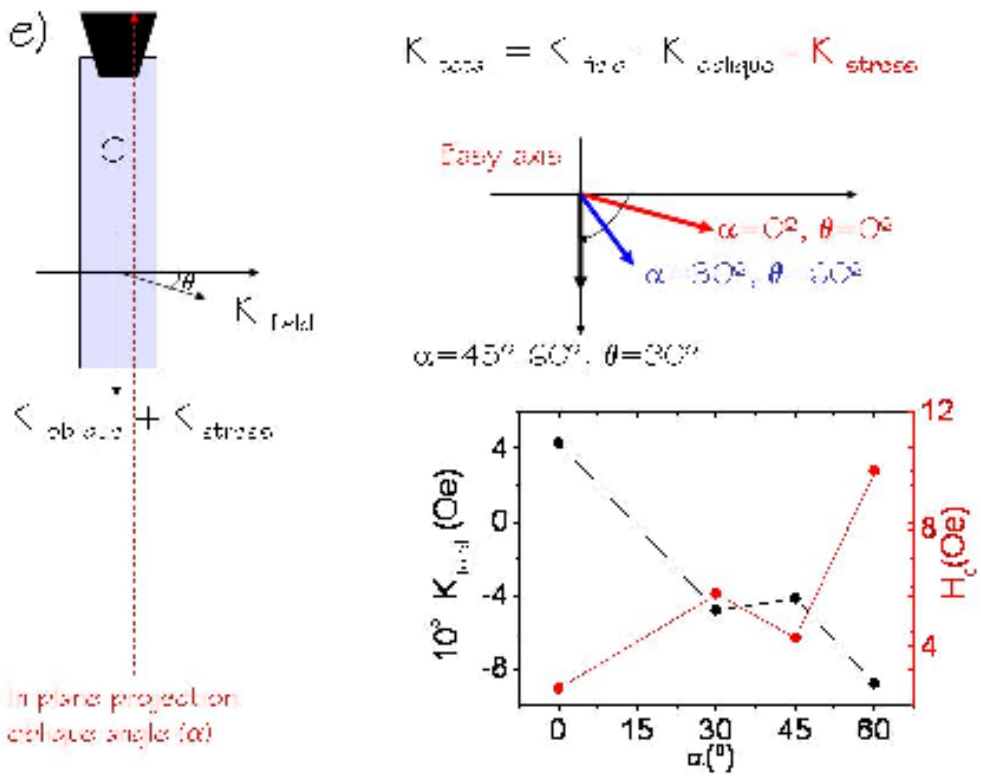

Figure 11: a)-d) Hard and easy magnetization axis loops and easy axis direction in the case of a thin glass substrate (B) which long edge is parallel to the applied magnetic field and for four different deposition angles (α). e) Anisotropy angle direction (θ), coercive field (H_c) extracted from the easy axis loops and anisotropy field (H_k) extracted from the hard axis loops.

III.3.3. Magnetic anisotropy as a function of the target potential.

Amorphous $Fe_{20}B_{20}$ films were grown on thin glass cantilevers with the following deposition parameters: a fixed sputtering pressure ($8 \cdot 10^{-3}$ mbar), a wide range of target potentials [(-0.5 to -2) kV] and 45º angle deposition. These films were used for the study of the accumulated stress as a function of the target potential carried out in Chaper II, Section II.5. It is found that near zero accumulated stress in the deposited films is achieved for a sputtering pressure of $8 \cdot 10^{-3}$ mbar and a target potential of -0.75 kV. The film B-H hysteresis loops along the easy and hard axis directions are shown in Figure 12.a) and 12.b). The anisotropy rotates 90º, as expected from the above arguments. From the technological point of view, there is a well defined uniaxial anisotropy at the optimized deposition parameters of -0.75 kV and $8 \cdot 10^{-3}$ mbar to achieve near zero stress films.

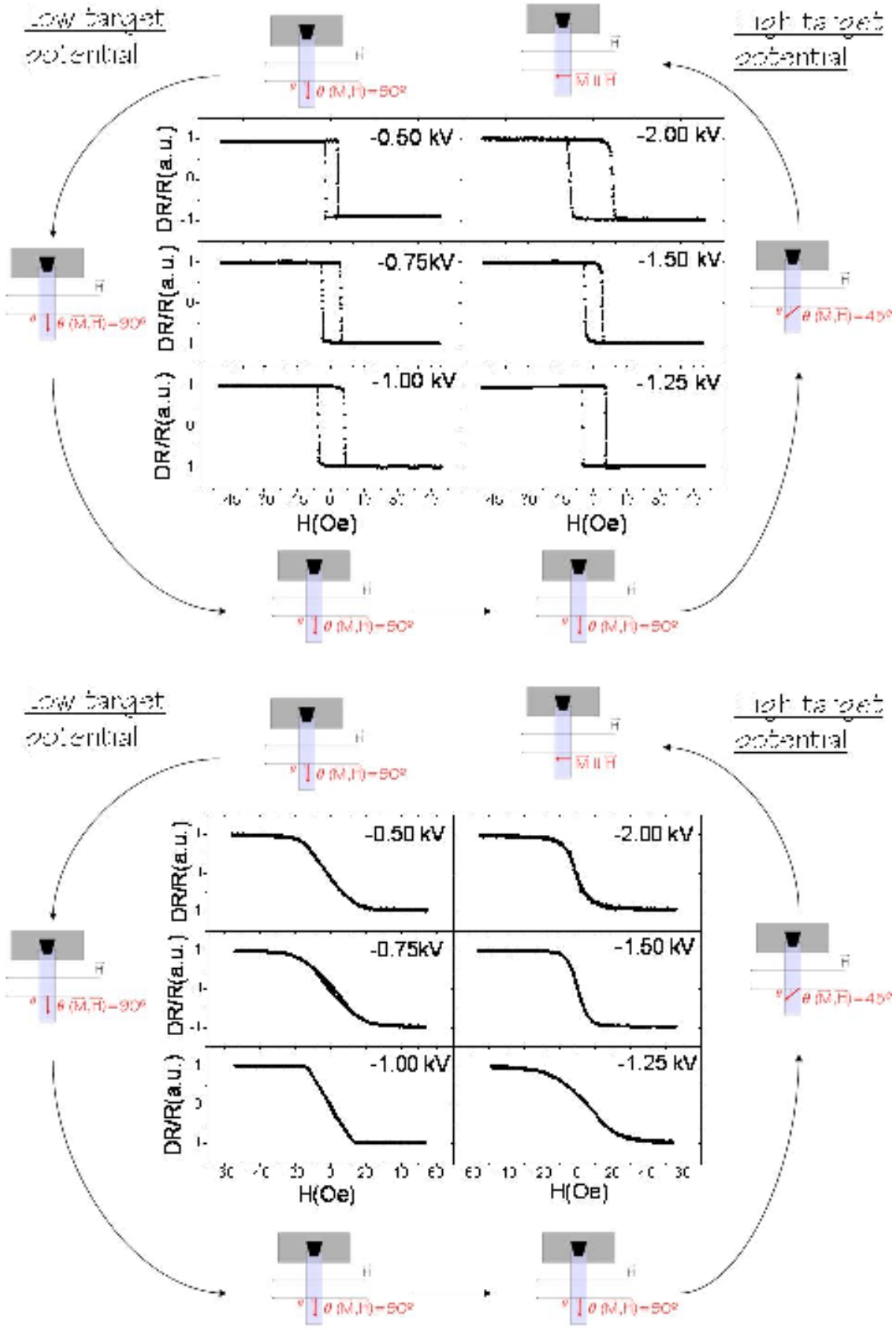

Figure 12 : a) B-H hysteresis loops along the easy magnetization axis for various target potentials. b) B-H hysteresis loops along the hard magnetization axis for various target potentials.

III.4. Conclusions.

In this chapter, it has been shown that amorphous sputtered $Fe_{80}B_{20}$ thin films display a net in-plane uniaxial anisotropy that can be tuned depending on substrate geometry and deposition conditions. The film magnetic anisotropy is studied as a function of the deposition parameters, for a wide range of sputtering pressures [(2 - 25) • 10^{-3} mbar] and target potentials [(-0.5 to -2) kV]. This film uniaxial magnetic anisotropy is a balance of three contributions : *stress induced*, *field induced* and *oblique incidence anisotropy*. This balance is determined by the film deposition parameters and substrate shape/thickness. The resulting magnetic properties of amorphous $Fe_{80}B_{20}$ thin films are correlated with the measured stress studied in Chapter II. From the technological point of view, an uniaxial anisotropy is defined at the right deposition parameters to achieve near zero stress films. A fine control of the hard axis direction is essential to maximize the magnetostrictive strains and consequently the use of amorphous $Fe_{80}B_{20}$ thin films in micromechanical actuators, as for example AFM cantilevers.

References.

[1] Y. Lu and A. Nathan, '*Metglass thin flm with as-deposited domain alignment for smart sensors and actuators* ', Appl. Phys.Lett., **70**, 526 (1997).

[2] T. Fukuda, H. Hosokai, H. Ohyama, H. Hashimoto and. F. Arai, *'Giant magnetostrictive alloy (GMA) applications to micro mobile robot as a micro actuator without power supply cables'*, IEEE MEMS91, 210 (1990)

[3] K. Honda and S. Kaya, Sci. Repts. Tohoku Imp. Univ., **15**, 721 (1926).

[4] G. Armelles, J. L. Costa-Krämer, J. I. Martin J. V. Anguita and J. L. Vicent. *'Anisotropy measurements in mesoscopic magnets by magneto-optical torque*', Appl. Phys. Lett., **77**, 2039 (2000).

[5] Y. Shimada, T. Hasegawa and H. Kojima, *'Sputtering of Fe-Co-B amorphous films with soft magnetic properties',* IEEE Trans. Magn., **MAG-17(2)**, 1199, (1981).

[6] H. J. Leamy and A. G. Dirks, *'Microstructure and magnetism in amorphous rare earth transition metal thin films. I. Microstructure*', J. Appl. Phys., **49 (6)**, 3430 (1978).

[7] D. García, F. J. Castaño, C. Prados, M. Vazquez and F. Castaño, *'Crossed anisotropies in FeB/CoSiB bilayers induced by the bowed-substrate sputtering technique',* Appl. Phys. Lett., **74**, 105 (1999).

[8] B. D. Cullity, '*Introduction to Magnetic Materials'*, Addison-Wesley, Reading, MA, p. 274 (1972).

[9] E. Luborsky, '*Amorphous Metallic Alloys',* Butterworths, 308 (1984).

[10] E. Luborsky, '*Amorphous Metallic Alloys',* Butterworths, 257 (1984).

[11] J. C. Slonczewski, *'Magnetic Annealing'*, edited by G. Rado and H. Suhl Academic, New York, **1**, 205 (1963).

[12] K. Dahmen, S. Lehwald and H. Ibach, *'Bending of crystalline plates under the influence of surface stress. A finite element analysis'*, Surf. Sci., **446** 161 (2000).

[13] B. D. Cullity, '*Introduction to magnetic materials'* Addison-Wesley, Reading, 330 (1971).

[14] T. G. Knorr and R. W. Hoffman, *'Dependence of Geometric Magnetic Anisotropy in Thin Iron Films'*, Phys. Rev., **113**, 1039 (1959).

[15] D. O. Smith, *'Anisotropy in Permalloy Films'* , J. Appl. Phys., **30**, 264S (1959).

[16] D. O. Smith, M. S. Cohen, and G. P. Weiss, J. Appl. Phys., **31**, 1755 (1960).

[17] F. G. West, *'Oblique-Incidence Anisotropy in Evaporated Permalloy Films'*, J. Appl. Phys., **35**, 1827 (1964).

[18] A. G. Dirks and H. J. Leamy, *'Columnar microstructure in vapor-deposited* thin films*'* , Thin Solid Films, **47**, 219 (1977).

[19] M. Suzuki and Y. Taga, *'Numerical study of the effective surface area of obliquely deposited thin films'* , J. Appl. Phys., **90**, 5599 (2001).

[20] T. J. Klemmer, K. A. Ellis, L. H. Chen, B. van Dover, and S. Jin, *'Ultrahigh frequency permeability of sputtered Fe-Co-B thin films'*, J. Appl. Phys., **87**, 830 (2000).

IV

Effect of sputtering in the presence of nitrogen on the structural and magnetic properties of Fe-B-N thin films.

IV.1. Introduction. 87

IV.2. Experimental details. 88

IV.3. Structural properties of Fe-B-N films. 88

IV.3.1. Nitrogen concentration determination. 88

IV.3.2. Crystallinity. 91

IV.3.3. Chemical environment of Fe, N y B atoms. 91

IV.4. Magnetic properties of Fe-B-N thin films. 94

IV.4.1. Saturation magnetization (M_S) 94

IV.4.2. Anisotropy Constant (K_u) 95

IV.4.3. Saturation Magnetostriction coefficient (λ_S) 96

IV.5. Evaluation of the corrosion resistance in liquid environment. 98

IV.6. Conclusions. 99

References. 99

IV.1. Introduction.

It is known that the addition of small amounts of nitrogen [1,2], oxygen [3,4] or carbon [5] to magnetic amorphous alloys can increase its crystallization and Curie temperatures, saturation magnetization M_s, corrosion resistance, electrical resistivity and high frequency permeability. These enhanced properties made these materials very interesting in the 90's for their use as core materials of magnetic heads, where materials with high saturation magnetization, higher frequency operation combined with very low eddy currents were required. In this thesis, it is proposed to make use of the excellent properties of these alloys for magnetostrictive modulation of micro-mechanical systems (MEMS) in liquid environment, where corrosion of the magnetic films usually limits their operation. In this chapter, the effect of sputtering in the presence of nitrogen on the structure, magnetic properties and corrosion resistance of amorphous Fe-B thin films is analyzed.

Some of these enhanced properties are related with the fact that these films usually çshow a very fine two phase hetero-amorphous or nano-granular structure. This structure consist of ferromagnetic metal particles of nanometer size embedded in a ceramic matrix, as shown in Figure 1. A extensive study was done in nano-granular soft magnetic (Fe, Co, Ni) - (Al, Si, Zr, Mg, rare earth) - (oxide or nitride) films deposited by reactive sputtering [6,7].

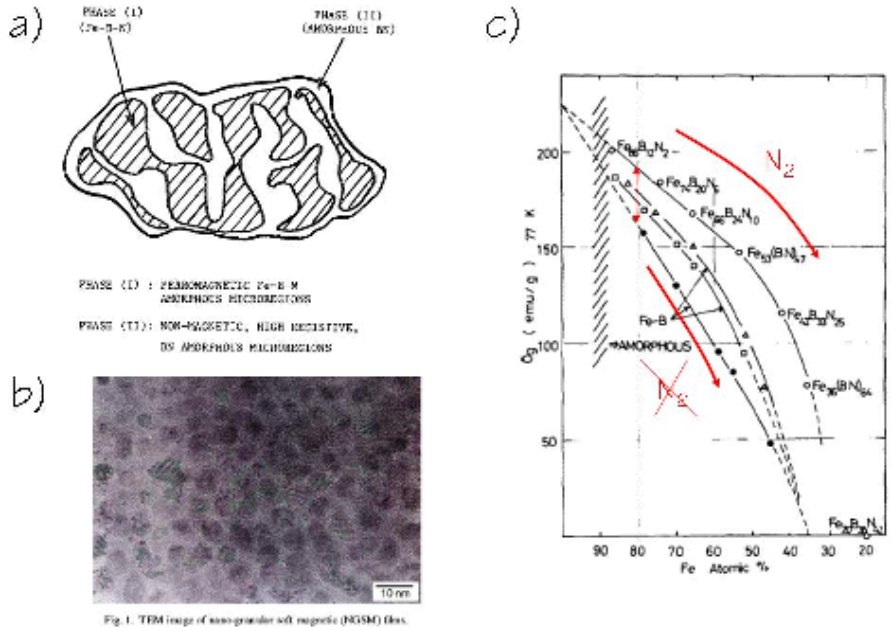

Figure 1 : a) Schematic diagram showing the arrangement of the two phases, a metallic phase embedded in a ceramic matrix present in nano-granular films. b) TEM image of nano-granular soft magnetic film. c) Dependence of saturation magnetization on iron content in Fe-B-N and Fe-B amorphous films [2]. It is show how the presence of nitrogen increases the value of the saturation magnetization of the film.

In the case of sputtered amorphous Fe-B-N films, it was found that an amorphous ferromagnetic phase (Fe-B-N) was embedded in a non magnetic and high resistive (B-N)

phase, as observed by Transmission Electron Microscopy (TEM) and infrared spectra [2]. It was shown that the presence of nitrogen increases the saturation magnetization M_s value of Fe-B-N films, as compared with Fe-B films with the same iron content. This is shown in Figure 1.c). The reason for this increase is still unclear. This is probably due to the compositional change induced by the introduction of nitrogen, that varies the chemical environment of the iron atoms [8,9].

In this thesis, it was found that higher values of magnetostriction constant combined with very large values of the anisotropy constant are achieved with a moderate nitrogen addition. Finally, the corrosion resistance is studied as a function of the time for films immersed in liquid environment. It was found that film without nitrogen addition were completely dissolved in several minutes, but for a moderate addition of nitrogen during deposition, 2% of nitrogen partial pressure, the properties of the film were stable even for a year.

IV.2. Experimental details.

Amorphous Fe-B-N are sputtered in the presence of a mixture of argon and nitrogen gas, for different nitrogen partial pressures. It is observed that nitrogen incorporates into the film preserving its amorphous structure and modifying its magnetic properties. The amount of nitrogen that incorporates into the amorphous structure is determined to scale linearly with the nitrogen gas partial pressure during film growth. Fe-B-N amorphous films have been sputtered in the presence of an Ar + N_2 atmosphere, both on glass and on silicon <100> substrates. The target potential was kept constant at –2.0 kV, while the total gas pressure was kept constant at $8.0 \cdot 10^{-3}$ mbar, varying the nitrogen partial pressure from 2% ($1.6 \cdot 10^{-4}$ mbar) to 7% ($5.4 \cdot 10^{-4}$ mbar). In addition, a thin film with 0% nitrogen was grown for comparison. The deposition rates were of the order of 1 Å/s, decreasing slightly and continuously as the partial nitrogen pressure increased. All deposited films have a thickness of 30 nm as confirmed by profilometer and AFM techniques.

IV.3. Structural properties of Fe-B-N films.

IV.3.1. Nitrogen concentration determination.

Non-Rutherford backscattering spectroscopy (Non-RBS) was used to determine the chemical composition and areal densities of the sputtered films as a function of the nitrogen pressure in the chamber during deposition. This technique consist of measuring the number and energy of ions which are back-scattered after colliding with the atoms of the target in the region of a film at which the beam has been targeted. This technique allows atomic masses and determination of the elemental concentration and distribution of target atoms with depth resolution. The advantage of using non-RBS in comparison to the traditional use of RBS for

stoichiometry determination is mainly that it allows an improved resolution and sensitivity of light elements detection. The non-RBS regime is achieved by tuning the beam energy to specific values in which the ion-atom cross section is non-Rutherford.

In our particular case, non-RBS measurements were performed using a He^+ beam at the resonance energy 3.7 MeV in a high vacuum chamber which is connected to a 5 MV Tandetron accelerator [10,11] at the *Centro de Microanálisis de Materiales (CMAM/UAM)* [12]. At this energy the nuclear reaction channel $^{14}N(\alpha,p_0)^{17}O$ is open. By coincidence, the energy of the emitted protons is nearly equal to that of the α particles back-scattered from the nitrogen and at the resonance energy the proton and α particle yield cannot be separated in our measurements. For this reason the Non-RBS spectra were measured under the same conditions by placing a 13 μm Mylar foil in front of the detector which prevents the α particles to arrive at the detector and allows us to estimate the contribution of the scattered protons to the nitrogen peak [13]. The backscattered ions were detected by a standard Si-barrier detector located at an angle of 165º to the beam direction [14].

A typical Non-RBS spectrum measured with a He^+ beam at an energy of 3.7 MeV is shown in Figure 2. That spectrum illustrates that the sputtered film consists of a Fe-B-N layer on a Si substrate. The Fe and N peaks are clearly visible while the B peak is quite small due to the experimental configuration. The atomic percentage of Fe and N in the film is estimated by comparing experimental and simulated spectra. For the simulations the commercial computer code SIMNRA [15] was used. The atomic percentage of B in the film is deduced after adjusting the Fe and N peaks.

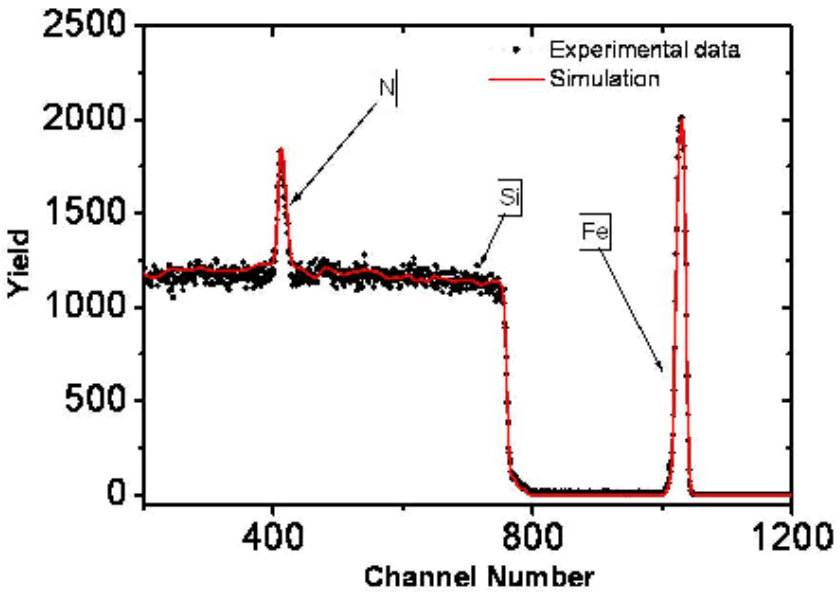

Figure 2 : Typical Non RBS spectrum of a Fe-B-N film taken at an energy of 3.7 MeV with a He+ beam. The experimental (broad black line) and the simulated (red line).

The stoichiometry and areal density of the films are estimated as a function of the partial pressure of nitrogen in the chamber during film deposition, as shown in Table 1. As said before, growth rate slightly decreases with increasing nitrogen content. This behaviour has been also observed in some other metal-nitrides [16,17]. By tuning the deposition time, all deposited films have the same thickness (30nm), as confirmed by profilometer and AFM techniques. Discount the possibility that the variation of the thickness measured by Non-RBS is due to a variation of the thin films density as nitrogen is incorporated, as variations of either the density or thickness are indistinguishable.

N_2 partial pressure	N (at %)	Stoichiometry	Areal density by Non-RBS (x 10^{15} at/cm^2)
0	0	$Fe_{80}B_{20}$	555
2	7	$Fe_{74}B_{19}N_7$	555
3	9	$Fe_{73}B_{18}N_9$	555
4	10	$Fe_{72}B_{18}N_{10}$	550
6	16	$Fe_{67}B_{17}N_{16}$	548
7	19	$Fe_{65}B_{16}N_{19}$	535

Table 1. Brief overview of the partial pressure in percentage on nitrogen in the chamber during growth (N_2 partial pressure), and of the atomic percentage of nitrogen in the thin films N (at %), stoichiometry and thickness of the thin films as estimated by Non-RBS.

Non-RBS data show that under this deposition conditions, the amount of nitrogen that incorporates into the amorphous structure linearly scales with the nitrogen partial pressure in the chamber during film deposition, as shown in Figure 3.

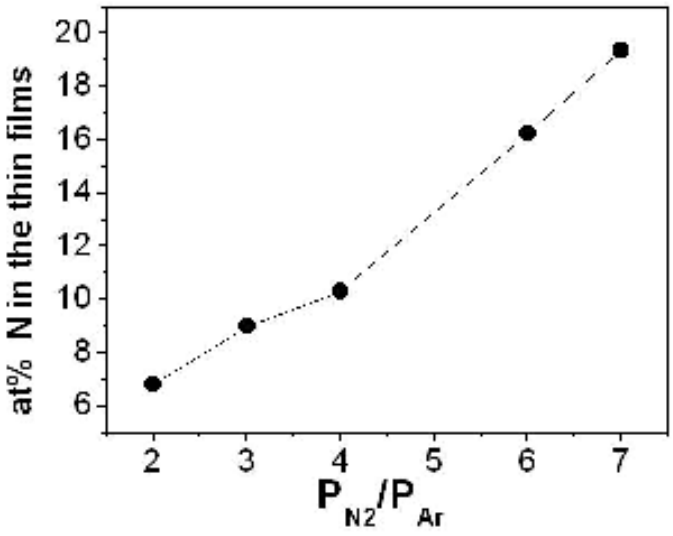

Figure 3 : Atomic percentage of nitrogen incorporated in the Fe-B-N thin film, as calculated from the non-RBS measurements, as a function of P_{N2}/P_{Ar} in the chamber during the sputtering process.

IV.3.2. Crystallinity.

The amorphous character has been confirmed by X-ray diffraction (XRD) measurements. No sharp diffraction peak is observed for thin films whatever the nitrogen concentration of the film. Thus, the layers can be termed X-ray amorphous for all nitrogen concentrations. The X-ray diffractograms patterns for Fe-B-N films with different nitrogen concentration are shown in Figure 4.

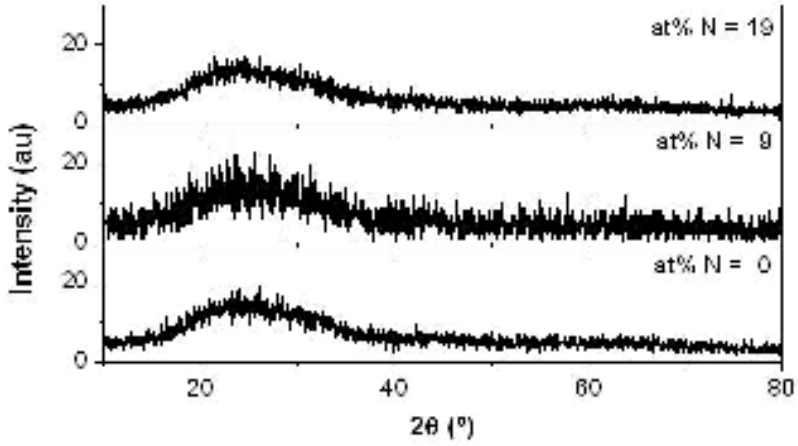

Figure 4 : X-ray diffractograms for 0, 9 and 19 at% of nitrogen content. No sharp diffraction peak is observed at any angle.

IV.3.3. Chemical environment of Fe, N y B atoms.

In order to obtain information about the chemical environment of the iron, boron and nitrogen atoms, X-ray photoemission spectroscopy (XPS) experiments were performed for Fe-B-N thin films with different nitrogen concentration at the *Servicio de Nanotecnología y Análisis de superficies de la Universidad de Vigo* [*18*]. The analysis was done using an VG Escalab 250 iXL ESCA instrument (VG Scientific), equipped with aluminium $K_{\alpha 1,2}$ monochromatic radiation at 1486.92 eV X-ray source. The XPS measurements were carried out using monochromatic Al-K_α radiation ($h\nu$=1486.92 eV). Photoelectrons were collected at a take off angle of 90º relative to the substrate surface. The measurement was done in a Constant Analyser Energy (CAE) mode with a 100.0 eV pass energy for survey spectra and 20.0 eV pass energy for high resolution spectra. Charge referencing was done by setting the lower binding energy C 1s photo-peak at 285.0 eV C1s hydrocarbon peak [19]. The spectra fitting is based on “Chi-squared” algorithm used to determine the goodness of a peak fit.

Fe-B-N thin films exposed to air showed C1s, O 1s and N 1s peaks, but after sputtering of the film surface with an Ar^+ ion gun for 300 seconds, C 1s peak vanishes and O 1s peaks

decreases dramatically. This was monitored by narrow-scan XPS measurements between successive periods of ion bombardment until the amount of carbon detected was less than 5%. An extensive study was developed on the Fe-B-N film with an overall composition of nitrogen of 9%, and the time required to remove totally the contaminants and the oxide layer was used for reference on the rest of films. A depth profile was done to determine the time (Ar+ sputtering seconds) required to remove the oxide layer, resulting in 300 sec / 9 levels, as shown in Figure 5. The contaminants of the surface were mainly C and O. Most of the carbon was removed, but the peak position of C 1s from the small amount of carbon left in the surface shifted from 285.0 eV to 283.0 eV. This could indicate the formation of a low quantity iron carbide.

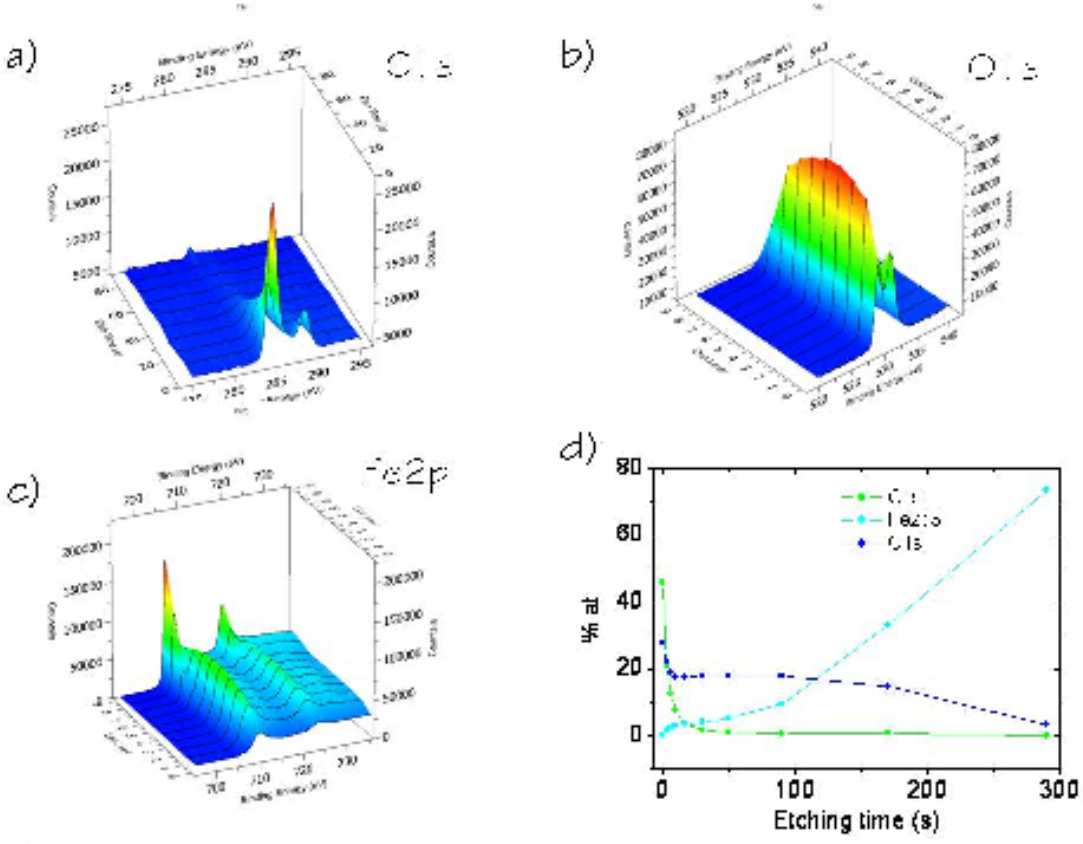

Figure 5 : a)-d) Depth profile for carbon (C), oxygen (O) and iron (Fe) atoms that are present in the Fe-B-N film. 9 levels of Ar+ etching with total etching time of 300seconds were used.

Once the contamination layer is removed, the chemical environment of the iron, boron and nitrogen atoms can be studied. Figure 6 shows the XPS spectra of B1s and Fe2p after Ar^+ sputtering. In the first case, this figure shows two peaks clearly corresponding to different chemical states for boron. One peak is located at a binding energy (BE) around 187.3 - 187.4 eV which illustrates a very good correspondence to the BE assigned to B - Fe bonding reported for the same compound $Fe_{80}B_{20}$ [19]. The second and broader peak of B1s is found at BE of 190.0 - 192.0 eV. This broad peak can be fitted by two peaks. One due to a B-N bonding at 190.2 eV and a second one at BE = 192.0 eV that can be related to a B-O bond from B_2O_3. This B-N and B-O bonds for the film at 0% nitrogen results probably from a non-complete removal of

surface contamination with the Ar^+ bombardment. For films with nitrogen content > 0, the chemical environment of the B 1s changes. The peak at 190.2 eV increases while compared with the one at 187.3 eV. This means that nitrogen incorporates into the films reacting with the B forming boron nitride reducing the amount of B associated with iron. This is also confirmed by the presence of a N-B peak at a BE 398.2 eV that is observed for the 9% and 19% nitrogen flow rates.

The BE of $Fe2p_{3/2}$ and $Fe2p_{1/2}$ is around 706.5 eV and 719.7 eV, respectively close to the values reported for a $Fe_{80}B_{20}$ (706.9 eV and 719.9 eV, respectively). Neither changes in the position nor shoulders in the peak are detected upon nitridation, which means that the chemical environment of Fe seems to be unalterable. This is a very interesting result because in general when iron and its alloys are in the presence of nitrogen they form nitrides [20]. This is another proof that nitrogen does not bond chemically to Fe but to B of the film. This can be understood from a thermodynamic point of view since the energy of formation of B-N compounds is more negative (more stable) than that for Fe-N compounds [21]. On the other hand, the fact that no diffraction peak is found in XRD pattern upon nitridation (Figure 4) means that the phases present in the films are amorphous, or too small to be detected, nanocrystalline presumably.

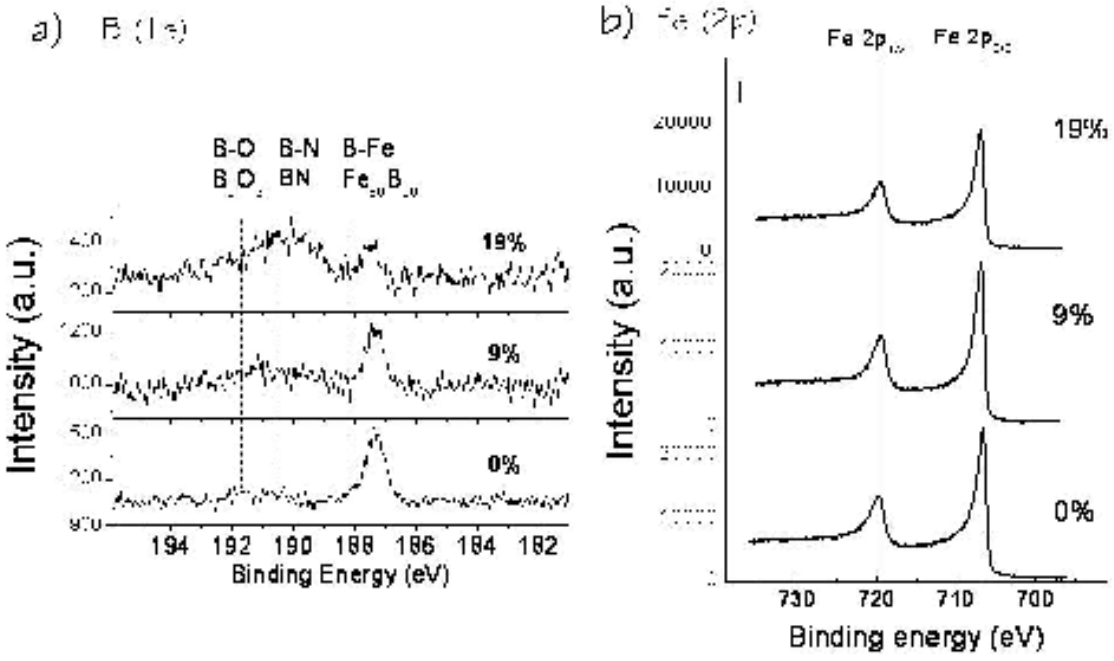

Figure 6 : XPS spectra on the a) B1s and b) Fe2p core levels for a Fe-B-N films with 0, 9 and 19 at% nitrogen concentration.

As reported by other authors [22], Mossbauer and Transmission Electron Microscope (TEM) studies of sputtered Fe-B-N films also indicate the formation of a granular solid, where a

continuous network of interconnected amorphous Fe-B alloy particles are embedded in a amorphous BN matrix.

IV.4. Magnetic properties of Fe-B-N thin films.

IV.4.1. Saturation magnetization (M_S).

Magnetic characterization of the Fe-B-N thin films was carried out by means of a superconducting quantum interference device (SQUID) from Quantum Design model MPMS XL at the *Instituto de Magnetismo Aplicado "Salvador Velayos"* [23]. The value of saturation magnetization (M_s) was calculated from these measurements. The obtained B-H 1hysteresis loops for a Fe-B reference film and for Fe-B-N films with different nitrogen concentration, ranging from 0% to 14%, are shown in Figure 7. The saturation magnetization (M_s) for Fe-B-N films is shown to depend on the nitrogen concentration. At the low nitrogen concentration range (Fe-B)-N_x (x < 9 at% N) the saturation magnetization increases as compared to that for the Fe-B reference film. The highest enhancement, up to 20%, is observed for Fe-B-N films with 9 at % of nitrogen. For films with nitrogen content higher than 9 at%, *Ms* drastically decreases as compared to that for the reference film, being up to 30% smaller for a film with a 14 at% of nitrogen than for the reference film. The saturation magnetization for the Fe-B reference film was measured to be 1058 emu·cm $^{-3}$ (1.33 T in the S.I.), which is in good agreement with values previously reported for films with the same stoichiometry [24].

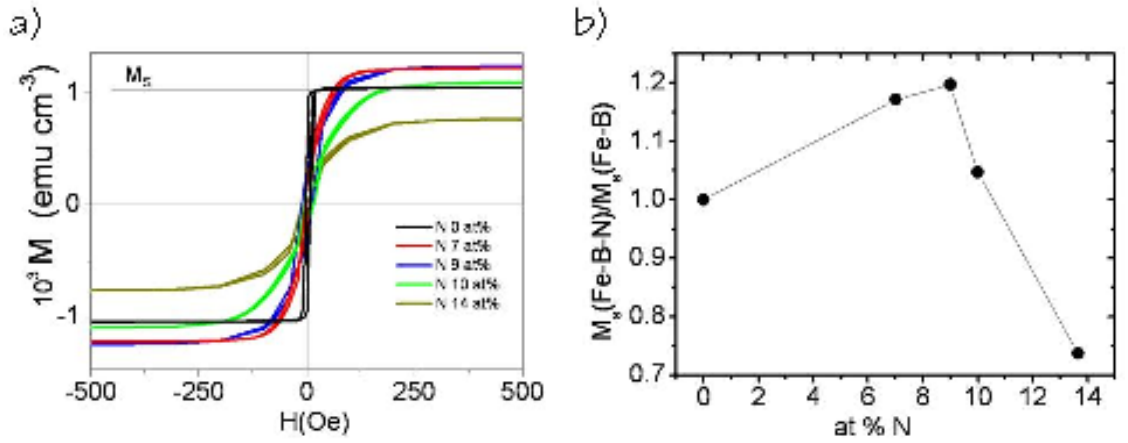

Figure 7 : a) B-H hoysteresis loops of Fe-B-N alloys with different atomic percentage of nitrogen measured by SQUID magnetometry at 300 K. b) Dependence of Ms on atomic percentage of nitrogen for Fe-B-N films. The value of the Ms is normalized to the reference film with 0% nitrogen content.

The increase of the saturation magnetization M_s value was also reported by other authors [2], comparing Fe-B-N with Fe-B amorphous films with the same iron content. The reason for this increase is still unclear. This is probably due to the compositional change induced by nitrogen varies the chemical environment of the iron atoms. For films with nitrogen

concentration larger than 9%, M_s decreases as the nitrogen concentration increases, as expected.

IV.4.2. Anisotropy Constant (K_u).

All the Fe-B-N thin films show an uniaxial anisotropy induced by the applied magnetic field used to confine the plasma, with an easy axis that points parallel to the field. The value of the anisotropy constant K_u is calculated from the anisotropy field H_k estimated from MOKE data and the saturation magnetization M_s as measured by SQUID using the next equation:

$$K_u = \frac{1}{2} M_S \cdot H_K \qquad (1)$$

The hysteresis loops measured in the hard axis are shown in Figure 8. For nitrogen concentrations lower than 10%, the B-H hysteresis loops are closed, signifying a coherent rotation of the magnetization. The value of the coercive field in the easy axis direction varies between 2 and 5 Oe, as seen in the inset of the Figure 8. For nitrogen concentrations larger than 10%, the hysteresis loops opens, while the coercive field increases with increasing nitrogen content up to 20%. Above that value of nitrogen concentration, no magnetic signal is measured by MOKE.

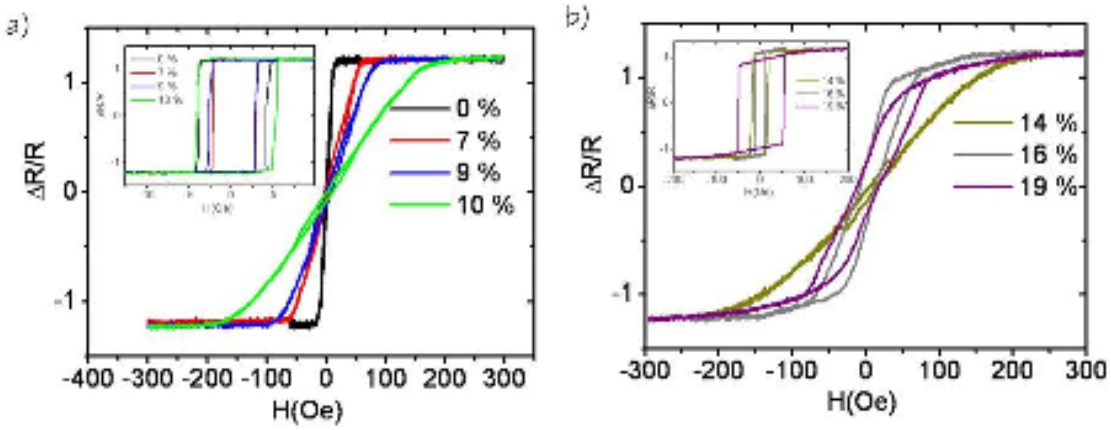

Figure 8 : a) Hard axis hysteresis loops corresponding to Fe-B-N thin films with 0%, 7%, 9% and 10% nitrogen concentration. The easy axis hysteresis loops are shown in the inset. b) Hard axis hysteresis loops corresponding to Fe80B20-N thin films with 14%, 16% and 19% nitrogen concentration.

For nitrogen concentrations lower than 10%, the value of the anisotropy constant increases drastically when increasing the atomic percentage of nitrogen in the Fe-B-N films. For the reference $Fe_{80}B_{20}$ film, the calculated value was $6.3 \cdot 10^3$ erg/cm^3, reaching a value of $8.2 \cdot 10^4$ erg/cm^3 for a thin film with a 10% of nitrogen incorporated. For higher nitrogen concentrations, the value of the anisotropy constant remains constant ($8.2 \cdot 10^4$ erg/cm^3). The values of the anisotropy field H_k and the anisotropy constant K_u as a function of the nitrogen content are shown in Figure 9.

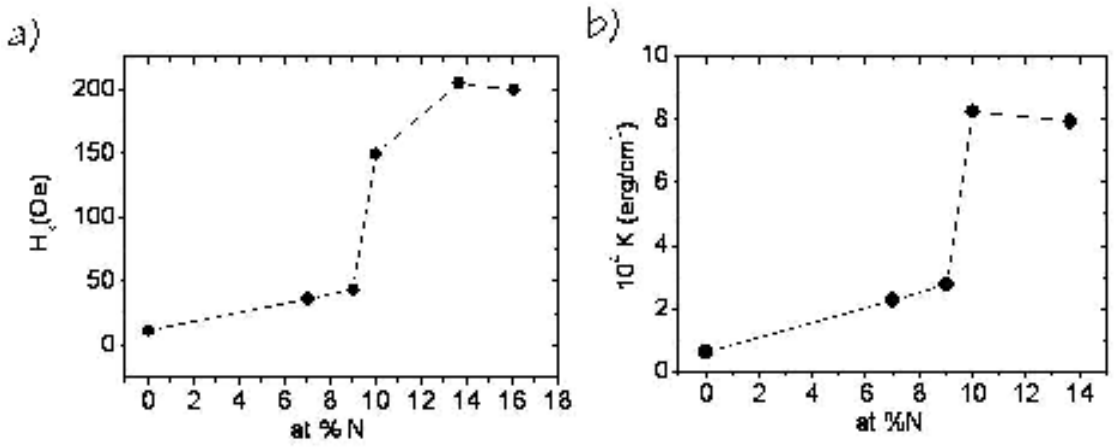

Figure 9 : a) Anisotropy field H_k and b) anisotropy constant (K_u) values as a function of the at% of nitrogen for Fe-B-N films.

The measured uniaxial magnetic anisotropy is a consequence of the directional ordering induced by the applied magnetic field during deposition [25]. As shown in Figure 9, the value of the film anisotropy constant increases with the presence of nitrogen. Similar results were reported by other authors in hetero-amorphous films that consist on $(Fe\text{-}Co)_{1-x}(B_{1-y}\text{-}C_y)_x$ [26]. They measured larger values of the anisotropy field with C addition, whose values disagree the Stomer-Wohlfarth model. They found a composition dependence of the magnetic anisotropy together with an extra directional ordering of the two phases present in the film ((Fe-Co) and (B-C)), what increases the value of the anisotropy constant. In the case of Fe-B-N films, the increase of the directional order with nitrogen addition is still unclear.

IV.4.3. Saturation Magnetostriction coefficient (λ_S).

Fe-B-N thin films were deposited onto thin glass substrates with rectangular cantilever geometry for the measurement of the saturation magnetostriction (λ_S), as explained in Chapter I. Two different measurements were made for films with various nitrogen concentrations. Firstly, an alternating magnetic field was applied parallel to the hard axis direction to measure the evolution of λ as a function of the applied magnetic field. As shown in Figure 10, the shape and value of the anisotropy field H_k is consistent with the magnetization process measured by transversal MOKE. After that, a circular in-plane magnetic field is applied to the glass substrates, to measure the value of the saturation magnetostriction constant.

The dependence of λ_S for the Fe-B-N films on the atomic percentage of nitrogen is shown on Figure 10. Notably, and similarly to what is observed in the evolution of M_s versus the nitrogen content in Figure 7, an initial increase of the saturation magnetostriction with increasing atomic percentage of nitrogen is observed when the nitrogen concentration is lower than ~7 at% N, followed by a slow gradual decrease as the atomic percentage of nitrogen increases further.

The measured value for the saturation magnetostriction constant of the $Fe_{80}B_{20}$ reference film is $25 \cdot 10^{-6}$ in very good agreement to $32 \cdot 10^{-6}$, which is the value reported in the literature [27].

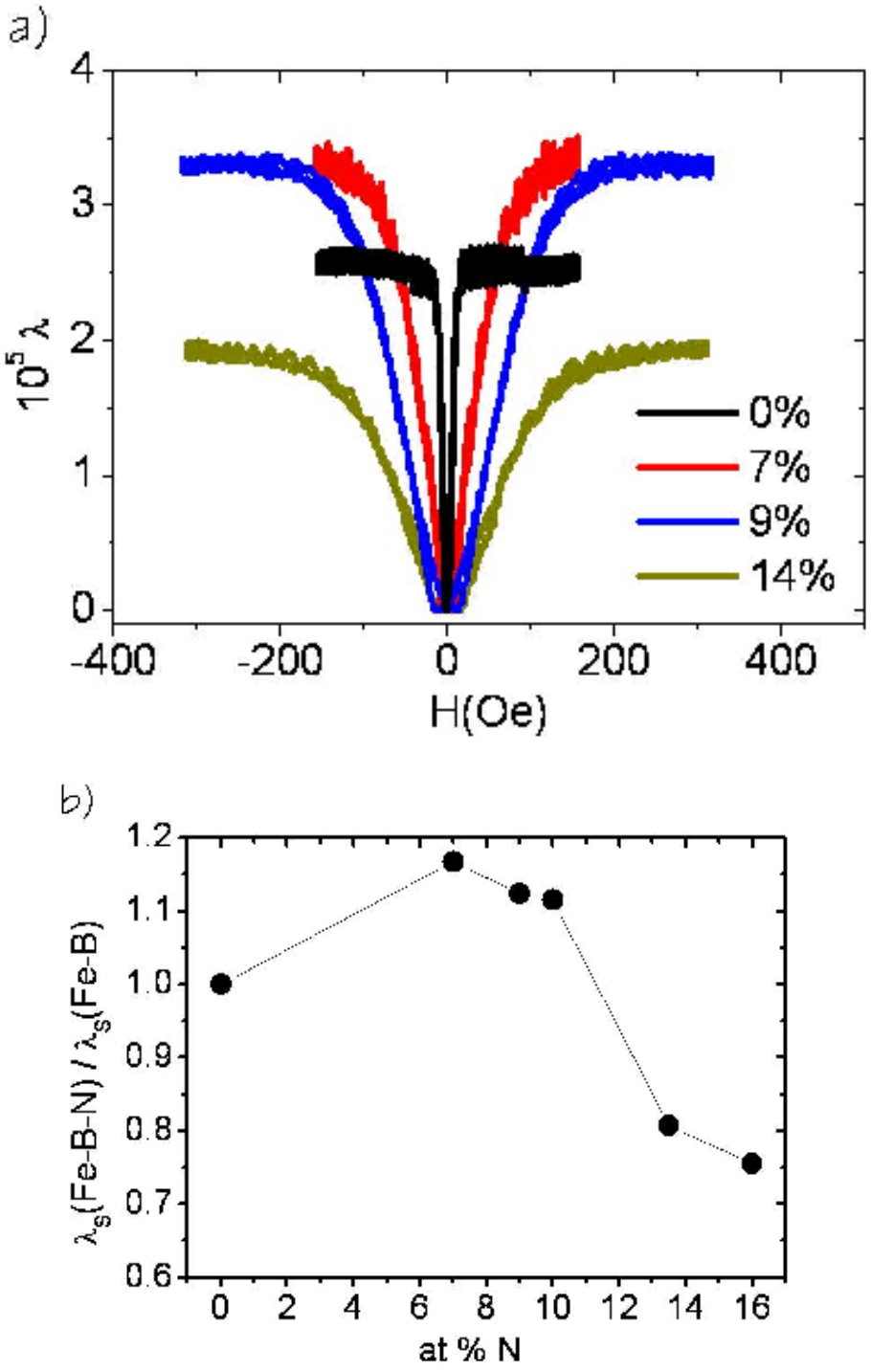

Figure 10 : a) Magnetostriction evolution as a function of the applied magnetic field for different nitrogen concentrations. b) Saturation magnetostriction constant as a function of at% of nitrogen in the film for Fe-B-N amorphous films. The value of the λs is normalized to the reference film with 0% nitrogen content

This unusual increase of the magnetostriction constant for moderate nitrogen incorporation was also found by other authors in hetero-amorphous films that consist on $(Fe\text{-}Co)_{1-x}(B_{1-y}\text{-}C_y)_x$ [26]. They also found an increase in the magnetostriction constant by increasing the carbon concentration, i.e. decreasing the composition of the transition metal. Until now, no explanation of this was found. For films with nitrogen concentration larger than 9%, M_s decreases as the nitrogen concentration increases, as expected.

IV.5. Evaluation of the corrosion resistance in liquid environment.

One of the most important properties that nano-granular films show is the improvement of its corrosion resistance [28, 29]. For technological applications as for example magnetic drive of AFM cantilevers, the corrosion of the magnetic particle or thin film coating when immersed in liquid environments is an important drawback. This gives rise to undesirable curvatures of the cantilever, degradation of the film/particle magnetic properties or contamination of the sample. In order to study of the stability of Fe-B-N films in aqueous and biological buffer solutions, changes in the optical reflectivity of the films during liquid immersion were measured as a function of the immersion time and for different nitrogen contents. A description of the method is illustrated in Figure 11.a)

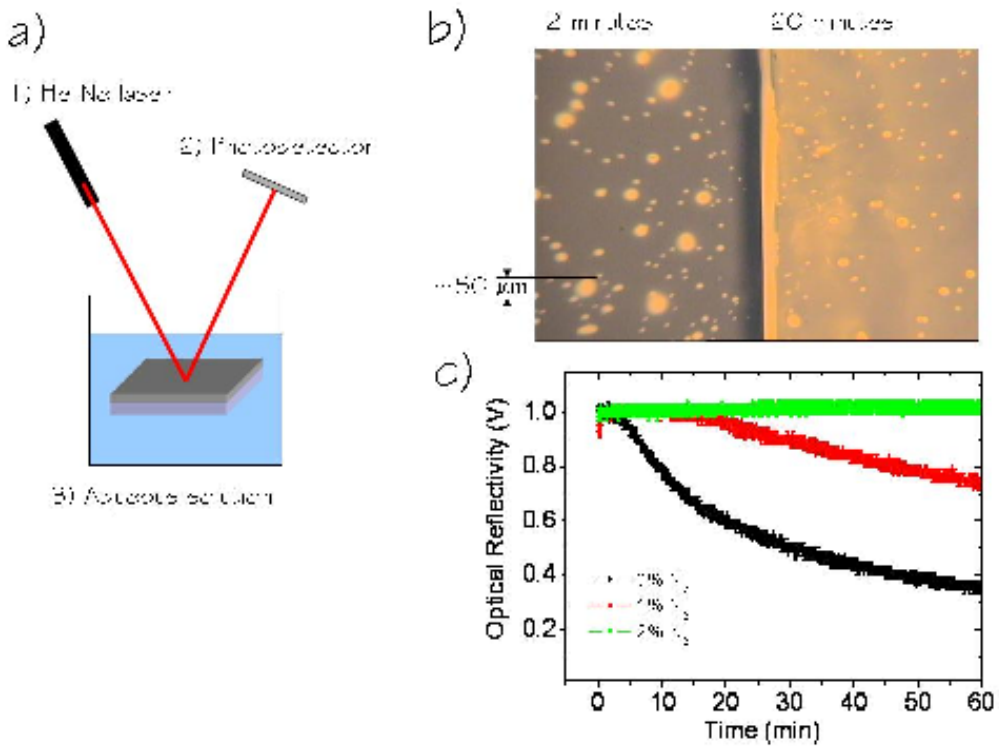

Figure 11 : a) Schematic picture of the experimental set up for the measurement of the reflectivity of coated substrates in liquid environment. b) Optical image of glass coated substrates after 2 and 20 minutes immersion in liquid. There is a high density of holes, accompanied with a variation in the contrast. c) Reflectivity as a function of the time of immersion for different partial pressures of nitrogen.

It consists in a glass or silicon nitride substrate coated with a magnetostrictive Fe-B-N thin film. Changes in the reflectivity are measured using the reflection of a laser beam from the top side of the substrate to the photodetector as a function of the immersion time. It was found that pure amorphous Fe-B thin films were completely dissolved in water after 1 hour. An optical image of the coated substrate after 2 and 20 minutes immersion is shown in Figure 11.b). A fast formation of holes, which diameter ranges between 10 to 50 μm is accompanied by a monotonously decrease of the reflectivity, as observed in the different contrast between both substrates. However, for a moderate presence of nitrogen during deposition (~2% of nitrogen partial pressure), there was no change in the Fe–B-N film properties as observed in Figure 11.c), where the film optical reflectivity is represented as a function of the immersion time . Even when the film coated substrates were immersed for a year either the film reflectivity or the film magnetic properties remain unaltered. This means that the presence of nitrogen during sputtering of amorphous Fe-B films improves its corrosion. These films were also found to be resistant to standard microfabrication solvents as acetone, isopropyl alcohol, methanol, ethanol and resist developers.

IV.6. Conclusions.

The structural, magnetic and magnetoelastic properties of Fe-B-N amorphous films, sputtered from a $Fe_{80}B_{20}$ target, in a mixture of argon and nitrogen atmosphere, were studied as a function of nitrogen partial pressure. It was demonstrated that nitrogen incorporates into the amorphous lattice preserving the amorphous structure, altering magnetic properties. The atomic percentage of nitrogen that incorporates into the amorphous structure is measured to scale linearly with the nitrogen partial pressure during film growth within the studied range. It has been shown that the chemical environment of boron atoms is strongly influenced by the nitrogen content of the film because of the formation of a chemical bonding B-N. When increasing nitrogen content a progressive change from Fe-B to B-N bonds occurs. A ~20% increase of both the saturation magnetization and the saturation magnetostriction constant are found for the composition $Fe_{0.74}\,B_{0.18}\,N_x$, when x is around 7 to 9 at%, compared to pure $Fe_{80}B_{20}$ amorphous films. Finally, it was shown that the Fe-B-N are corrosion resistant in liquid environment, what makes these films very interesting for the its use in magnetostrictive MEMS.

References.

[1] K. V. Rao, M. Steinback, H. H. Liebermann and L. Barton, *'Nitrogen-bearing amorphous FeVBSi alloys : Thermal and magnetic properties'*, J. Appl. Phys., **53**, 7795 (1982).

[2] H. Karamon, T. Masumoto and Y. Makino, *'Magnetic and electrical*. properties of Fe-B-N amorphous films*'*, J. Appl. Phys., **57**, 3527 (1985).

[3] H. Matsuyama, H. Eguchi and H. Karamon, 'The high-resistive soft magnetic amorphous films consisting of cobalt, iron, boron, silicon and oxygen, utilized for video head devices', **67**, 5123 (1990).

[4] H. Karamon. U. S. Patent number : 4,921,763.

[5] H. Karamon, *'A new type of high-resistive soft magnetic amorphous films utilized for a very* high frequency range', J. Appl. Phys., **63**, 4306 (1988).

[6] S. H. Liou and C. L. Chien, 'Particle size dependence of the magnetic properties of ultrafine granular films', J. Appl. Phys., **63**, 4240 (1988).

[7] S. Ohnuma, M. Ohnuma, H. Fujimori and T. Masumoto, *'Metal-insulator type nanogranular soft magnetic thin films investigations on mechanism and applications'*, J. Mag. Magn. Mat., **310**, 2503 (2007).

[8] T.K. Kim, M. Takahashi, *'New magnetic material having ultrahigh magnetic moment'*, Appl. Phys. Lett., **20**, 492 (1972).

[9] K. Nakajima, S. Okamoto, *'Large magnetization induced in single crystalline iron films by high-dose nitrogen implantation'*, Appl. Phys. Lett., **56**, 92 (1990).

[10] D. J. W. Mous, A. Gottdang, R. G. Haitsma, 'The *novel HVEE 5 MV Tandetron™'*, Nucl. Instr. And Meth. B, **190**, 177 (2001).

[11] D. J. W. Mous, A. Gottdang, R. G. Haitsma, G Garcia Lopez, A. Climent-Font, F. Agullo-Lopez, D. O. Boerma, '*Performance and Applications of the first HVE 5MV Tandetron at the University of Madrid, CP680, Application of Accelerators in Research and Industry: 17th Int. Conf.',* edited by J. L. Duggan and I. L. Morgan, Am. Inst. of Physics 999-2002 (2003).

[12] www.cmam.uam.es

[13] Y. Feng, Z. Zhou, G. Zhao, F. Yang, *"Cross sections for 165° backscattering of 2.0–9.0 MeV 4He ions from nitrogen"*, Nucl. Instr. and Meth. B, **94**, 11 (1994).

[14] E. Andrzejewska, R. Gonzalez-Arrabal, D. Borsa, and D. O. Boerma, *"Study of the phases of iron–nitride with a stoichiometry near to FeN"*, Nucl. Instr. Meth. B., **249**, 838 (2006).

[15] M. Mayer, SIMNRA, Version 5.02, Max Plank Institut für Plasmaphysik,

[16] T. Maruyama and T. Morishita, "Copper nitride thin films prepared by radio-frequency reactive sputtering", J. Appl. Phys., **78**, 4104 (1995).

[17] T. Nosaka, M. Yoshitake, A. Okamoto, S. Ogawa, Y. Nakayama, *"Copper nitride thin films prepared by reactive radio-frequency magnetron sputtering"*, Thin Solid Films, **348**, 8 (1999).

[18] http://webs.uvigo.es/surface/

[19] National Institute of Standards & Technology. X-ray Photoelectron Spectroscopy (2001) Database, Standard Reference Database 20, Version 3.1 http://srdata.nist.gov/xps/

[20] M. S. Martin-Gonzalez, Y. Huttel, A. Cebollada, G. Armelles, F. Briones, *"Surface localized nitrogen incorporation in epitaxial FePd films and its effect in the Magneto-Optical properties"*, Surf. Sci., **571**, 63 (2004).

[21] CRC handbook of chemistry and physics 86th edition 2005-2006

[22] G. C. Hadjipanayisa, A. Tsoukatos, V. Papaefthymiou, A. Simopoulos and A. Kostikas, *'Mössbauer studies and correlation of coercivity with particle morphology in Fe/SiO2 and Fe/BN granular solids'*, Scripta Metallurgica et Materialia, **33**,1679 (1995).

[23] http://www.ucm.es/info/ima/

[24] R. Hasegawa, R. C. O'Handley, and L. I. Mendelsohn, *'Advances in Ferromagnetic Metallic Glasses'* AIP Conf. Proc., **34**, 298 (1976).

[25] E. Luborsky, *'Amorphous Metallic Alloys'*, Butterworths, 308 (1984).

[26] H. Tomita, T. Inoue and T. Mizoguchi, '*Hetero-amorphous Fe-Co-B-C* soft magnetic thin films with uniaxialmagnetic anisotropy and large magnetostriction', IEEE Trans. Magns., **32**, 4529 (1996).

[27] E. Luborsky, *'Amorphous Metallic Alloys'*, Butterworths, 273 (1984).

[28] H. Karamon, T. Masumoto and Y. Makino, *"Magnetic and electrical properties of amorphous Fe-B-N films,"* J. Appl. Phys., **57**, 3527 (1985).

[29] J. F. Pierson and C. Rousselot, *"Amorphous Fe-B-N film deposited by reactive sputtering of a Fe-B target"*, Surf. Coat. Technol., **180-181**, 44 (2004).

V

Dynamic magnetostrictive drive of Atomic Force Microscopy (AFM) cantilevers for liquid operation

V.1. Introduction. 105

V.2. Introduction to Atomic Force Microscopy (AFM). 105

V.3. Fe-B-N thin films for magnetostrictive cantilevers. 110

V.3.1. Residual stress measurement in Fe-B-N coated commercial cantilevers. 110

V.4. Dynamic magnetostrictive drive of AFM cantilevers. 111

V.5. Conclusions. 114

References. 114

V.1. Introduction.

In this chapter, a new imaging mode for dynamic Atomic Force Microscopy (AFM) in liquid environment is described. This method is based on direct magnetostrictive excitation of Fe-B-N coated commercial cantilevers. As shown in the previous chapters, these films exhibit excellent magnetic properties, good corrosion resistance in a liquid environment and nearly zero accumulated stress when properly deposited. In addition, a commercial AFM liquid cell has been modified to generate an alternating magnetic field. A set of miniature solenoids has been designed, built and attached to the cell. The measurements performed of the excitation characteristics as a function of magnetic field amplitude, direction and frequency demonstrate that the magnetic field drives the mechanical resonance of the coated cantilever through the film magnetostriction. Under optimum conditions topographic images of a gold surface were obtained in liquid environment as an operational example.

V.2. Introduction to Atomic Force Microscopy (AFM).

Atomic force microcopy (AFM) is a powerful imaging tool to obtain high spatial real space resolution up to the nanometer scale [1]. The precursor to the AFM, the Scanning Tunneling Microscopy (STM) [2], was discovered by Binning and Rohrer in the early 1980s, a development that earned them the Nobel Prize in Physics in 1986. Binning, Quate and Gerber developed the first AFM in the same year, 1986. The AFM is one of the foremost tools for imaging, measuring and manipulating matter at the nanoscale. The AFM consists of a microcantilever with a sharp tip (probe) at the end that is used to scan the specimen surface, as shown in Figure 1. Cantilevers are typically fabricated of silicon or silicon nitride with a tip radius of curvature of the order of nanometers. When the tip is brought into proximity of a sample surface, forces between the tip and the sample lead to a deflection of the cantilever according to Hooke's law. Depending on the experimental situation, the forces can be mechanical contact force, Van der Walls forces, capillary forces, chemical bonding, electrostatic forces, magnetic forces, Casimir forces, solvation forces, etc.. As well as force, additional quantities can simultaneously be measured through the use of specialized types of probes, as for example scanning thermal microcopy, photo-thermal micro-spectroscopy, etc…. Typically, the deflection is measured using a laser beam reflected from the top of the cantilever into a segmented photodetector, as shown in Figure 1.

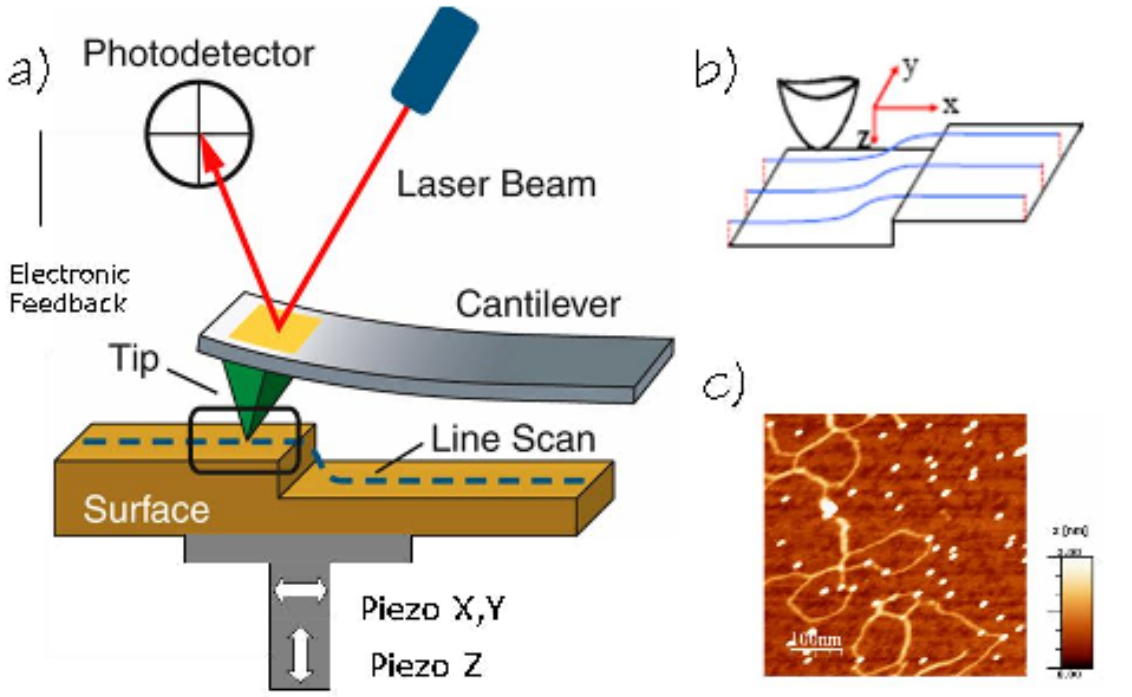

Figure 1 : a) Schematic view of the AFM contact mode operation. The sample is mounted on a piezoelectric tube, that can move the sample in the z direction for maintaining a constant force, and in the x and y directions for scanning the sample. The microcantilever, sharp tip and segmented photodetector are shown. b) Schematic view of the tip scanning the surface. c) AFM image of gold nanoparticles and ADN deposited on mica (Courtesy of Mariana Köber).

If the tip is scanned at a constant height, there is risk of colliding with the surface, causing damage. Hence, in most cases a feedback mechanism is employed to adjust the tip-to-sample distance to maintain a constant force between the tip and the sample. Traditionally, the sample is mounted on a piezoelectric tube, that can move the sample in the z direction for maintaining a constant force, and in x and y directions for scanning the sample. The AFM can be operated in a number of modes, depending on the application. In general, possible imaging modes are divided into static (also called contact) modes and a variety of dynamic (or non-contact) modes.

In the *contact mode operation*, the static tip deflection is used as a feedback signal. Low stiffness cantilevers are used to obtain a better signal to noise ratio. However, close to the surface of the sample, attractive forces can be quite strong, causing the tip to 'snap-in' the surface. Thus contact mode AFM is almost always done in contact where the overall force is repulsive. The force between the tip and the surface is kept constant during scanning by maintaining a constant deflection. In the *dynamic mode (or tapping mode)*, the cantilever is externally oscillated up at down at near its resonance frequency by a small piezoelectric ceramic mounted in the AFM tip holder. When the driving frequency is near a bending-mode resonance of the cantilever, the cantilever is driven into motion which causes an ac signal to be detected by the segmented photodetector. The oscillation amplitude, phase and resonance frequency are modified by tip-sample interaction forces. These changes in oscillation with

respect to the external reference oscillation provide information about the characteristics of the substrate surface. Due to the interaction of forces acting on the cantilever when the tip comes close to the surface, Van der Waals force or dipole-dipole interaction, electrostatic forces, etc… cause the amplitude of this oscillation to decrease as the tip gets closer to the sample. An electronic feedback loop adjusts the height of the tip to maintain a set oscillation amplitude as the cantilever is scanned over the sample. A Tapping AFM image is therefore produced by imaging the force of the oscillating contacts of the tip with the sample surface. For example, tapping mode is gentle enough even for the visualization of adsorbed single polymer molecules under liquid medium. However, a proper adjustment of the scanning parameters is often difficult when using tapping mode AFM for imaging soft materials in liquid environment.

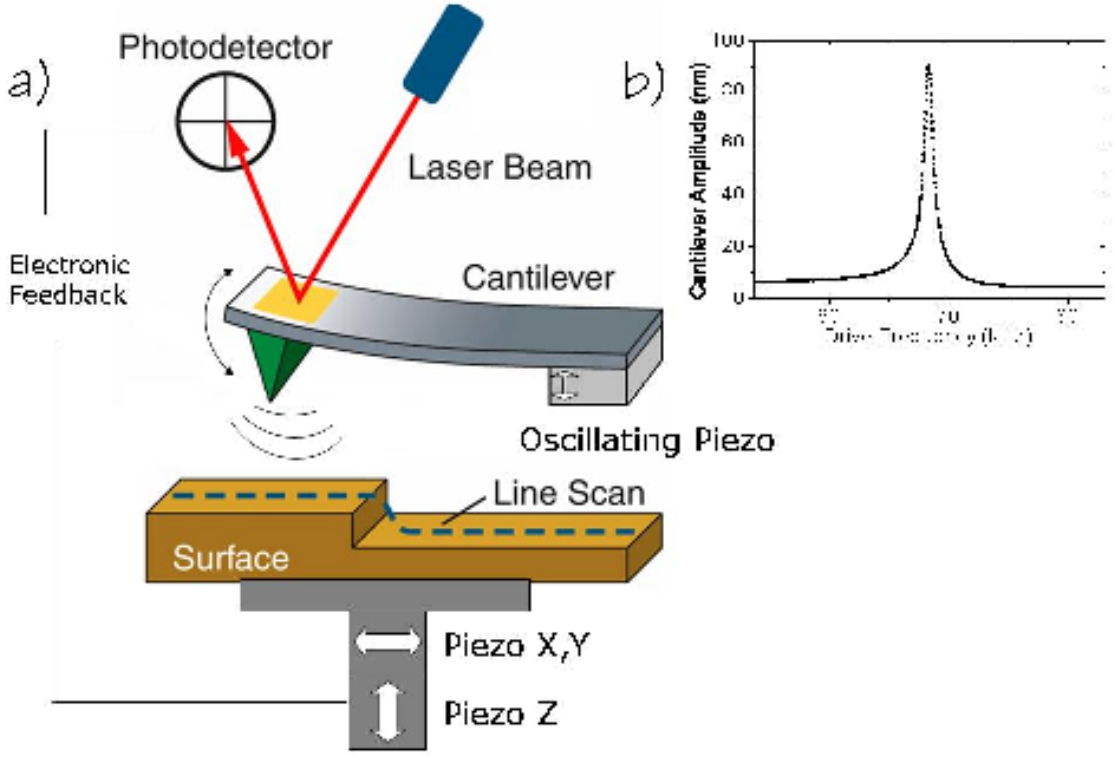

Figure 2 : a) Schematic view of the dynamic mode operation of AFM. The cantilever is externally oscillated up at down at near its resonance frequency by a small piezoelectric ceramic mounted in the AFM tip holder. The oscillation amplitude, phase and resonance frequency are modified by tip-sample interaction forces. An electronic feedback loop adjusts the height of the tip to maintain a set cantilever oscillation amplitude as the cantilever is scanned over the sample. b) Cantilever oscillation amplitude as a function of the drive frequency. The mechanical resonance of the cantilever in air is placed at 68 kHz.

However, for topographic measurements in liquid environment, the oscillation amplitude of the cantilever becomes viscously damped. By using acoustic excitation, this means that a substantial piezo-ceramic excitation amplitude to drive the cantilever into motion is required. In addition, the fluid acts as a coupling medium between the source of acoustic excitation and the fluid cell assembly, resulting in a amplitude/frequency resonance curve usually described as a ‘forest of peaks’. These resonances make the determination of the true cantilever resonance

problematic, as shown in Figure 3. This complicated operation parameter limits the applications of this operation mode. New alternatives in which the cantilever is directly excited, avoiding unwanted mechanical coupling have been proposed, as for example magnetic modulation [3].

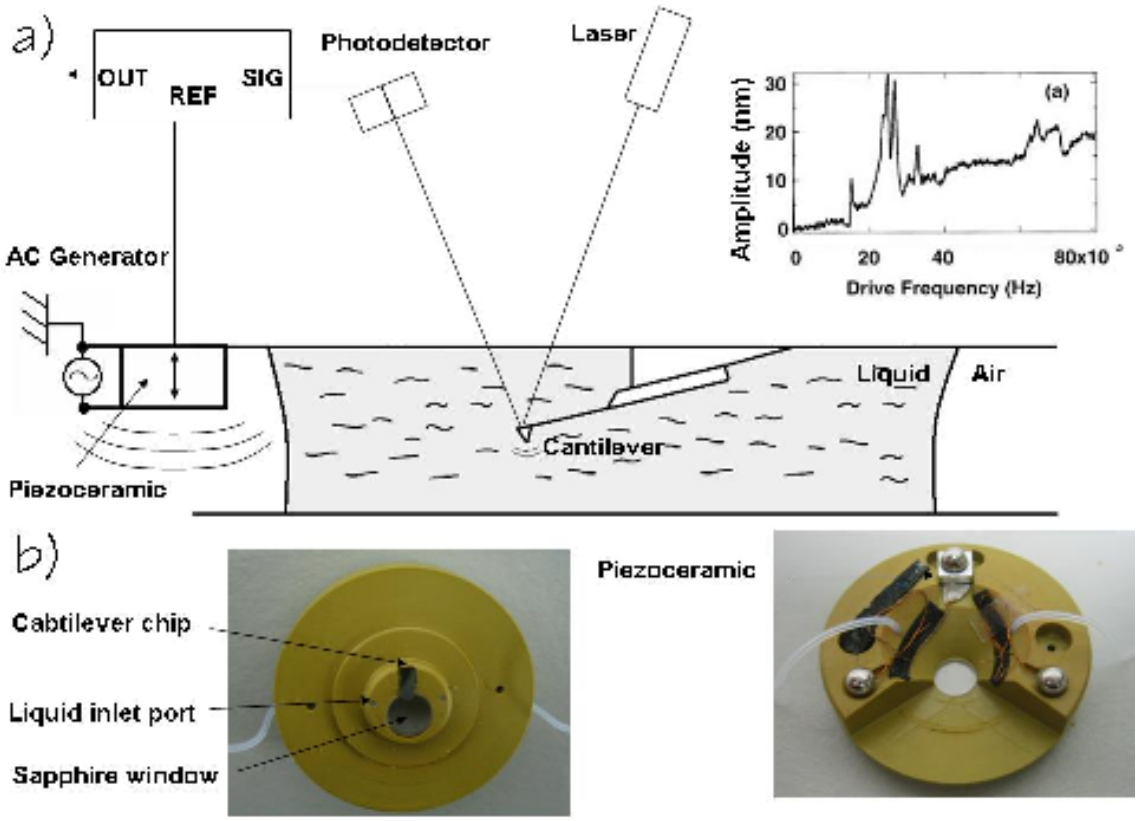

Figure 3 : a) Schematic view of the acoustic excitation of AFM cantilevers in liquid. A piezoelectric ceramic mounted in the AFM tip holder is used to drive the cantilever to its resonance frequency. The inset shows a spectrum of the cantilever oscillation amplitude as a function of the drive frequency. As shown, it is difficult to distinguish the resonance peak corresponding to the cantilever. Numerous unwanted peaks that mask the actual resonance peak are observed due to vibration of the liquid cell. Pictures of the commercial liquid cell (Nanotec). Notice the sapphire window, the piezoceramic, the cantilever chip and the liquid inlet port.

Magnetic drive of AFM cantilevers in liquids have been extensively used in the last years either by coating the cantilevers with a thin ferromagnetic layer [4] or mounting a small magnetic particle on the end of the cantilever [5]. An external alternating magnetic field generated by a solenoid is applied to drive the cantilever. As opposed to acoustically-excited AFM, in this case the cantilever is directly excited/driven and no spurious oscillation of microscope components appears, as shown in Figure 4.

Reduction of the spurious signal arising from excitation of microscope components other than the cantilever is important for several reasons. For example, it results in much easier operation because the only ac signal received by the segmented photodetector is that generated by motion of the cantilever itself. Also, there is no need to hunt for a frequency at which the background is free enough of spurious signals. Instead, an optimum frequency

(usually the highest at which adequate deflection of the cantilever may be obtained) for the experiment can be chosen without regard to this factor. Moreover, there is a improvement in sensitivity results allowing microscope operation at a smaller amplitude of oscillation.

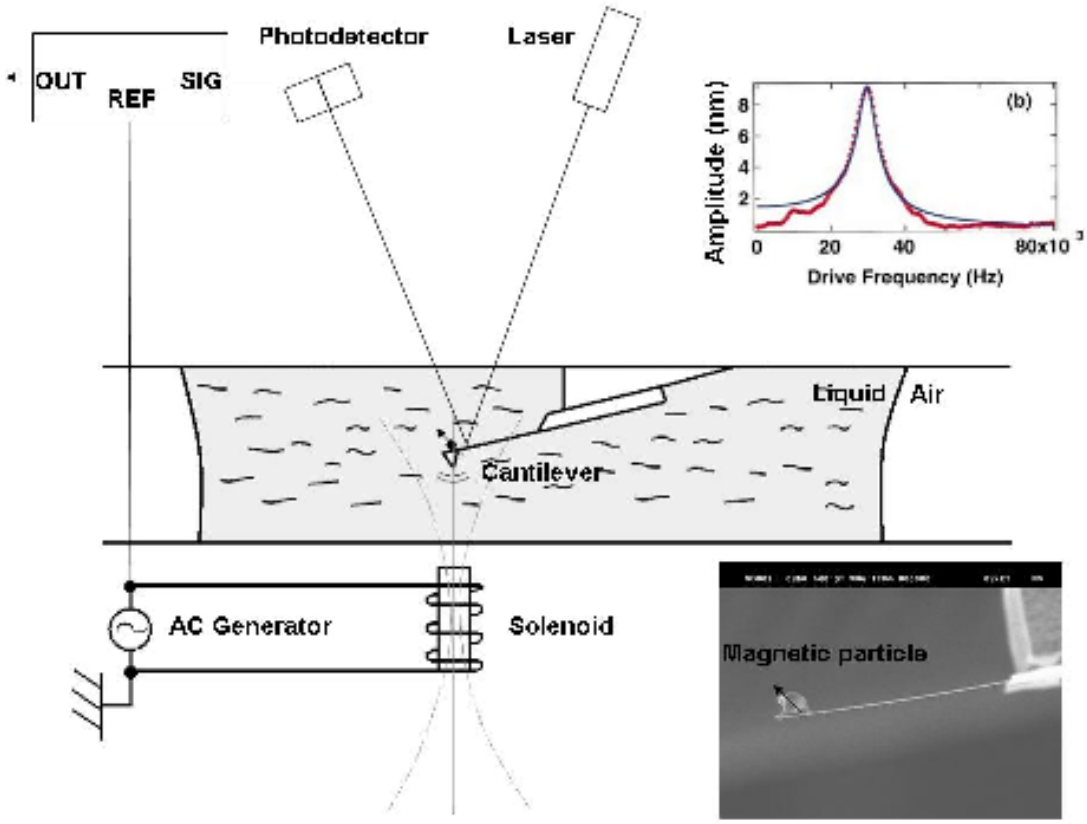

Figure 4 : Schematic view of the Magnetically Activated Mode of operation (MAC-Mode). A electromagnet under the fluid cell is shown. The insets show a spectrum of the cantilever oscillation amplitude as a function of the drive frequency, where a single resonance frequency peak of the AFM cantilever is obtained, and a SEM image of a magnet mounted on the end of the cantilever.

Several combinations of the orientation between the particle/film magnetization and the applied magnetic field were studied in the literature [6]. In the first case, the magnetic particle/film is permanently magnetized in the direction perpendicular to the applied magnetic field, giving rise to a magnetic force that results from the torque induced by the field on the cantilever. In the second case, the magnetic particle/film is permanently magnetized in the direction parallel to the applied magnetic field, giving rise to a magnetic force that arises from gradients in the field. In both cases, the applied magnetic field necessary to drive the cantilever to motion needs to be in the order of several hundreds of Oe.

There is a Magnetic Actuated Drive (MAD) mechanism commercialized by Veeco [7]. This system uses an electromagnet in the fluid cell to create a magnetic field to drive magnetized cantilevers. Those cantilevers are coated with a magnetic film (Co or Co/Cr) on the top side to preserve the tip sharpness. However, this magnetic coating can lead to the

possibility of contamination of sensitive samples with soluble metal ions and unwanted curvatures due to corrosion of the magnetic film coating. It was also shown that the electromagnet of the magnetic drive fluid cell may lead to undesirable warm of the fluid cell sample.

V.3. Fe-B-N thin films for magnetostrictive cantilevers.

Amorphous sputtered Fe-B-N thin films were used for magnetostrictive drive of AFM cantilevers. These thin films present a high saturation magnetostriction coefficient, $\lambda_S=\delta l/l\,|_S$ = + 35 ▪ 10^{-6}, i.e., the dimensional change when the material is magnetized, combined with soft magnetic properties [8]. These magnetic properties of the amorphous film were shown to be stable during repeated scanning of the cantilever in fluid. Moreover, these amorphous films have very good mechanical properties, as well as excellent adhesion and good corrosion resistance. As seen in Chapter II, these films can also be obtained with nearly-zero accumulated stress if properly deposited. The main advantage of depositing the magnetostrictive layer only on the top side is that the sharpness of the probe tip is maintained.

V.3.1. Residual stress measurement in Fe-B-N coated commercial cantilevers.

Commercial silicon nitride cantilevers (MikroMasch with overall dimensions of 400 μm long, 100 μm wide, and 1 μm thick) were coated with a magnetostrictive Fe-B-N layer using the optimal sputtering deposition conditions obtained in Chapter II : –0.7 kV target potential and 8 • 10^{-3} mbar of Ar working pressure. The curvature induced on the cantilevers were measured by using a reflected laser beam from the top side of the cantilever to a position sensitive photodetector (PSD) [9]. This laser beam is scanned along the cantilever length to obtain a curvature profile, as schematically shown in Figure 5. Flat cantilevers, with a bending value around 0.5 º are obtained. This value is 5 times smaller than that of the commercial evaporated cantilevers, that is typically 3º. An example of a curvature profile along the cantilever is shown in Figure 5.

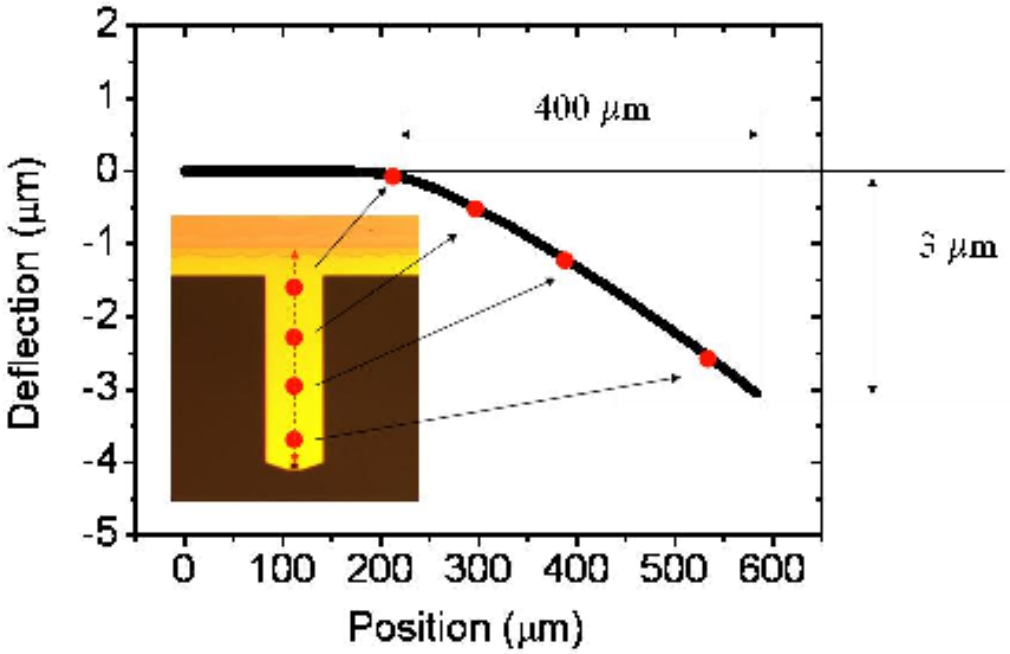

Figure 5 : Cantilever curvature profile. The measured bending value was estimated to be less than 1%.

V.4. Dynamic magnetostrictive drive of AFM cantilevers.

A commercial AFM system (Nanotec Electrónica S.A. [10]) has been modified to implement the dynamic magnetostrictive drive of AFM cantilevers. A description of the method and a picture of the modified liquid cell is shown in Figure 6. The method consists of a cantilever coated with a 20 nm magnetostrictive Fe-B-N thin film, whose deflection is detected by reflecting a laser beam on the top side of the cantilever and measuring the reflecting beam deflection in a segmented photodetector. This is allowed with an optically transparent window on the liquid cell, as shown in Figure 6. The cantilever is attached to a liquid cell which holds it above the surface of the sample and may be submerged in a fluid. A coil wounded onto a ferrite core are positioned closed to the cantilever in order to generate an alternating magnetic field. This magnetic field lead to a magnetostrictive cantilever oscillation up at down at near its resonance frequency. An alternating driving signal of around 50 mAmps (rms) drives the coil and produces a magnetic field of around 5 Oe (rms), as measured by a Gaussmeter in the low frequency regime. The limited bandwidth of the Gausmeter (2kHz) limits the measurement of the field intensity at higher frequencies. An important property of this modulation method is that the intensity of the applied magnetic field is independent of the tip-sample separation. In addition, the applied field is predominantly parallel to the plane of the cantilever, what maximizes the magnetostrictive strain and minimizes any magnetostatic force. As similar to the conventional dynamic modes, the oscillation amplitude, phase and resonance frequency is measured in the segmented photodetector and compared with the external reference signal as the cantilever approaches the sample to obtain information about its surface. For geometrical constrictions, the applied magnetic field has to be applied parallel to the short edge of the cantilever. Then, the coating hard axis direction is chosen parallel to that edge to maximize the

magnetostrictive strain. Silicon nitride Olympus cantilevers, 100 μm long and 800 nm thick, which resonant frequency was around 71 kHz, were used. After coating with 20 nm of Fe-B-N, the resonant frequency dropped to 68 kHz.

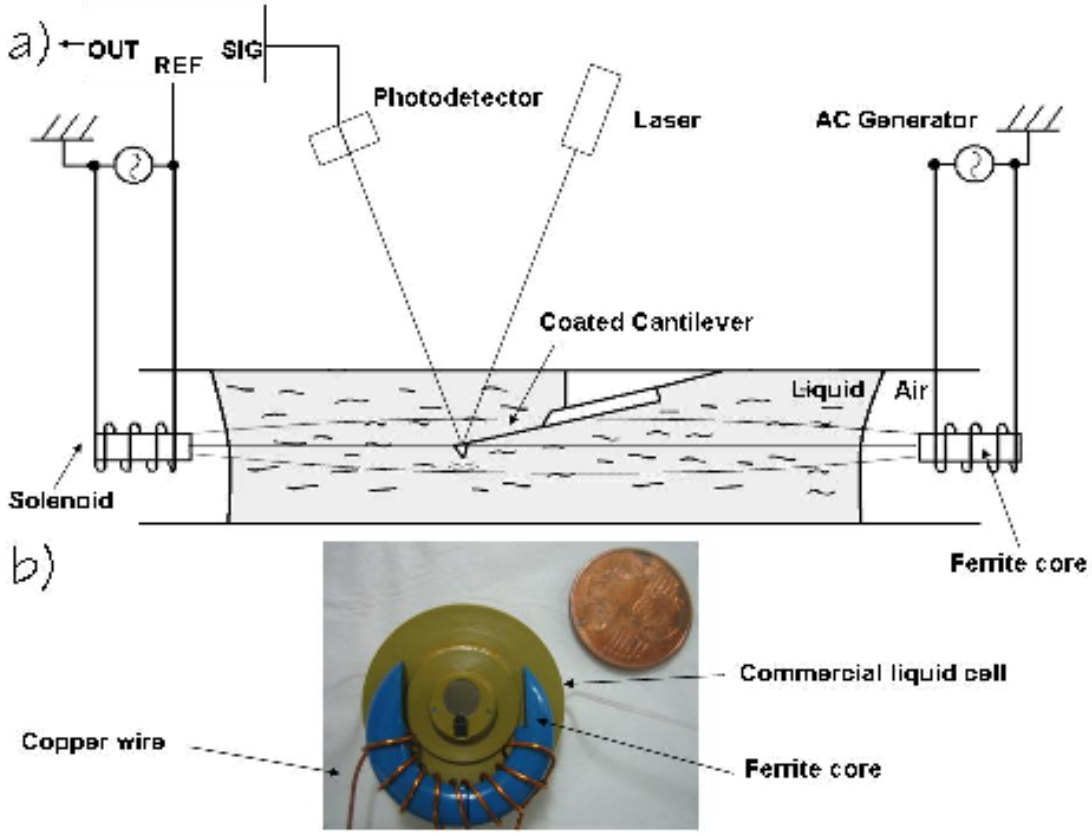

Figure 6 : a) Schematic of the Magnetostrictive drive of AFM cantilevers. b) Picture of the commercial liquid cell (Nanotec) modified for magnetostrictive modulation. A solenoid with a ferrite core is wounded to the liquid cell.

The amplitude oscillation of the cantilever as a function of the drive frequency when the liquid cell is immersed in water and excited acoustically with a piezoelectric is shown in Figure 7.a). As shown, the amplitude/frequency resonance curve can be described as a 'forest of peaks' corresponding to the mechanical resonances of the microscope. Due to the substantial background signal, the determination of the true cantilever resonance is problematic. This is not the case when the cantilevers are excited directly with the magnetostrictive method, as it can be shown in Figure 7.b). The amplitude oscillation of the cantilever is represented as a function of the drive frequency of the applied magnetic field, in air and liquid environment. The amplitude/frequency curve is less noisy. This method is able to overcome the limitations inherent to operation in liquid, where the resonant vibration of the cantilever is impeded by the large damping and inertial mass of the liquid [11]. Both effects, result into a low quality factor (Q) and the shift of the resonance to lower frequencies respectively. As expected, the resonance peak amplitude is damped when the cantilever in immersed in liquid (the quality factor reduced its value from 100 to 4), while the resonance frequency shifts to lower

frequencies (from 68 to 21kHz). The observed signal is essentially free of the spurious signals as compared with acoustically-excited cantilever response. As a consequence of this, the sensitivity of the microscope is essentially independent of the driving frequency. Moreover, the lack of a background signal permits the use of lower amplitudes of oscillation which, when combined with softer cantilevers, results in a substantial decrease of the energy deposited into the sample and consequently, a reduction in the sample damage.

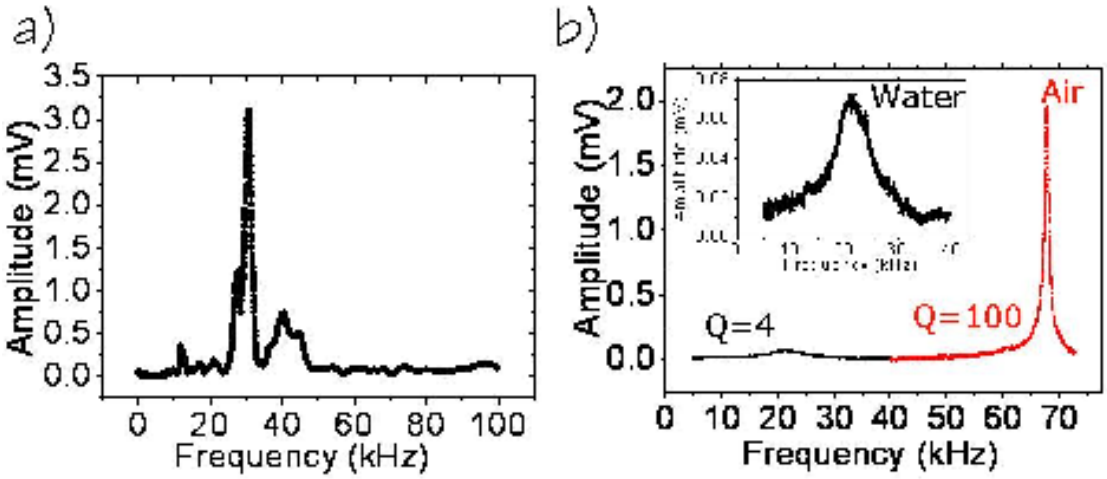

Figure 7 : a) Up: Amplitude oscillation of the AFM cantilever as a function of the drive frequency in liquid environment for the acoustic drive of the liquid cell. The sharp peaks correspond to mechanical resonances of the microscope. b) Amplitude oscillation of the magnetostrictive cantilever as a function of the drive frequency in air and liquid environment. It is shown how the amplitude and Quality factor (Q) is reduced when the cantilever is immersed in water solution. Moreover, the resonant frequency shifts to lower values, as expected for larger inertial mass of the liquid environment.

Contrary to expected, the excitation and the cantilever oscillation frequencies were found to be the same, even when magnetostriction is a odd function of the film magnetization [Chapter I, Section I.4.3.]. This can be explained with the fact that the initial state of the film magnetization is unknown (there is some remanent magnetization of the ferrite core), and the low intensity of the applied magnetic field in not able to reverse the film magnetization.

As an operational example, the ability of this method to obtain topographic images of a gold surface under water solution is shown in Figure 8. No significant difference in height and width of the grains appear comparing between measurements that it has been made both in liquid and in air.

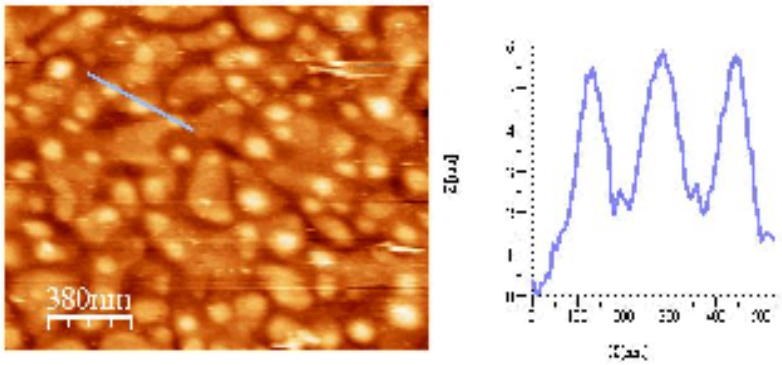

Figure 8: Topographic image and the corresponding scan profile of gold grains obtained with the magnetostrictive drive method in water.

V.5. Conclusions.

In this chapter, a novel dynamic magnetostrictive drive of Atomic Force Microscopy (AFM) cantilevers is described, obtaining topographic images in liquid environments. This method differs form the commercial ones in the manner in which the cantilever is driven. In order to excite them inside the liquid, commercial silicon nitride cantilevers have been coated with sputtered thin magnetostrictive Fe-B-N films. These films exhibit excellent magnetic properties, good corrosion resistance in a liquid environment and nearly zero accumulated stress when properly deposited [Chapter II]. In addition, a new AFM liquid cell with a set of miniature solenoids has been designed and built. Within this cell, the cantilever is excited with an alternating magnetic field. The measurements performed of the excitation characteristics as a function of magnetic field amplitude, direction and frequency demonstrate that the magnetic field drives the mechanical resonance of the coated cantilever through the film magnetostriction. Under optimum conditions topographic images of a gold surface were obtained in liquid environment as an operational example.

References.

[1] G. Binnig, C. F. Quate and C. Gerber, *"Atomic force microscope",* Phys. Rev. Lett., **56**, 930 (1986).

[2] G. Binning and H. Rohrer, *"The scanning tunneling microscope"*, Sci. Am., **253**, 50 (1985).

[3] S. M. Lindsay, Y. L. Lyubchenko, N. J. Tao, Y. Q. Li, P. I. Oden, J. A. De Rose, and J. Pan, *"STM and AFM studies of biomaterials at a liquid-solid interface"*, J. Vac. Sci. Technol. A, **11**, 808 (1993).

[4] Wenhai Han, S. M. Lindsay and Tianwei Jing, *"A magnetically driven oscillating probe microscope for operation in liquids",* Appl. Phys. Lett., **69**, 4111 (1996).

[5] S. P. Jarvis, T. P. Weihs, A. Oral and J. B. Pethica, *"Mechanics of contacts at less than 100 Å scale: indentation and AFM"*, Mater. Res. Soc. Proc., **308**, 127 (1993).

[6] Irène Revenko and Roger Proksch, *"Magnetic and acoustic tapping mode microscopy of liquid phase phospholipid bilayers and DNA molecules",* J. Appl. Phys., **87**, 526 (2000).

[7] www.Veeco.com

[8] I. Fernández-Martínez, M.S. Martín-González, R. González-Arrabal, R. Álvarez-Sánchez, F. Briones and J.L. Costa-Krämer, *"Nitrided Fe-B amorphous thin films for magnetomechanical systems "*, J. Magn. Magn. Mat., **320**, 68 (2008).

[9] (In collaboration with J. Tamayo). J. Mertens, M. Calleja, D. Ramos, A. Tarýn, and J. Tamayo, *"Role of the gold film nanostructure on the nanomechanical response of microcantilever sensors"*, J. Appl. Phys., **101**, 034904 (2007).

[10] NANOTEC Electrónica S.L. www.nanotec.es

[11] G. Y. Chen, R. J. Warmack, A. Huang, and T. Thundat, *"Harmonic response to near-contact scanning force microscopy"*, J. Appl. Phys., **78**, 1465 (1995).

VI

Fabrication of Nano-Electro-Mechanical Systems (NEMS).

VI.1. Introduction. 119

VI.2. Nano-Electro-Mechanical-Systems (NEMS). 119

VI.3. NEMS fabrication process. 120

VI.4. NEMS fabrication using epitaxial GaAs/AlGaAs heterostructures. 122

VI.5. Strained NEMS for the fabrication of a tunnelling displacement detector. 124

VI.6. Conclusions. 131

References. 132

VI.1. Introduction.

This chapter is dedicated to nano-electro-mechanical systems (NEMS). The basic concepts of NEMS and its fabrication procces are described. Firstly, GaAs/AlGaAs heterostructures grown by Molecular Beam Epitaxy (MBE) are used to fabricate suspended GaAs structures. Finally, a tunneling displacement detector using fabricated nanogaps is proposed. Nanogaps as small as 5 nm were fabricated in a reproducible way.

VI.2. Nano-Electro-Mechanical-Systems (NEMS).

One of the earliest reported electromechanical devices was built in 1785 by Charles-Augustin de Coulomb [1] to measure electrical charge. His electrical torsion balance consisted of two spherical metal balls one of which was fixed, the other attached to a moving rod that acted as capacitor plates, converting a difference in charge between them to an attractive force. The device illustrates the two principal components common to most electromechanical systems irrespective of scale: mechanical elements and transducers. A nano-electro-mechanical system (NEMS) consists of a nanometer scale mechanical element that is coupled to an electronic device [2]. The mechanical element may have a simple geometry, such as a cantilever (suspended beam clamped at one end) or a bridge (suspended beam clamped at both ends) that deflects or vibrates in response to an applied force. These elements are fabricated of semiconductor materials such as silicon (Si) or gallium arsenide (GaAs) using standard semiconductor micro-machining techniques [3]. Because of their size, they can vibrate at frequencies ranging from a few megahertz (MHz) up to around a gigahertz (GHz) [4]. Among the most important technological challenges in the operation of these NEMS are the actuation and detection of their sub-Å displacements at frequencies in the MHz range [5].

The transducers in NEMS convert mechanical energy into electrical or optical signals and vice versa. However, in some cases the input transducer simply keeps the mechanical element vibrating steadily while its characteristics are monitored as the system is perturbed. In this case such perturbations, rather than the input signal itself, are precisely the signals we wish to measure. They might include pressure variations that affect the mechanical damping of the device, the presence of chemical adsorbates that alter the mass of the nanoscale resonator, or temperature changes that can modify its elasticity or internal strain. In these last two cases, the net effect is to change the frequency of vibration.

The actuators provide mechanical stimuli to the mechanical element, converting an input impulse into motion. There are several techniques that have extensively used, electrostatic, acoustic, bimetallic, etc… In this thesis, magnetostriction, the dimensional change of a magnetic material resulting from a change in its magnetic state is studied and used for cantilever actuation.

Most recent NEMS are resonant devices where the mechanical element is excited in one of its resonant modes. For the fundamental out-of-plane flexural mode resonance of a cantilever, the resonance frequency f_0 can be expressed as:

$$f_0 = \frac{1}{2\pi}\sqrt{\frac{E}{\rho}}\frac{t}{L^2} \qquad (1)$$

where E, ρ, t and L are the Young's modulus, density, thickness and length of the beam respectively.

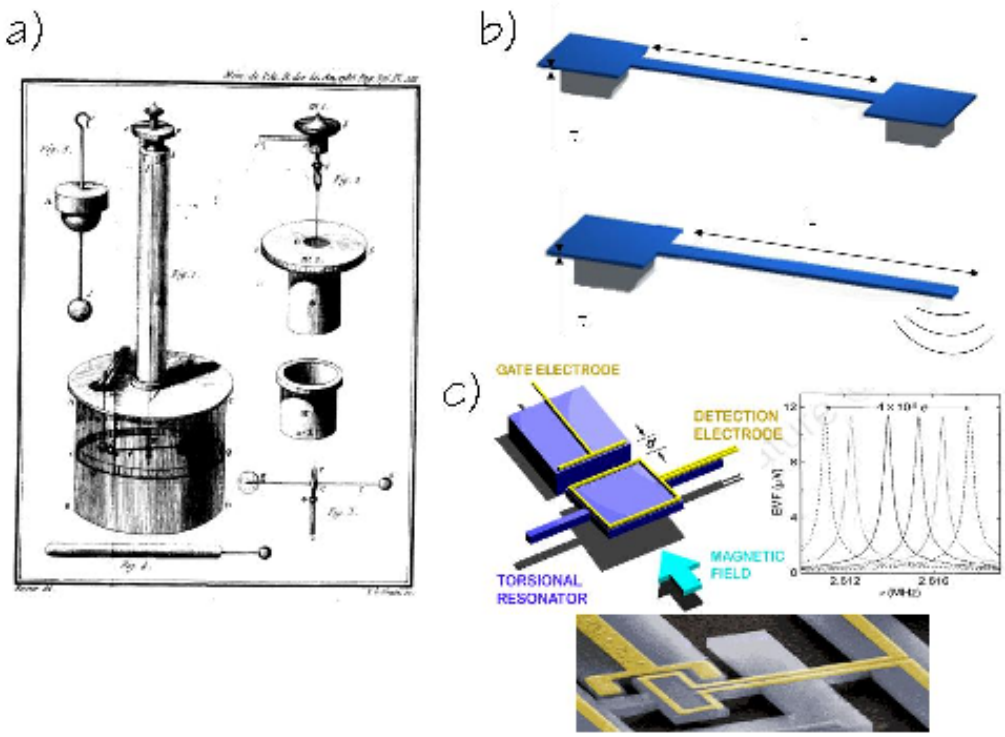

Figure 1 : a) Picture of the first reported electromechanical device: an electrical torsion balance built in 1875 by Coulomb. It was used for measuring the electrical charge. b) Schematic picture of the typical mechanical elements used: cantilever and bridge. c) A nanometer-scale mechanical electrometer fabricated with standard semiconductor micro-machining and with a high charge sensitivity [6].

VI.3. NEMS fabrication process.

Several micro-machining techniques have been developed for patterning freely suspended three dimensional (3D) semiconductor structures. These techniques apply silicon-on-insulator (SOI) heterostructures, as well as systems based on gallium arsenide (GaAs). As shown in Figure 2, the procedure begins with a heterostructure that contains structural (red) and sacrificial layers (blue) on a substrate (yellow). Typically, the structure layer is fabricated of Si or GaAs, whilst silicon dioxide (SiO_2) or aluminium gallium arsenide (AlGaAs) are used as sacrificial layer. Masks on top of this substrate are patterned by a combination of optical and

electron-beam lithography, followed by a thin-film deposition process. The resulting mask (black), usually fabricated of aluminium (Al) or titanium (Ti), protects the material beneath it during the next stage. The unprotected material around the mask is then etched away using a plasma-based process, typically ion milling with argon, or Reactive Ion Etching (RIE) with methane or fluoride mixtures [7]. Finally, a wet chemically selective etch step using hydrofluoric acid (HF) in water solution, removes the sacrificial layer from specific regions to create freely suspended nanostructures that are both thermally and mechanically isolated.

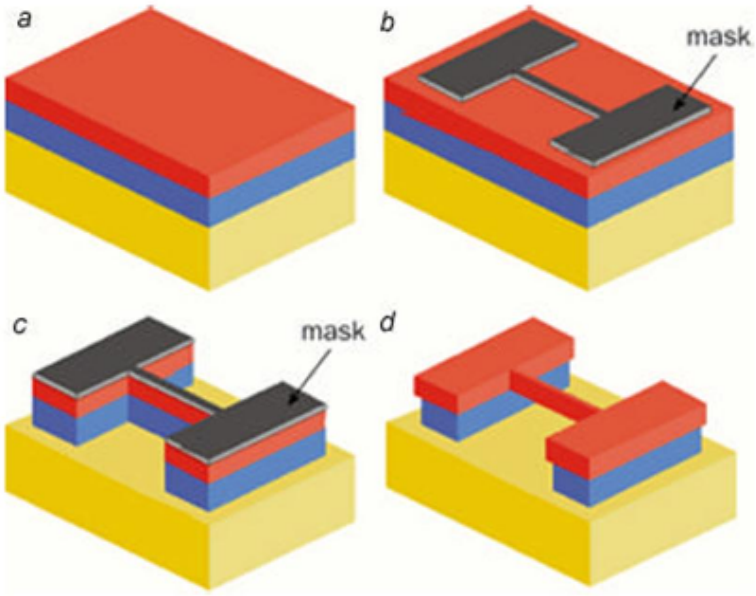

Figure 2 : a) The procedure begins with a heterostructure that contains structural (red) and sacrificial layers (blue) on a substrate (yellow). b) Masks on top of this substrate are patterned by a combination of optical and electron-beam lithography, followed by a thin-film deposition process. The resulting mask (black) protects the material beneath it during the next stage. c) Unprotected material around the mask is then etched away using a plasma process. d) Finally, a local chemically selective etch step removes the sacrificial layer from specific regions to create freely suspended nanostructures that are both thermally and mechanically isolated.

A well-known problem in the fabrication of NEMS is stiction, which occurs when surface adhesion forces are higher than the mechanical restoring force of the suspended structure. Surface effects become more important when the mechanical elements shrink in size. Suspended structures usually stick to the substrate during the drying process after the wet etching of the sacrificial layer. This is because the liquid meniscus formed on hydrophilic surfaces during drying pulls the microstructure towards the substrate, as schematically shown in Figure 3.a). Once contact has been made, forces like Van der Valls, electrostatic, hydrogen bridging etc… result in permanent attachment of the structure to the substrate. Several procedures has been developed to avoid this release-stiction problem, as for example supercritical CO_2 drying [8], anti-stiction coating [9], etc…

In this thesis, a “freeze drying” method has been used to avoid stiction during sacrificial etching. In this method a final rinsing agent is frozen and subsequently sublimated in a few hours under a nitrogen atmosphere. The main advantage of using this method is that the liquid-gas interface is avoided, minimizing the capillarity forces, and no vacuum or complicated systems are required [10]. Cyclohexane, which freezes at about 7ºC is used as a final rinsing agent. Freezing and subsequent sublimation are accomplished by placing the substrate under a nitrogen flow on a regulated Peltier element with a temperature below the freezing point, typically -10ºC. To achieve this temperature, the hot side of the Peltier element is water cooled, while a DC current of 3 Amps is passed through it. The total time for the sublimation process was typically 2 hours. As high purity cyclohexane was used, no residues were observed. Cantilevers with high aspect ratios (length/thickness) as high as 500, at a gap spacing of 1 μm, were obtained by this freezy-drying method.

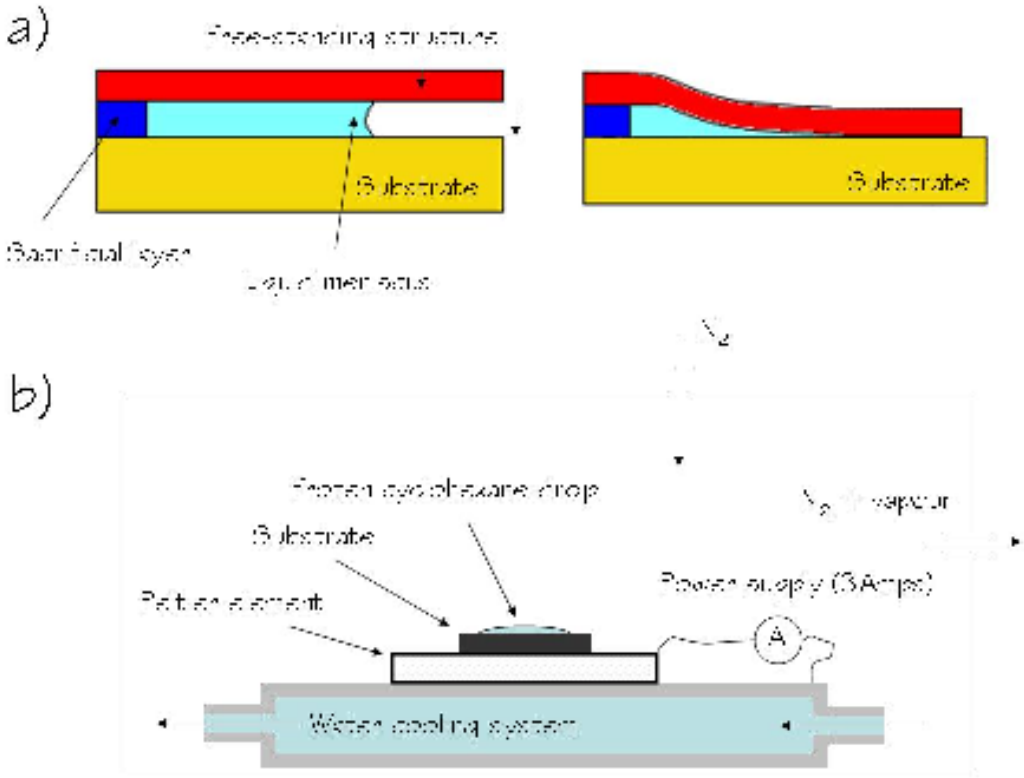

Figure 3 : a) Schematic picture of the stiction process during the drying process after the wet chemical etching. A liquid meniscus pulls the microstructure towards the substrate. b) Schematic of the cyclohexane drying set up.

VI.4. NEMS fabrication using epitaxial GaAs/AlGaAs heterostructures.

In this thesis, suspended structures were fabricated from molecular beam epitaxy (MBE)-grown GaAs/$Al_{0.75}Ga_{0.25}As$ heterostructures. These heterostructures were grown on GaAs (001) substrates. The thickness of the structural GaAs layer varied between 100 to 200 nm, while the

thickness of the sacrificial layer was 1 μm. Masks on top of the heterostructure were patterned by a combination of optical and electron-beam lithography, followed by thin-film deposition processes (either e-beam evaporation or sputtering) of a Ti or Al layer. These metallic materials were used, as they are etched away during the wet etching of the AlGaAs sacrificial layer. The structural layer is released by using an HF solution (1.5% in water). Doubly and singly clamped beams were fabricated, which lengths vary between 500nm to 50 μm.

Once the structures were fabricated, they were observed either by scanning electron or optical microscopy. In both cases, there is a clear contrast between suspended and stuck structures, as shown in Figure 4. The etching rate (1 μm • min^{-1}) of the AlGaAs layer was extracted, measuring the depth of the sacrificial layer etching or undercutting.

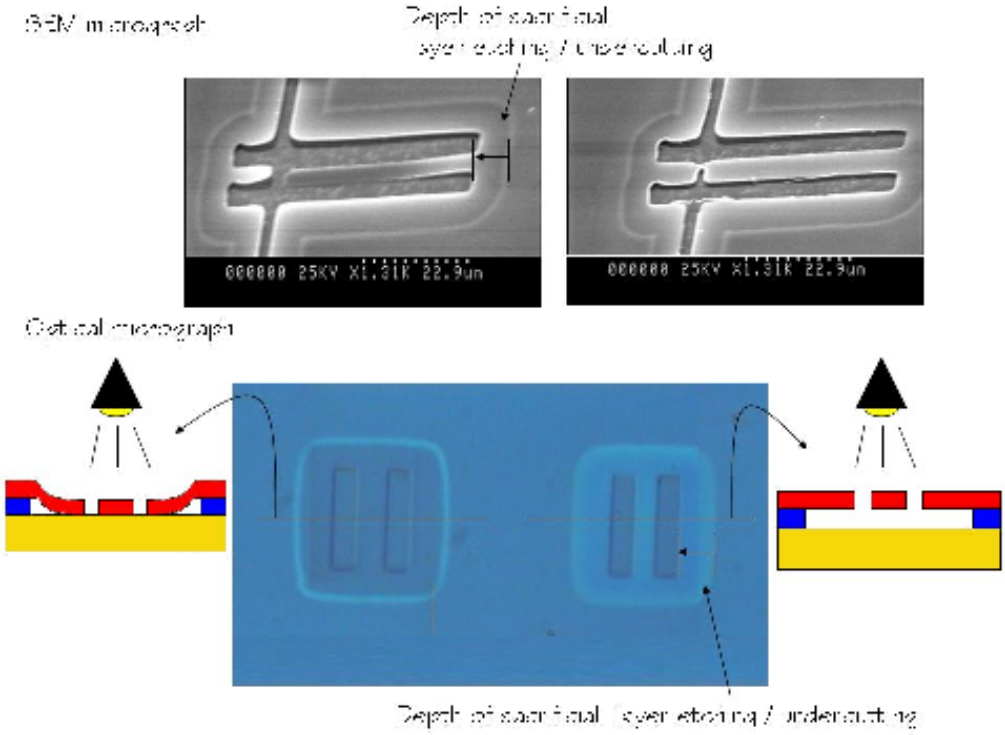

Figure 4 : a) SEM and optical image of fabricated GaAs structures which are suspended (right) or stuck (left) to the substrate.

Some examples of the fabricated cantilevers (clamped at one end) and bridges (clamped at both ends) are shown in Figure 5.

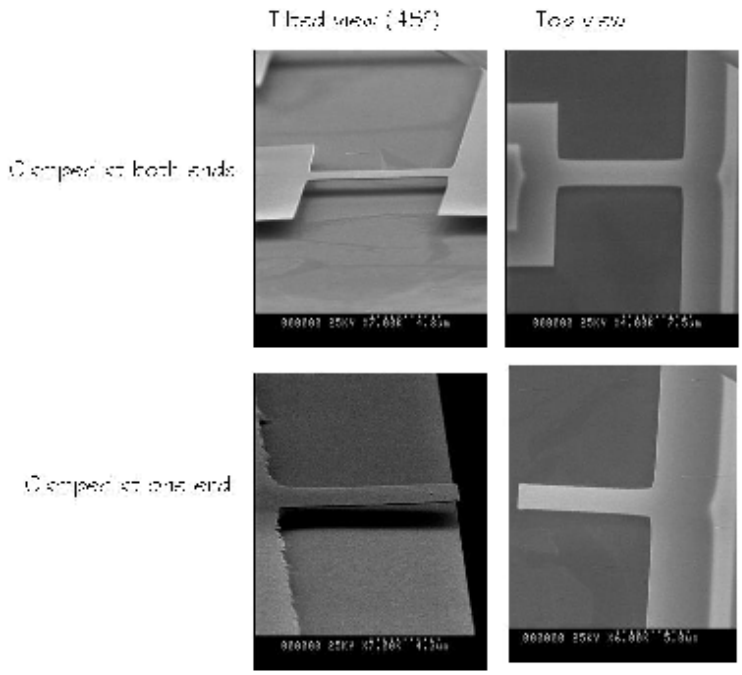

Figure 5 : a) SEM image of fabricated GaAs cantilevers and bridges. Devices were tilted 90º during the image acquisition to ensure that the sacrificial layer is completely etched.

VI.5. Strained NEMS for the fabrication of a tunnelling displacement detector.

Detection of displacements at the nanoscale is a significantly challenge task [5], because of the very small displacement amplitudes in NEMS (sub-Å) at high frequencies (MHz-GHz). Recently, optical interferometric techniques [11], capacitive [12] or piezoresistive detection [13] have been developed for NEMS displacement detection. However, when decreasing the length scale from micrometers to nanometers, the use of these techniques becomes difficult, as for example due to reduction of the capacitance compared to the parasitic currents. In this thesis, an alternative sensor that relies on the quantum mechanical tunneling effect is proposed for NEMS detection.

When the gap between two conductors is small enough, an electron can tunnel through the energy barrier from one side to the other with a finite probability. This tunnelling current is an exponential function of the distance *d* between the electrodes and the tunnelling barrier ϕ, which corresponds to the effective work function of the electrodes:

$$I = I_0 exp\left(-\frac{2}{\hbar}\sqrt{2m\varphi}d \right) \qquad (2)$$

where I_o depends on the applied voltage across the gap and m is the electron mass. Practically, this effect is relevant for distances on the order of 1 nm and below. The tunneling current does not depend on the dimensions of the electrode (as in the case of capacitive detection) which makes it specially well suited for NEMS applications. For example, the tunnelling current between a sharp tip and a sample is used in Scanning Tunneling Microscope (STM) [14] to image topography. Even when tunnelling sensors should show a extreme displacement sensitivity, only a few developments, as for example infrared detectors [15] or accelerometers with micro-g sensitivity [16] have been reported. This is due to some practical problems in sensor construction and operation.

The main difficult in the tunnelling sensor manufacturing lies in the fabrication of a stable nano-separation or nanogap between the tunnelling sensor and the NEMS. In addition, this distance should be on the order of 1nm, which is below the lower limit of standard lithographic techniques. For example, in reference [17] they use a adjustable tip electrode which is approached to the NEMS structure. The metallic tip measures a tunnelling current when the NEMS structure is deflected, demonstrating the proper operation of a tunnelling sensor, but showing a limited stability and mechanical noise.

A new concept for a tunnelling sensor is proposed in this thesis. The NEMS, in this case a nanocantilever, is separated a few nanometers from a electrode that measures a tunnelling current proportional to that separation, and consequently, to the cantilever flexural deformation, as schematically shown in Figure 6. The electrode or tunnelling sensor is positioned in front of the nanocantilever.

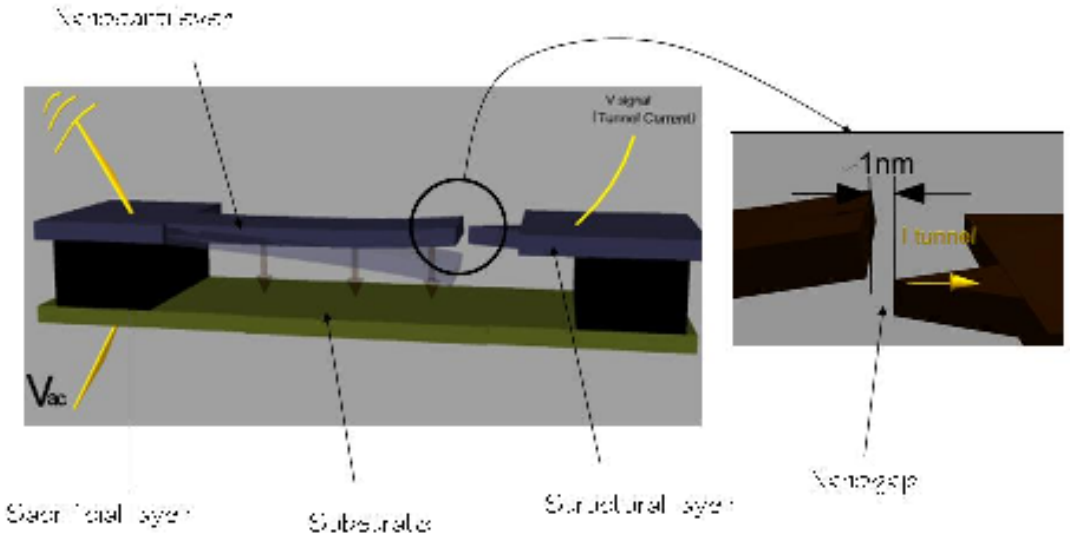

Figure 6 : Schematic picture of the tunneling sensor proposed in this thesis. The tunneling current passing through the nanogap depends on the nanocantilever deflection. .

To achieve these nano-separated electrodes or nanogaps, a novel strain-release break junction was developed [18]. This method uses strained (or pre-stressed) structural layers that release its stress when removing the sacrificial layer, giving rise to a contraction of several nanometers length, as explained it what follows.

The ability of MBE to grow multilayer heterostructures, with thickness control in the atomic scale, is used to fabricate NEMS structures with a well defined stress state [19]. The GaAs structural layer was grown with a strong in-plane tensile accumulated stress, by embedding a certain number of stressors of one atom thickness into the layer, as schematically shown in Figure 6. These stressors are GaP MLs which has a lattice parameter 3.57% smaller than GaAs. The lattice mismatch is accommodated during growth by strain of the GaP layer, giving rise to a biaxial in-plane tensile accumulated stress.

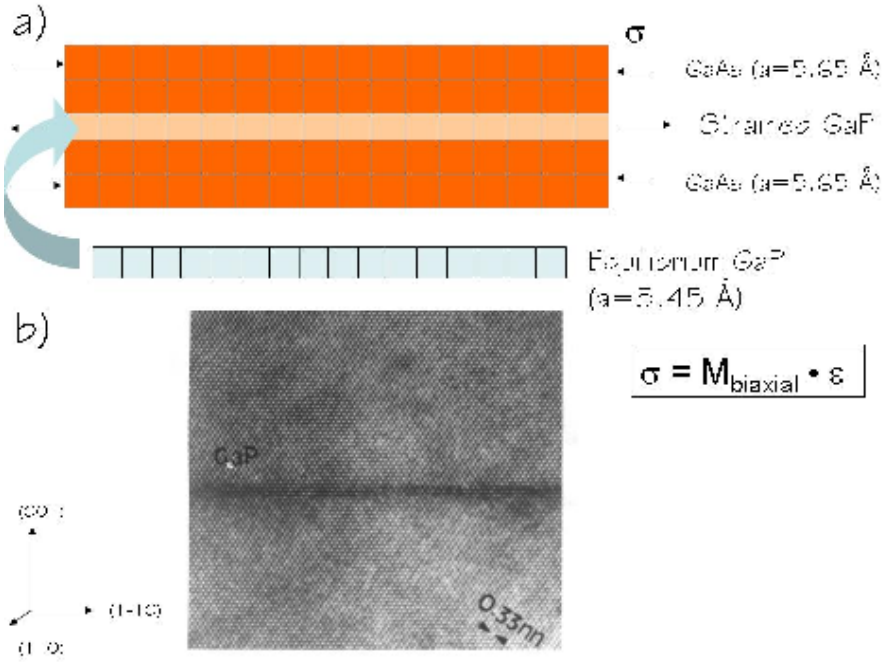

Figure 6 : a) Schematic picture of a strained GaP monolayer embedded in a GaAs matrix. b) Transmission Electron Microscope picture of a grown heterostructure with two GaP monolayers embedded in a GaAs matrix. Very flat and abrupt interfaces are shown [20].

As shown in Section VI.4., the heterostructure for NEMS micro-fabrication contains a structural and sacrificial layer on a substrate. The heterostructure fabrication starts with a 1μm thick $Al_{0.75}Ga_{0.25}As$ sacrificial layer grown on a GaAs (001) substrate. Following the AlGaAs layer, a top structural layer is grown, containing ten periods of (n-type) $(GaAs)_{56}/(GaP)_1$ superlattice, finished with a 56 MLs thick GaAs layer. This results in a GaAs/GaP heterostructure with 10 MLs of GaP symmetrically distributed through the GaAs/GaP structural

layer, which accumulates a strong tensile stress. A schematic view of the final heterostructure is shown in Figure 7.

As individual GaP monolayers are embedded in the structural GaAs layer, it is ensured that no defects or misfit dislocations are formed, maintaining a flat and abrupt interface, as shown in Figure 2.b). As studied in earlier works, the critical thickness for misfit dislocation formation of GaP grown on GaAs is 1.58nm (3MLs) [20].

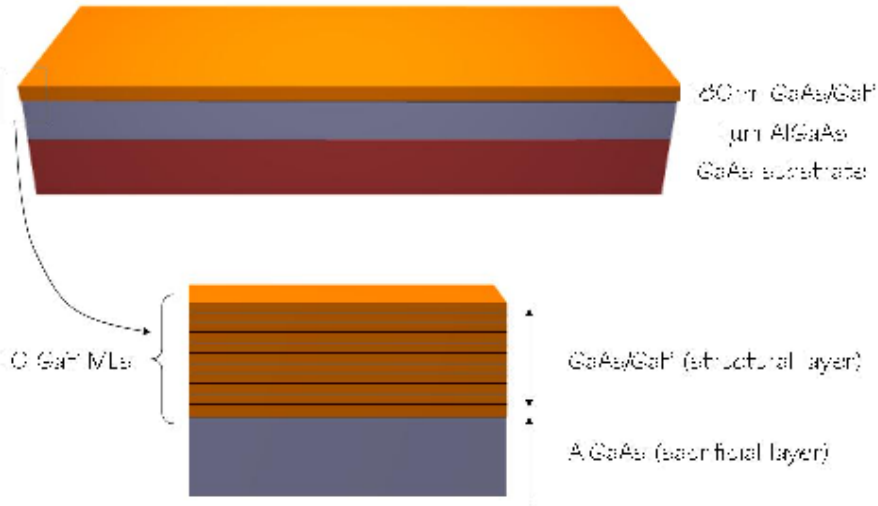

Figure 7 : a) Schematic picture of the grown (GaAs/GaP)/AlGaAs heterostructure on the GaAs (001) substrate. !0MLs of GaP are introduced symmetrically into the GaAs/GaP structural layer.

The structural GaAs/GaP layer grows coupled to the AlGaAs layer and accumulates a strong tensile stress. But, when removing the sacrificial layer by a HF wet etching, the suspended GaAs/GaP layer releases its accumulated stress to achieve a final strain state. This gives rise to a contraction of the suspended structure, which distance depends on the structure length (*L*), as observed in Figure 8. The value of the relaxation distance (*d*) can be calculated using a force-balanced model for strain sharing, between the GaP and GaAs layers. For an ideal elastic system, de relaxation distance can be expressed as:

$$d = L \cdot \frac{a_{0,GaAs} - a_{0,GaAsP}}{a_{0,GaAs}} = L \cdot \frac{a_{0,GaAs} - a_{0,GaP}}{a_{0,GaAs}} \cdot \frac{1}{1 + \frac{n_{GaAs}}{n_{GaP}} \cdot \frac{M_{GaAs}}{M_{GaP}}} \qquad (3)$$

where L is the length of the total etched structure ($L = L_1 + L_{undercut}$), $a_{0,GaAs}$ is the GaAs equilibrium lattice parameter and $a_{GaAs/GaP}$ is the lattice parameter of the released GaAs/GaP suspended structure, $a_{0,GaP}$ is the GaP equilibrium lattice parameter, and n and M are the corresponding number of MLs and the biaxial elastic moduli ($M = 1/(c_{11} + c_{12})$, where c_{11} and c_{12} are the elastic constants of the corresponding material). Relaxation distances in the nanometer

range are achieved for bridges length in the micrometer range, typically between 5 μm to 25 μm. This means that a precise control of the relaxation distance is obtained by varying the length of the suspended structure.

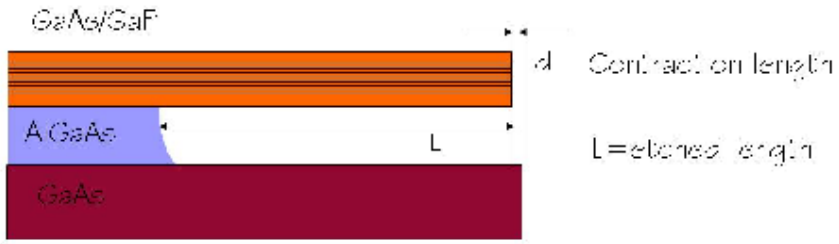

Figure 8 : a) Schematic picture of the contraction of the GaAs/GaP structural layer when the sacrificial layer is etched away.

To turn this relaxation distance into a nanogap, bridges with a narrow neck or nano-constriction are patterned. When removing the sacrificial layer, the strong tensile accumulated stress of GaAs/GaP layer releases if a breakage in the nanoconstriction is produced, as schematically shown in Figure 9. After this breakage, the beam contracts giving rise to a formation of two atomically flat surfaces or electrodes separated several nanometers.

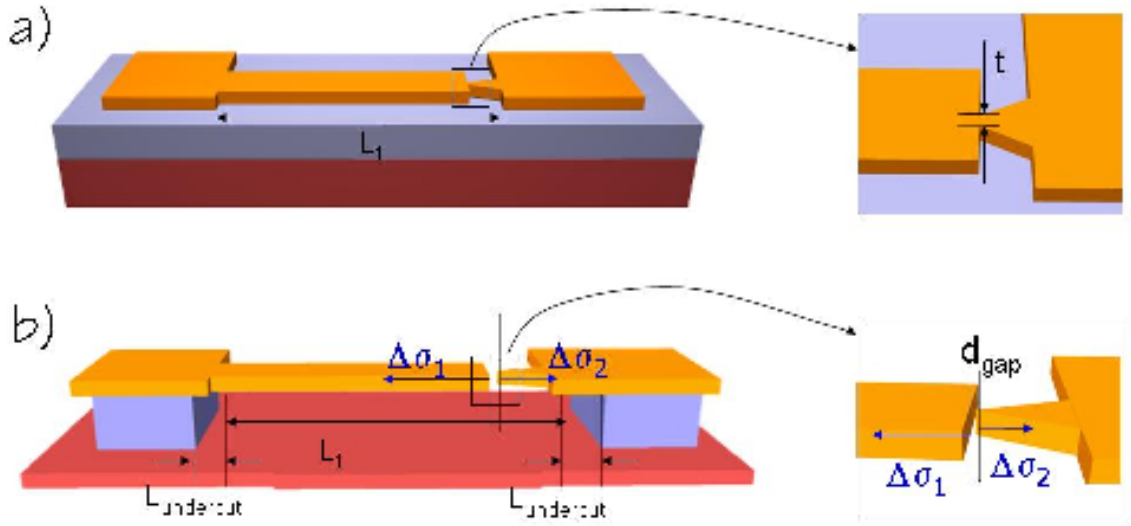

Figure 9 : a) Schematic picture of the patterned bridge with a narrow neck or nanoconstriction. b) Schematic picture of the suspended bridge after the wet etching of the AlGaAs sacrificial layer. A breakage in the nanoconstriction gives rise a nanogap formation of width d.

The constriction is patterned with an asymmetric shape and it is not centered with respect to the bridge. The structure is patterned by aligning the bridges along the [110] or [1-10] crystallographic directions, i.e., the easiest cleaved planes. The length of the patterned structure (L_1) is tailored from 4 to 10 μm and the width (t) of the constriction is kept fixed to 400nm. In this

case, a isotropic wet chemical etching using a H_3PO_4:H_2O_2:DI water solution (8:4:68) was used to transfer the resist mask patter to the GaAs/GaP structural layer. After this wet chemical etching, the constriction width decreases to 300nm. An oxygen plasma is used to removed the resist mask. A schematic picture of the device after these processes is shown in Figure 9.a). Finally, the sacrificial AlGaAs layer is removed with a HF solution, giving rise to a suspended bridge. The asymmetric shape and the position of the constriction with respect to the beam creates a non uniform lateral strain that assists the cleavage and consequent nanogap formation. There is a critical length L_C to produce a breakage. Below this value ($L<L_C$), the beam has not stored enough elastic energy to produce a breakage at the beam nanoconstriction, and the nanogap is not formed. If the length of the structure L is larger than L_C, the cleavage is produced and the equation (3) is valid. For our fabricated device 300nm nanoconstriction width, the experimental value of L_C is between 3.5 μm and 4.0 μm, increasing for wider nanoconstrictions. The calculated elastic energy per unit area stored in each GaP ML is 1.12N/m. As shown below, in this work we obtain experimental results demonstrating that 10 GaP MLs store enough elastic energy to break an 300nm width x 200 nm thick semiconductor constriction.

A scanning electron microscope (SEM) image of the final processed device, and the nanogap formed after breaking the constriction are shown in Figure 10. Figure 10.a) shows a top view of the entire device. The suspended structure is colored in light gray. The GaAs substrate and the non-etched heteroepitaxial layer are colored in blue and red respectively. A SEM image of a constriction with t = 300nm width is shown on Figure 10.b). Notice the asymmetric shape and the position of the constriction with respect to the beam. The nanogap formed by the cantilever contraction during the GaAs/GaP layer release due to the relaxation of the in-plane accumulated stress (σ_1, σ_2) is clearly observed on Figure 10.c). In this figure the structure has been tilted 90º in order to observe the nanogap details. The direction of the contraction is represented with two black arrows. An important feature is that the nanogap consists of atomically flat and strictly parallel surfaces formed by the (110) or (1-10) cleavage planes.

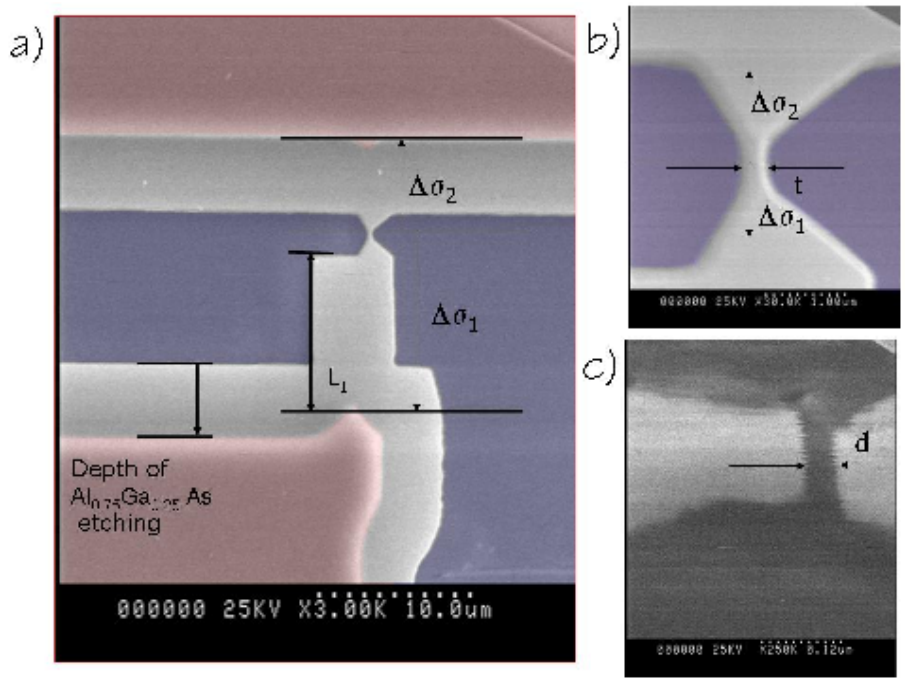

Figure 10 : SEM image of the fabricated structures. a) Top view of the device with the suspended structures colored in light gray. GaAs substrate is colored in blue, and un-etched heteroepitaxy is colored in red. The direction of the contraction due to the relaxation of elastic accumulated stress ($\Delta\sigma_1$ and $\Delta\sigma_2$) are shown by the black arrows. The undercutting of the $Al_{0.75}Ga_{0.25}As$ sacrificial layer selective wet etched is also shown. b) Top view of the defined beam constriction, t denotes the width. c) Side view of the nanogap (90 ° SEM tilted image) formed at the constriction after release.

An array of four cantilevers with the same constriction width and different beam lengths (from 4 to 10 μm) was designed and fabricated. The obtained array is shown on Figure 11.a). The formed nanogaps for different cantilever lengths are shown on Figure 11.b). Figure 11.c) shows the nanogap size *d* as a function of the beam length L_1. The data obtained at low nanogap sizes was quite hard due to our SEM resolution limit. A linear relation is obtained, as expected from eq. (1). These results clearly show that the nanogap formation mechanism developed in this work allows us to control the nanogap size by changing the nanocantilever length, getting nanogap sizes as low as 5 nm.

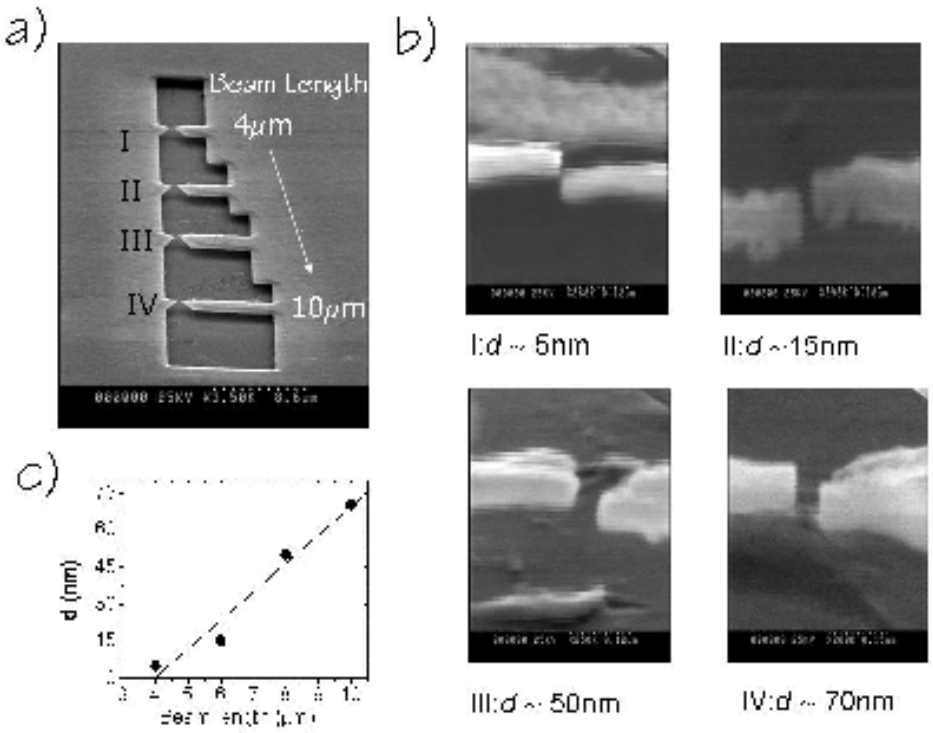

Figure 11 : a) SEM image of a four-junction array in which the length of the cantilever is designed from 4 to 10 μm. The device is tilted 45 degrees during the image acquisition. b) Side view of the different nanogaps that correspond to different beam lengths. The device is tilted 90 degrees during the image acquisition. c) Nanogap size d as a function of the beam length L_1.

It has been demonstrated the ability to fabricate electrodes separated a few nanometers. But, no tunnelling current was measured even for the smaller separation between electrodes. Several drawbacks were found. First, smaller separations between electrodes to reach the tunnelling regime must be fabricated (~ 1nm). The way to achieve this is decreasing the number of GaP ML's reducing the nanoconstriction width *t*. Secondly, the open circuit leakage current is still high (220 nA at a fixed voltage of 1.5V), probably because the AlGaAs layer is a poor "isolator". Low temperature AlGaAs layer growth could circumvent this problem.

VI.6. Conclusions.

In this chapter, a brief discussion of the fabrication process of III-V semiconductor nano-electro-mechanical systems (NEMS) is reported. Suspended GaAs structures were fabricated from GaAs/AlGaAs heterostructures grown by Molecular Beam Epitaxy (MBE). A tunneling displacement detector using fabricated nanogaps is proposed. Nanogaps as small as 5 nm were fabricated in a reproducible way, but no successful electrical measurements through the nanogap were performed.

References.

[1] C. A. Coulomb, *"Recherches théoriques et expérimentales sur la force de torsion et sur l'élasticité des fils de metal",* Memoires de l'Academie Royale des Sciences de Paris, 229–236 (1784)

[2] K. L. Ekinci and M. L. Roukes, *"Nanoelectromechanical systems"*, Rev. Sci. Instrum., **76**, 061101 (2005).

[3] S. A. Campbell and H. J. Lewerenz, 'Semiconductor Micro-machining', Wiley (1998).

[4] A. Gaidarzhy, G. Zolfagharkhani, R. L. Badzey and P. Mohanty, *"Evidence for Quantized Displacement in Macroscopic Nanomechanical Oscillators"*, Phys. Rev. Lett., **94**, 030402 (2005)

[5] K. L. Ekinci, *"Electromechanical Transducers at the Nanoscale : Actuation and Sensing of Motion in Nanoelectromechanical Systems (NEMS)"*, Small, **8-9**, 786 (2005).

[6] A. N. Cleland and M. L. Roukes*, "A nanometer-scale mechanical electrometer",* Nature, **392**, 160 (1998).

[7] Marc J. Madou, 'Fundamentals of Microfabrication : The Science of Miniaturization', CRC Press (2002).

[8] C. W. Dyck, J. H. Smith, S. L. Miller, E. M. Russick and C. L. J. Adkins, *'Supercritical carbon dioxide solvent extraction from surface-micromachined micromechanical structures'* Proc. SPIE **2879** 225 (1996).

[9] J. M. Kim, C. W. Baek, J. H. Park,S. D. Shin, Y. S. Lee and Y. K. Kim, *'Continuous anti-stiction coatings using self-assembled monolayers for gold microstructures', J. Micromech. Microeng,.* **12**, 688 (2002).

[10] Rob Legtenberg and Harrie A.C. Tilmans, "*Electrostatically driven vacuum-encapsulated poly-silicon resonators Part I. Design and fabrication"*, Sensors and Actuators A, **45**, 57 (1994).

[11] D. Karabacak, T. Kouh and K. L. Ekinci, *'Analysis of optical interferometric displacement detection in NEMS'*, J. Appl. Phys., **98**, 124309 (2005).

[12] M. D. La Haye, O. Buu, B. Camarota ad K. C. Schwab, *'Approaching the quantum limit of a nanomechanical resonator'*, Science, **304**, 74 (2004).

[13] R. G. Beck, M. A. Eriksson, M. A. Topinka, R. M. Westervelt, K. D. Maranowski and A. C. Gossard, "*GaAs/AlGaAs Self-Sensing Cantilever for Cryogenic Scanning Probe Microscopy"*, Appl. Phys. Lett., **73**, 1149 (1998).

[14] G. Binning and H. Rohrer, "The scanning tunneling microscope", Sci. Am., **253**, 50 (1985).

[15] T. W. Kenny, S. B. Waltman, J. K. Reynolds, and W. J. Kaiser, *'Novel infrared detector based on a tunneling displacement transducer'*, Appl. Phys. Lett., **58**, 100 (1991).

[16] Cheng-Hsien Liu and T.W. Kenny, *'A High-Precision, Wide-Bandwidth Micromachined Tunneling Accelerometer',* Journal of Microelectromechanical Systems, **10**, 425 (2001).

[17] S. Sadewasser, G. Abadal, N. Barniol, S. Dohn, A. Boisen, L. Fonseca and J. Esteve. 'Integrated tunnelling sensor for NEMS', Appl. Phys. Lett., **89**, 173101 (2006).

[18] I. Fernández-Martínez, Y. González and F. Briones, *'Parallel nanogap fabricaron with nanometer size control using III-V epitaxial semiconductor technology'*, Nanotechnology, **19**, 275392 (2008).

[19] Michelle M. Roberts, Levente J. Klein, Donald E. Savage, Keith A. Slinker, Mark Friesen, George Celler, Mark A. Eriksson and Max G. Lagally, *"Elastically relaxed free-standing strained silicon nano-membranes",* Nature Materials, **5**, 388 (2006).

[20] A. Mazuelas, L. Gonzalez, F. A. Ponce, L. Tapfer and F. Briones, *"Critical thickness determination of InAs, InP and GaP on GaAs"*, J. Cryst. Growth, **131**, 465 (1993).

Resumen y conclusiones

A pesar de que a lo largo de esta memoria de tesis se han ido exponiendo las conclusiones extraídas en cada parte del trabajo, a continuación se exponen los principales resultados obtenidos:

- Se pueden depositar películas delgadas amorfas de $Fe_{80}B_{20}$ mediante pulverización catódica triodo. Éstas películas poseen un carácter magnéticamente blando combinado con un alto coeficiente de magnetostricción.

- A partir de las medidas *in-situ* de las tensiones acumuladas durante el depósito, se puede obtener información acerca del mecanismo de crecimiento de la película delgada de $Fe_{80}B_{20}$,. Además, se pueden optimizar los parámetros de depósito para obtener películas delgadas de $Fe_{80}B_{20}$ con tensión acumulada neta nula.

- Se puede controlar la dirección de la anisotropía magnética variando los parámetros de depósito y geometría del substrato, maximizando así el esfuerzo magnetostrictivo.

- La resistencia a la corrosión de las aleaciones de $Fe_{80}B_{20}$ mejora enormemente al ser depositadas en presencia de nitrógeno. Bajo estas condiciones, se mantiene el carecer amorfo de las películas delgadas, alterándose sus propiedades magnéticas. Se observa un aumento en el coeficiente de magnetostricción e imanación de saturación para concentraciones moderadas de nitrógeno.

- Se ha diseñado un Microscopio de Fuerzas Atómicas (AFM) magnetostrictivo para medidas de topografía en medios líquidos. Micro-palancas comerciales son recubiertas con película delgadas de Fe-B-N, cuyo depósito se realiza en las condiciones óptimas obtenidas anteriormente. Se obtienen buenos factores de calidad (Q) de oscilación de la micro-palanca el medios líquidos.

- Por último, se fabrican Sistemas Nano-Electro-Mecánicos (NEMS) basados en tecnología III-V. Además, se propone un sistema de medida de desplazamientos de los elementos nanomecánicos basado en el efecto túnel, cuyo funcionamiento no se consigue demostrar.

List of publications

Papers related to this thesis:

- **I. Fernández-Martínez**, M. S. Martín-González, R. González-Arrabal, R. Álvarez, F. Briones and J. L. Costa-Krämer*, 'Nitrided FeB amorphous thin Films for Magneto Mechanical Systems'*, Journal of Magnetism and Magnetic Materials, 320, 68 (2008).

- **I. Fernández-Martínez**, J. L. Costa-Krämer and F. Briones*, 'Stress and magnetoelastic properties control of amorphous Fe80B20 thin films during sputtering deposition'*, Journal of Applied Physics, 103, 113902 (2008).

- **I. Fernández-Martínez**, Y. González and F. Briones*, 'Parallel nanogap fabrication with nanometer size control using III-V semiconductor epitaxial technology'*, Nanotechnology, 19, 275302 (2008).

- **I. Fernández-Martínez**, M. Penedo, J. L. Costa-Krämer, M. Luna and F. Briones*, 'Magnetostrictive drive of AFM cantilevers for liquid operation'*, submitted to Applied Physics Letters.

Patents related to this thesis:

- **I. Fernández-Martínez**, M. Penedo, J. L. Costa-Krämer, M. Luna and F. Briones*, 'Elemento micromecánico magnetostrictivo resistente a la corrosión'.* Oficina Española de Patentes y Marcas (OEPM) (12/10/2008).

Other papers:

- P. Alonso-González, L. González, Y. González, D. Fuster, **I. Fernández-Martínez,** J. Martín-Sánchez and L. Abelmann, *'New process for high optical*

quality InAs quantum dots grown on patterned GaAs(001) substrates', Nanotechnology **18**, 355302 (2007).

- L . Fàbrega, **I. Fernández-Martínez**, O. Gil, M. Parra-Borderías, A. Camón, J. L. Costa-Krämer, R. González-Arrabal, J. Sesé, F. Briones, J. Santiso ad F. Peiró, '*Mo-based proximity bilayers for TES : microstructure and properties'*, accepted to IEEE Transactions on Applied Superconductivity.

- B. Alén, D. Fuster, **I. Fernández-Martínez**, J. Martínez-Pastor, Y. González, F. Briones ad L. González, *'Semiconductor quantum wire planar arrays as an scalable platform for solid state quantum byte fabrication'*, submitted to NanoLetters. (http://arxiv.org/abs/0803.0569)

Contributions to international conferences (póster):

- **I. Fernández-Martínez**, F. Torres, A. Pardo, J. P. Silveira, J. V. Anguita, J. L. Costa-Krämer and F. Briones, *'Fabricación de microcantilevers de GaAs como sensor de desplazamientos sub-nanométricos*', III Reunión de la Red de Nanociencia, Oviedo (2003).

- **I. Fernández-Martínez**, F. Torres, A. Pardo, J. P. Silveira, J. V. Anguita, J. L. Costa-Krämer and F. Briones, '*NEMS on epitaxial GaAs technology: break junction displacement sensor*', 1st NanoSpain Workshop, San Sebastián (2004).

- **I. Fernández-Martínez**, F. Torres, A. Pardo, J. P. Silveira, J. V. Anguita, J. L. Costa-Krämer and F. Briones, '*NEMS on epitaxial GaAs technology: break junction displacement sensor*', Trends in Nanotechnoloogy, Segovia (2004).

- **I. Fernández-Martínez**, F. Torres, A. Pardo, J. P. Silveira, J. V. Anguita, J. L. Costa-Krämer and F. Briones, '*NEMS on epitaxial GaAs technology: break junction displacement sensor*', 1st Nanomechanical Sensors, Madrid (2004).

- **I. Fernández-Martínez**, R. Alvárez-Sanchez, M. Luna and F. Briones, '*Modulación magnética para modos dinámicos en líquidos*', V Congreso español de Fuerzas y Túnel', Murcia (2006).

- **Fernández-Martínez**, R. Alvárez-Sanchez, M. Luna and F. Briones, '*Modulación magnética para modos dinámicos en líquidos*', V Congreso español de Fuerzas y Túnel', Murcia (2006).

- **I. Fernández-Martínez** and F. Briones, *'In situ monitoring of intrinsic strain evolution during growth of sputtered amorphous magnetostrictive Fe-B-N thin films'*, 17th International Vacumm Congress (IVC-17), Stockholm (2006).

- **I. Fernández-Martínez,** M.S. Martín-González, R. González-Arrabal, R.Álvarez, J.L. Costa-Krämer, F. Briones, *'Nitrided FeB amorphous thin Films for Magneto Mechanical Systems'*, Trends in Nanotechnoloogy, Grenoble (2006).

- **I. Fernández-Martínez**, J. L. Costa-Krämer and F. Briones, *'Stress and magnetoelastic properties control of amorphous $Fe_{80}B_{20}$ thin films during triode sputtering deposition*, Intermag, Madrid (2008).

- **I. Fernández-Martínez**, M. Penedo, J. L. Costa-Krämer, M. Luna and F. Briones*, 'Magnetostrictive drive of AFM cantilevers for liquid operation'*, , Trends in Nanotechnoloogy, Oviedo (2008).

- B. Alén, D. Fuster, **I. Fernández-Martínez**, J. Martínez-Pastor, Y. González, F. Briones and L. González, *'Semiconductor quantum wire planar arrays as an scalable platform for solid state quantum byte fabrication'*, International Conference on the Physics of Semiconductors (ICPS), Rio de Janeiro (2008).

- L . Fàbrega, **I. Fernández-Martínez**, O. Gil, M. Parra-Borderías, A. Camón, J. L. Costa-Krämer, R. González-Arrabal, J. Sesé, F. Briones, J. Santiso ad F. Peiró, '*Mo-based proximity bilayers for TES : microstructure and properties'*, Applied Superconductivity Conference (ACS), Chicago (2008).

Contributions to international conferences (oral):

- **I. Fernández-Martínez**, Y. González and F. Briones*, 'Parallel nanogap fabrication with nanometer size control using III-V semiconductor epitaxial technology'*, NanoIberial Conference, Braga (2008).